Influence of Structural Flexibility on Flapping Wing Propulsion

DISSERTATION

Aaron M. McClung, CIV

AFIT/DS/ENY/09-J01

DEPARTMENT OF THE AIR FORCE
AIR UNIVERSITY

AIR FORCE INSTITUTE OF TECHNOLOGY

Wright-Patterson Air Force Base, Ohio

AFIT/DS/ENY/09-J01

Influence of Structural Flexibility on Flapping Wing Propulsion

DISSERTATION

Presented to the Faculty
Department of Aeronautics and Astronautics
Graduate School of Engineering and Management
Air Force Institute of Technology
Air University
Air Education and Training Command
In Partial Fulfillment of the Requirements for the
Degree of Doctor of Philosophy Aeronautical Engineering

Aaron M. McClung, B.S.A.E., M.S.M.E
CIV

June, 2009

AFIT/DS/ENY/09-J01

Influence of Structural Flexibility on Flapping Wing Propulsion

Aaron M. McClung, B.S.A.E., M.S.M.E
CIV

Approved:

/signed/	30 April 2009
Dr. Raymond Maple Dissertation Advisor	date
/signed/	30 April 2009
Dr. Philip Beran Committee Member	date
/signed/	30 April 2009
Dr. Donald Kunz Committee Member	date
/signed/	30 April 2009
Dr. James Chrissis Committee Member	date

Accepted:

/signed/	30 April 2009
M.U. THOMAS Dean, Graduate School of Engineering and Management	date

AFIT/DS/ENY/09-J01

Abstract

Flapping wing propulsion offers an attractive alternative to conventional propulsion methods for future unmanned aerial systems. At scales relevant for future micro- and nano-aerial vehicles, large insects often utilize a single aerodynamic surface undergoing large amplitude oscillatory motion to produce the lifting, propulsive, and control forces necessary for sustained flight. These dynamic wing motions produce unsteady aerodynamic phenomena which are responsible for the primary lifting, propulsive, and control forces. The use of unsteady aerodynamic phenomena differentiate flapping wing fliers from conventional fixed and rotary wing configurations.

It has been previously demonstrated that the unsteady aerodynamic phenomena are sensitive to variations in the wing motion as well as the dynamic response of flexible wing structures. Yet, it is not well understood how the unsteady aerodynamic phenomena, dynamic wing motions, and structural response interact to determine overall aerodynamic performance. This work examines the influence of structural response on the local unsteady aerodynamic phenomena produced by the dynamic wing motions, and considers the influence of local variations in the unsteady aerodynamic phenomena on overall aerodynamic performance.

To gain insight into the interplay between wing motion, structural response, and unsteady aerodynamic phenomena, Navier-Stokes based numerical simulation was used to examine the influence of prescribed structural deformations on the aerodynamic performance of a characteristic flapping wing configuration based on the Hawkmoth *Manduca sexta*. Prescribed deformations, including span-wise feathering and span-wise bending, for an elastic axis located at the leading edge of the wing were superimposed onto the rigid wing motion defined by a set of experimentally determined kinematic parameters for a Hawkmoth at hover. Both deformation modes influence the velocity and acceleration profile of the wing surface, altering the unsteady aerodynamic phenomena produced by the dynamic wing motion.

The spanwise feathering rotation, or torsional response, altered the motion of the wing near the wing root. This variation in the acceleration profile influenced the non-circulatory aerodynamic response and the local wake structures produced near the wing root during pronation and supination. Increased lifting forces and enhanced aerodynamic efficiencies were observed for a moderate increase in torsional flexibility.

Peak bending deformations near the wing tip also occured during pronation and supination, altering the velocity and acceleration profiles of the wing as the circulatory aerodynamic phenomena undergo a transition as the wing changes direction of motion. Because of the timing of the bending deformations, small tip deformations may have a significant influence on overall aerodynamic performance.

Acknowledgements

First and foremost, I owe a large debt of gratitude to my research advisor, Dr. Raymond Maple, for his guidance during the pursuit of this research and to my research committee, Dr. Philip Beran, Dr. Donald Kunz, and Dr. James Chrissis for their support of my research and feedback on this document. This work was sponsored with significant funding by AFOSR under the direction of program manager Dr. Victor Giurgiutiu, and AFRL/RBSD under the direction of Dr. Philip Beran.

I would like to thank Mr. David Doak and Mr. Jason Speckman for their efforts maintaining the AFIT Linux resources and for answering my many questions with tireless humor. I would also like to thank Mr. James Gray for assisting with access to the AFRL DSRC. Together they provided invaluable assistance, without which the simulations that form the core of this work would still be running.

Finally, I would like to thank my wife for her support and encouragement during my time at AFIT. The last four years have been an adventure, and I look forward to our future adventures together.

Aaron M. McClung

Table of Contents

List of Figures

Figure Page

Figure Page

Figure Page

Figure Page

Figure Page

List of Tables

List of Symbols

Symbol		Page
D	Cylinder Diameter	27
St	Strouhal Number, fD/U	27
ρ_{REF}	OVERFLOW Reference Density	43
U_{REF}	OVERFLOW Reference Velocity	43
S_{REF}	OVERFLOW Reference Area	43
L_{REF}	OVERFLOW Reference Length	43
CF	Force Coefficient	43
CM	Moment Coefficient	43
F	Force	43
M	Moment	43
P	Power	43
*	Non-dimensional parameter, OVERFLOW reference velocity	43
$\vec{M}_{aero}$	Integrated Aerodynamic Moment at the Origin of Rotation	44
$\vec{F}_{aero}$	Integrated Aerodynamic Force at the Origin of Rotation	44
$\vec{\dot{\theta}}$	Rotational Rate	44
$\vec{\ddot{\theta}}$	Rotational Acceleration	44
$\vec{v}$	Translational Velocity	44
η_{aero}	Aerodynamic Efficiency	44
PL	Power Loading	44
$\eta_{inertial}$	Inertial Efficiency	45
a	Speed of Sound	46
ρ_{rotor}	Density defined in **&EROTOR**	46
M_{rotor}	Mach number at rotor tip defined in **&EROTOR**	46
V_{tip}	Velocity at the wing tip	54

List of Abbreviations

Abbreviation		Page
DARPA	Defense Advanced Research Projects Agency	8
NASA	National Aeronautics and Space Administration	18
AFIT	Air Force Institute of Technology	18
HPC	High Performance Computing	18
AFRL	Air Force Research Laboratory	18
MSRC	Major Shared Resource Center	18
WENO	Weighted Essentially Non-Oscillatory	18
DCF	Domain Connectivity Function	21
GMP	Geometry Manipulation Protocol	21
6DOF	Six-Degree of Freedom	21
MAC	Marker-and-Cell	22
SIMPLE	Semi-Implicit Method for Pressure Linked Equations	22
FSI	Fluid-Structure Interaction	23
PIV	particle image velocimetry	31

INFLUENCE OF STRUCTURAL FLEXIBILITY ON FLAPPING WING PROPULSION

I. Introduction

Natural fliers operate effectively in flow regimes where the propulsion efficiency of conventional systems decrease with size, and demonstrate an aerial agility that has yet to be achieved by engineered fliers. One of the features that differentiate small flapping wing fliers from engineered, fixed and rotary wing, fliers is the use of unsteady aerodynamic phenomena to produce the aerodynamic forces necessary for sustained flight. By understanding how natural fliers utilize and control the unsteady aerodynamic phenomena responsible for their enhanced aerial abilities, engineered mini- and micro-aerial systems may be developed that take advantage of similar unsteady aerodynamic mechanisms. Thus, bio-inspiration offers a means to enhance the performance of the next generation of mini- and micro-aerial systems over existing fixed and rotary wing systems.

1.1 Unsteady Aerodynamics

The unsteady aerodynamic phenomena that allow insects to operate efficiently at small scales are produced by dynamic rotations of the insect wing. These wing rotations are oscillatory in nature and encompass a large variety of motion profiles and associated tip paths for different species of insects. The tip path associated with a particular insect species depends on the insect morphology, the configuration of the wing and body structures and joints, and the insect physiology which determines how the wing is actuated.

At wing lengths on the order of 50 millimeters, the dominant unsteady aerodynamic phenomenon assumed to be responsible for aerodynamic lift is a leading edge vortex produced by a laminar flow separation near the leading edge of the wing [1]. This vortical structure produces a region of low pressure near the wing surface and influences the strength of the bound circulation about the wing. This leading edge vortex is similar to the vortical structure produced during dynamic stall observed for conventional configurations undergoing rapid pitch or plunge maneuvers. Unlike the vortex produced during a dynamic stall, the leading edge vortex observed for flapping wing fliers is stable for the duration of the half-stroke.

In addition to circulatory aerodynamic phenomena, there are aerodynamic forces associated with the acceleration of the volume of air in the immediate vicinity of the wing as the wing changes direction of motion at the end of each half-stroke. This non-circulatory phenomenon influences the pressure distribution along the wing surface as well as the pressure and velocity field about the wing. The circulatory and non-circulatory aerodynamic phenomena each produce localized wake structures. These local wake structures interact to form the complex wake structures observed for natural fliers. Sustained flight is achieved when the vortical wake structures align in space and time to form a coherent momentum jet.

1.2 Dynamic Structural Response and Fluid-Structure Interaction

Because the aerodynamic phenomena are produced by the dynamic wing motion, they are sensitive to variations in the motion profile [2,3,4,5,6,7]. In addition to variations in the underlying motion profile, any mechanisms that alter the wing motion, such as structural response, may influence the unsteady aerodynamic phenomena and the resulting aerodynamic forces [8,9,10,11]. Most insects have light-weight, flexible, wing structures that exhibit varying degrees of dynamic response during the wing stroke. The amplitude and modal contribution of the dynamic structural response depend on several factors, including the size of the insect, the wing structure, material properties, and the forces and moments acting on the wing.

There are two significant sets of forces and moments acting on the wing structure, the inertial-elastic forces due to the dynamic wing motion, and the aerodynamic forces produced in response to the dynamic wing motions. Both the inertial-elastic and aerodynamic forces depend on the profile of the motion at the wing root. However, the aerodynamic forces are also sensitive to phenomena that introduce local variations in the wing motion, such as structural response. This sets up a potential feedback loop where aerodynamic forces influence structural response, and structural response influences the aerodynamic forces. The influence of this multi-physics coupling on aerodynamic performance should be understood in order to optimize future mini- and micro-aerial vehicle designs that utilize flapping wing propulsion.

1.3 Multi-Physics Interactions

Multi-physics coupling in flapping wing propulsion can be extended to include the kinematic parameters that define the dynamic wing motion. If the goal is to optimize a design to achieve a desired set of performance goals, to trim an existing design for a given state, such as maximum efficiency or maximum thrust, or to achieve an agile maneuver, the kinematics, aerodynamics, and structural dynamics should be considered to be linked. Alterations to the actuation of the wing, or base excitation, influence the unsteady aerodynamic phenomena and aerodynamic forces, the inertial-elastic forces acting on the wing structure, and the interactions between the dynamic structural response and the unsteady aerodynamic forces. The nature of the fluid-structure-kinematic coupling is characteristic of a specific insect species and the kinematic parameters associated with the insect's physiology.

1.4 Multi-Physics Simulation

Examining the influence of multi-physics coupling using numerical simulation depends on an understanding of the influence of each of the physical components that contribute to the coupled system. In the case of the flapping wing problem, the influence of kinematics and structural flexibility on aerodynamic performance are active areas of investigation.

Understanding these multi-physics interactions requires a benchmark configuration where the characteristics of each of the physical components are well documented. For a flapping wing flier, this would start with a characterization of the wing structure and material properties, documentation of the kinematic parameters that describe the wing motion in time, an understanding of the root actuation of the wing structure as a function of the kinematic parameters, and an understanding of the aerodynamic phenomena associated with the chosen wing kinematics. Suitable simulation techniques that have the fidelity to capture the essential characteristics of each physical component would then be selected and coupled in order to simulate the multi-physics interactions and document the influence of coupling on aerodynamic performance.

1.5 Scope of Research

The objective of this research is to understand how structural response in the form of local deformations and feathering rotations influence the underlying unsteady aerodynamic phenomena that are responsible for the aerodynamic forces and influence aerodynamic performance. This work represents a benchmark multi-physics simulation of flapping wing propulsion and the first examination of the influence of feathering modes on the local aerodynamic phenomena using three-dimensional Navier-Stokes simulation.

1.5.1 Thesis Statement.

The wings of natural fliers exhibit significant structural deformations in free flight. This structural response influences the strength and timing of the local aerodynamic mechanisms produced by the dynamic wing motion. Variations in the local aerodynamic mechanisms influence the overall aerodynamic performance, as represented by mean lift, power, and efficiency.

1.6 Research Approach

In order to examine the influence of structural response on the unsteady aerodynamic phenomena and the associated influence on the aerodynamic forces and moments, numerical simulation of the Navier-Stokes equations was used to predict the aerodynamic performance of a test configuration based on the Hawkmoth *Manduca sexta* with prescribed structural deformations. The available body of literature examining the Hawkmoth include characterizations of the unsteady aerodynamic mechanisms, kinematic parameters that approximate the rigid wing motion in the flight regime from hover to forward flight, and static characterizations of the Hawkmoth wing structure. This body of literature, while incomplete from the standpoint of a coupled multi-physics simulation, allows for the influence of the dominant structural mode, feathering, or torsion about the wing length, on the unsteady aerodynamic mechanisms to be examined using a decoupled simulation approach.

As an initial investigation, several preliminary tasks had to be accomplished in order to examine the influence of structural response on the unsteady aerodynamic phenomena. The preliminary tasks fell into two main categories, identification and development of a suitable test configuration based on available literature, and the identification, acquisition, modification, and demonstration of a suitable flow solver.

To examine the influence of structural response on the aerodynamic mechanisms, it was considered prudent by the author to understand the influence of kinematic approximation on the aerodynamic forces. A complete investigation considering the influence of individual kinematic parameters was too intensive for a study also considering the influence of structural flexibility. In order to gain insight into the influence of the dynamic wing motions on the unsteady aerodynamic phenomena, the kinematic approximation used for this study was systematically varied for a selected set of simulations. Simulations were computed for wing motion based on 2-, 3-, and 4-term Fourier approximations of experimentally derived kinematic parameters. These rigid-wing simulations also served as a baseline when examining the influence of structural response on the unsteady aerodynamic phenomena and aerodynamic performance.

While a complete physical characterization of the wing structure was not available for this research, the published study documenting the dynamic wing motions at hover recorded feathering orientation along the wing length as a function of time. This measurement allowed a spanwise feathering distribution along the wing length to be reconstructed. This reconstruction of the feathering parameter was used to prescribe the feathering rotation of the wing surface for the numerical simulations. The influence of bending was examined using an inertially motivated bending distribution and time history, and is presented as a proof-of-concept demonstration of the solution method and as an extension of the fluid-structure coupling mechanisms studied with the prescribed torsional deformations.

1.7 Document Organization

The remainder of this document is organized as follows:

Chapter II: Covers the fundamentals of insect flight and the relevant aerodynamic phenomena. This chapter also provides an overview of the aerodynamic simulation method and the capabilities of OVERFLOW, the Navier-Stokes flow solver selected for this research, as well as the modifications that form the basis of the updated flow solver, OVERFLOW 2.1-Elastic.

Chapter III: Provides a discussion of the verification and validation of the updated OVERFLOW 2.1-Elastic flow solver, and demonstrates the ability of OVERFLOW 2.1-Elastic to capture the characteristic aerodynamics exhibited by a benchmark configuration modeled on the Hawkmoth.

Chapter IV: Details the method in which the complex behavior of the Hawkmoth was reduced to a characteristic configuration that exhibits the unsteady aerodynamic phenomena observed in previous studies while providing a simplified configuration for future numerical and experimental studies.

Chapter V: Examines the influence of the kinematic approximation on the unsteady aerodynamic mechanisms and aerodynamic performance.

Chapter VI: Examines the influence of span-wise feathering variation on the unsteady aerodynamic phenomena.

Chapter VII: Presents a proof-of-concept examination of the influence of bending and the influence on the unsteady aerodynamic phenomena.

Chapter VIII: Summarizes the influence of the kinematic profile, feathering variation, and bending on the unsteady aerodynamic mechanisms and presents recommendations for future research efforts.

II. Numerical Simulation of a Flexible Flapping Wing Flier

Natural fliers range in size from the millimeter scale to the meter scale and operate at Reynolds numbers from 100 to 100,000. Throughout this range of sizes and operating conditions, natural fliers utilize a variety of wing motions to generate the aerodynamic forces necessary for sustained flight. The selection of a single representative species for a detailed examination represents a balancing act between desired characteristics and the availability of previous research upon which a numerical model may be developed.

2.1 The Hawkmoth

The Hawkmoth *Manduca sexta* represents one such species that exhibits capabilities desired for the next generation of mini- and micro-aerial vehicles at a scale relevant for future micro-aerial vehicle designs. A typical adult Hawkmoth has a wing span around 110 millimeters and total mass of 1.8 grams [12, 13], which falls within the upper bound of the DARPA definition of a micro-aerial vehicle [14]. The aerodynamic phenomena utilized by the Hawkmoth to achieve sustained hover, agile maneuvers, and forward flight have been previously studied by Ellington, Liu, and others [15,16,17,6,18,19,20,21,22,23,24,25], who have documented the dynamic wing motions, unsteady aerodynamic phenomena, and morphological characteristics.

2.1.1 Aerodynamic Characteristics. In this operating regime, one of the dominant unsteady aerodynamic mechanisms is the leading edge vortex produced during the translational phase of the wing stroke [15]. The leading edge vortex is produced by a laminar flow separation just aft of the leading edge that forms a strong vortical structure as shown in Figure 1. This vortical structure produces a region of low static pressure that influences the pressure distribution along the wing, shown in Figure 2, due to the proximity of the vortical structure to the wing surface. As previously discussed in Section 1.1, the leading edge vortex is similar to dynamic stall observed for conventional configurations at high angles of attack. However, the leading edge vortex exhibited by the Hawkmoth is stabilized for the duration of

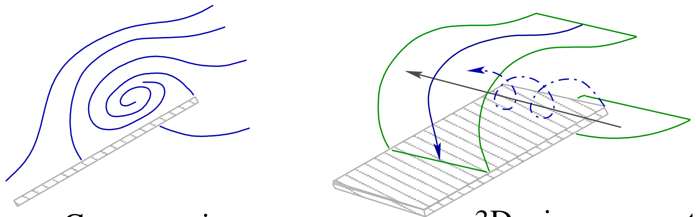

Cross–section 3D wing segment

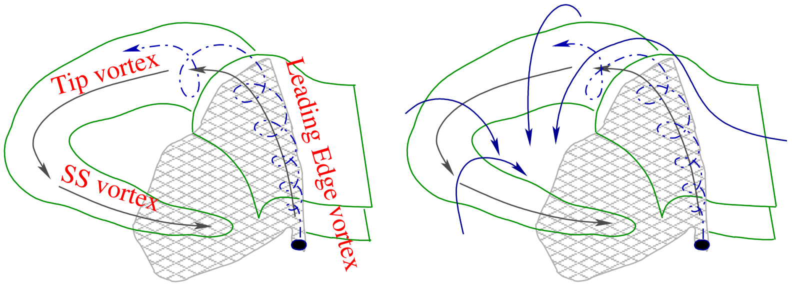

Inside the vortex system Outside the vortex system

Figure 1: Diagram of a typical leading edge vortex. Vortical structures are shown using blue dashed lines and bounded by green solid lines. Streamlines are shown using solid blue lines, and the wing surface is shown in gray. Figure adapted from van den Berg and Ellington [16].

each half-stroke by a span-wise flow towards the wing tip at the core of the vortical structure.

The finite length Hawkmoth wing exhibits significant three-dimensional tip effects which produce a strong vortical structure at the wing tip. The three-dimensional tip effects are accentuated by the spanwise pressure distribution, which features a region of low pressure near the wing tip, as shown in Figure 2. The spanwise flow and the leading edge vortex coalesce with the tip vortex to form a continuous vortical structure that extends along the length of the wing from near the wing root until it is shed into the wake along the path of the wing tip, also shown in Figure 1.

The end of each half-stroke is characterized by a deceleration of the wing sweep until the translational velocity component reaches zero and the direction of motion changes. This deceleration is accompanied by a feathering rotation along a span-wise axis that re-orients the leading edge of the wing for the following half-stroke. As the wing changes direction of motion, the strength of the leading edge vortex that

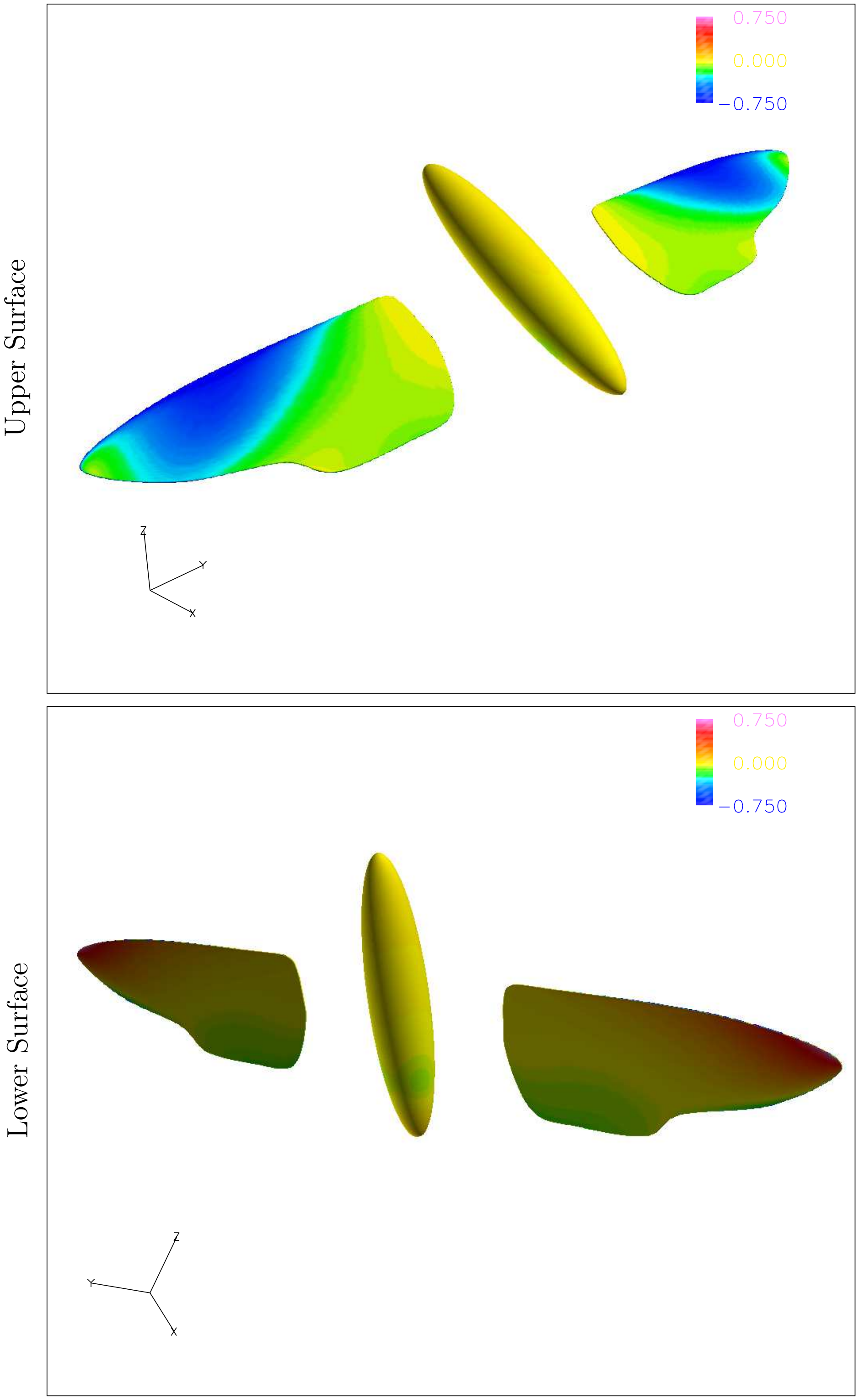

Figure 2: Pressure distribution along a *Manduca sexta* planform computed using rigid wing motions.

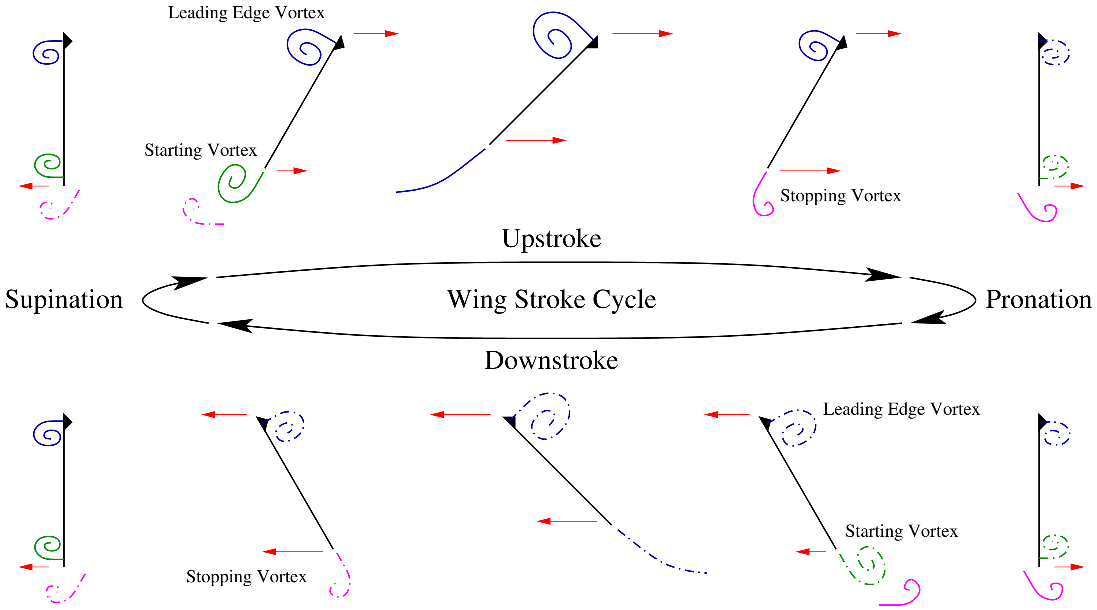

Figure 3: Evolution of the leading edge vortex, starting vortex, and stopping vortex during the stroke cycle. Vortical structures produced during the upstroke are shown as solid lines and vortical structures produced during the downstroke are shown as dashed lines. The velocity of the wing at the leading and trailing edges is shown in red. Figure adapted from van den Berg and Ellington [16].

developed during the preceding half-stroke decreases until it is released into the wake. This decrease in the strength of the leading edge vortex and bound circulation about the wing is balanced by a release of vorticity into the wake at the trailing edge. The vorticity shed from the trailing edge of the wing forms a stopping vortex, shown in Figure 3. As the direction of motion changes and the wing accelerates into the next half-stroke, a new leading edge vortex is formed along with an accompanying starting vortex that balances the change in bound circulation about the wing. This cycle is illustrated in Figure 3.

The vortex wake produced by the leading edge vortex, tip vortex, and the stopping and starting vortices produced by each wing form a vortex ring [16, 18, 21]. When the phase and orientation of the vortical structures align, the vortex ring produces a momentum jet that provides the thrust necessary for sustained hovering and forward flight, as shown by the streamlines outside the vortex system in Figure 1.

In addition to the circulatory aerodynamic mechanisms that produce the leading edge vortex and influence the bound circulation about the wing, the dynamic wing motions produce additional aerodynamic forces associated with the acceleration and deceleration of the volume of air immediately surrounding the wing. These non-circulatory forces influence the pressure distribution along the wing length as well as the pressure distribution in the fluid immediately surrounding the wing. These pressure variations influence the local velocity distribution, and potentially alter the formation and convection of the vortical wake structures associated with the circulatory aerodynamic phenomena. Wing-wake interaction is an example of a non-circulatory aerodynamic phenomenon that occurs at the end of each half-stroke as the wing "encounters" the wake that is entrained behind the wing during the half-stroke.

2.1.2 Structural Characteristics. Hawkmoth wings are lightweight, compliant structures that exhibit significant structural response during the wing stroke. A typical wing response at hover is captured in the sequence of stills shown in Figures 4 and 5. The sequence of still frames highlight the large variation in feathering orientation of the wing as a function of span-wise position, while the shape and magnitude of any deformations associated with bending is difficult to discern through observation alone. Figure 6 provides an example of how point of view can influence qualitative estimates of bending.

Previous experimental investigations indicate that the Hawkmoth wing is a non-homogeneous structure with pronounced anisotropic properties [26], with several orders of magnitude difference between the static bending stiffnesses measured in the chord-wise and span-wise directions. Lacking a dynamic characterization of the Hawkmoth wing structure, trends must be drawn from structural characterizations that have been performed on other insects, such as the Fruit Fly, Dragon Fly, and the Desert Locust [27, 28, 29, 30, 31, 32, 33, 34, 35], and bulk structural properties for the Hawkmoth wing estimated using static bending and torsion tests [36, 37, 38].

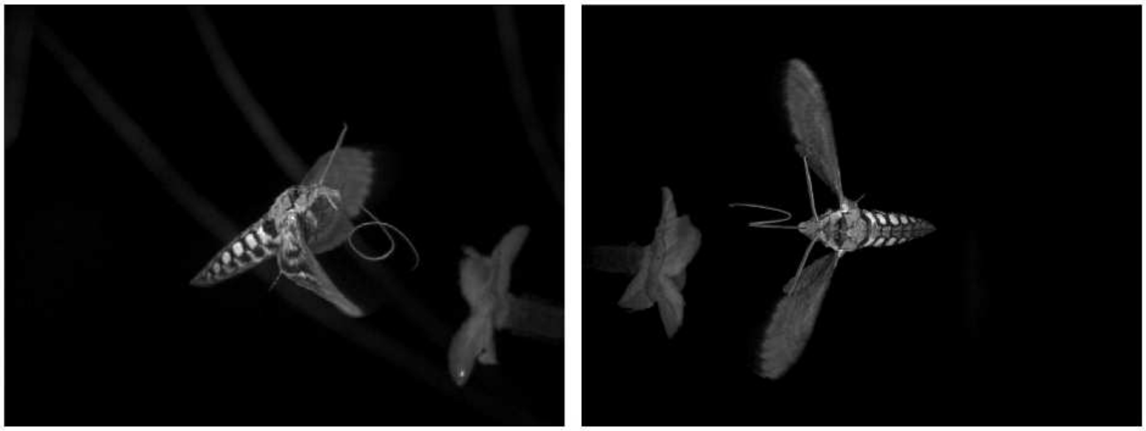

$t/\tau = 1/6$

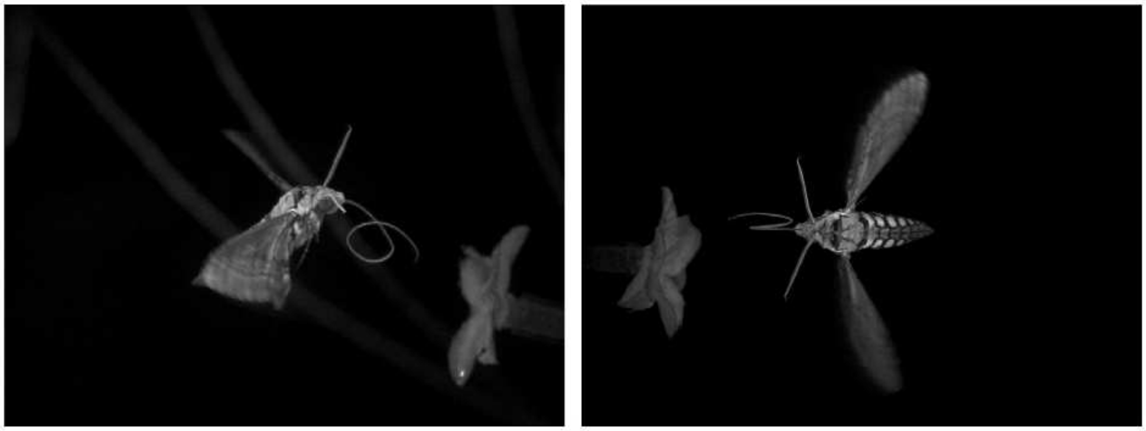

$t/\tau = 2/6$

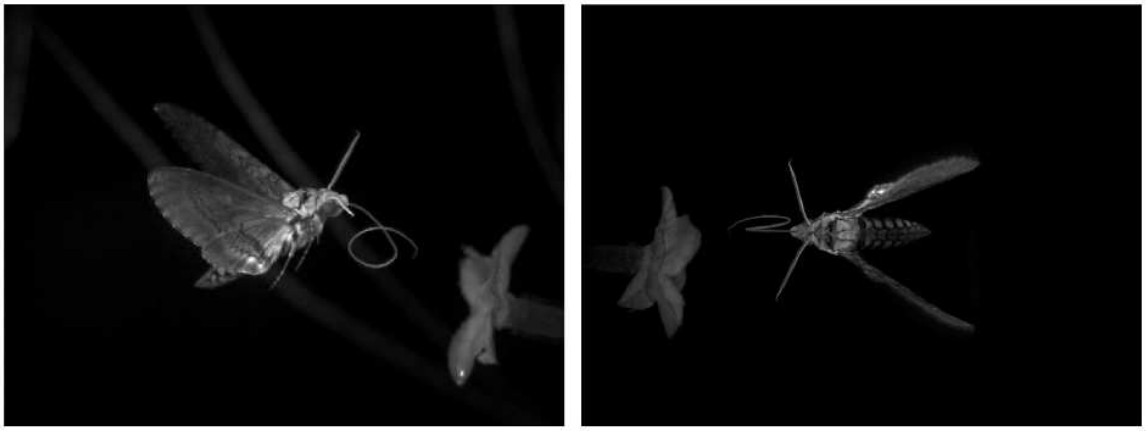

$t/\tau = 3/6$

Figure 4: A typical upstroke for a Hawkmoth at hover. The point of view highlights the span-wise feathering variation at $t/\tau = 1/6$, and the wing planform at $t/\tau = 3/6$. Video stills are reproduced with permission [13].

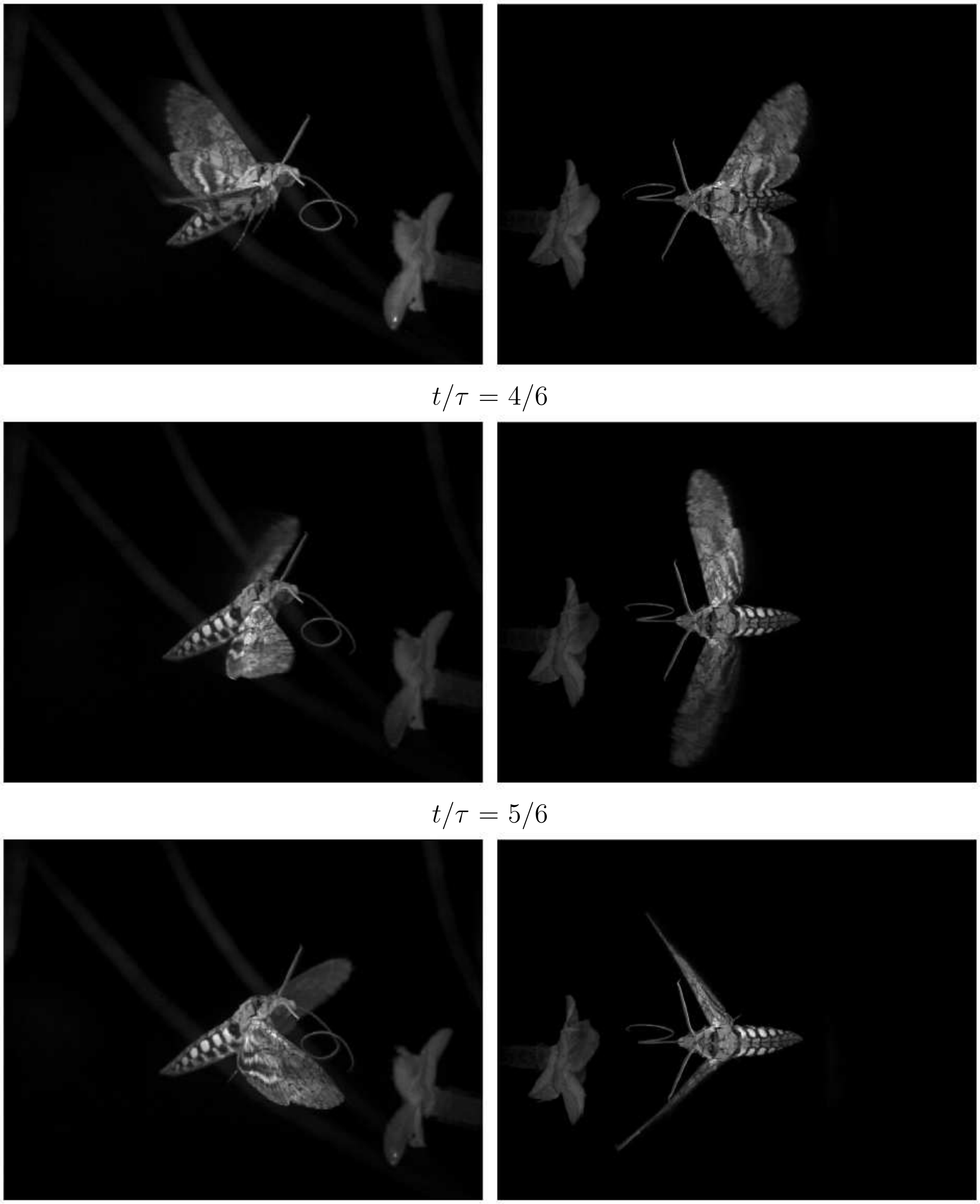

$t/\tau = 4/6$

$t/\tau = 5/6$

$t/\tau = 6/6$

Figure 5: A typical downstroke for a Hawkmoth at hover. The point of view hinders qualitative observation of the feathering variation during the half-stroke. Video stills are reproduced with permission [13].

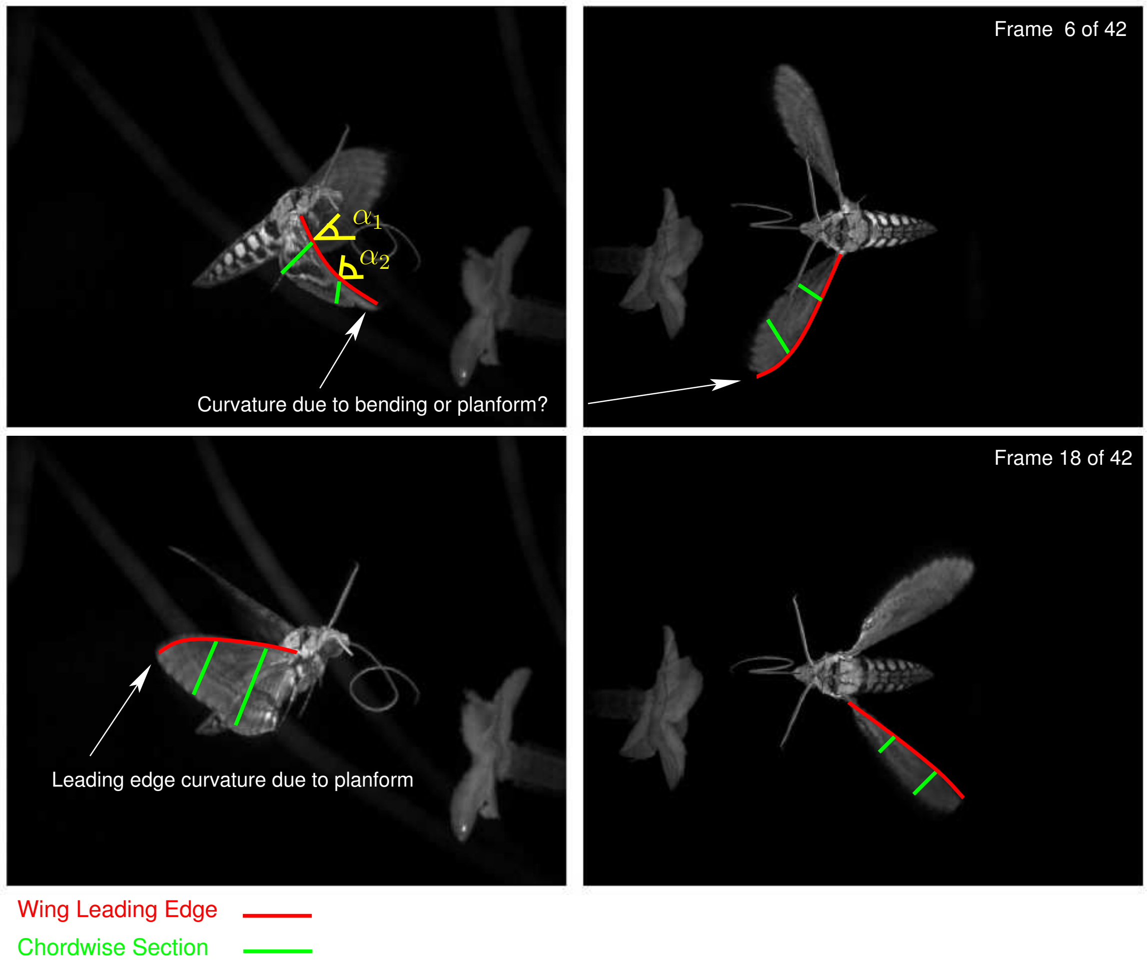

Figure 6: Estimating the relative magnitude of bending and torsion modes during the wing stroke is difficult to accomplish through qualitative observation alone. Choosing a single point of view to observe the dynamic structural response is complicated by the large amplitude wing rotations, and determining the relative contributions of the bending and torsion modes is complicated by the curvature of the leading edge of the Hawkmoth wing when using multiple points of view.

2.2 Analytic Aerodynamic Models

A variety of analytic models have been proposed for examining insect flight. The use of these methods has evolved along with our understanding of the aerodynamic phenomena associated with flapping wing flight. Early aerodynamic analytic models were based on quasi-steady aerodynamic assumptions. The blade element model is one such technique used to examine flapping wing fliers that idealized the wings as a set of "blade elements", or chordwise sections [39]. Aerodynamic forces for each chordwise section were based on a quasi-steady analysis of each blade element based on wing orientation and velocity. The wing velocity represents a combination of the flapping, forward, and induced velocity components. The induced velocity component were often based on a momentum jet analysis of the wake.

Models based on a momentum jet analysis allowed for mean aerodynamic performance and power requirements to be examined. The momentum jet approach idealizes the wing as an actuator disc which imparts momentum from the wing to the fluid. Aerodynamic forces and power may be predicted from an analysis of the farfield flow velocities. Because the wing is idealized as an actuator disc and depends on farfield wake characteristics, the influence of kinematic and geometric variations on the near-body wake are not included in the analysis [39].

Hybrid methods, which combine the blade element method with a modified momentum theory approach were proposed that allowed the influence of morphological, kinematic, and geometric variations on the mean aerodynamic force and power. The hybrid momentum jet was a modification of the blade element model which utilized a pulsed actuator disc to predict the induced velocity component [40, 41].

Other efforts were made to examine the time-dependent aerodynamic forces, such as the unsteady strip theory based on the Theodorsen function for harmonic pitching and plunging motions described by DeLaurier [42], and three-dimensional influences, such as the vortex lattice method described by Sunada *et al.* [43, 44] to examine three-dimensional oscillating flat plates. The strip method described by DeLaurier overcame the quasi-steady aerodynamic assumption by utilizing the Theodorsen function for harmonic pitching and plunging airfoils. However, the Theodorsen approximation is only valid for small oscillation amplitudes.

2.3 Physics Based Numerical Simulation

Physics based simulation is an alternative to analytical methods for examining the aerodynamic performance of flapping wing fliers. Smith [45] described the use of an unsteady panel method to examine the performance of a Hawkmoth during flight. The unsteady panel method utilized doublet panels to model the wing surface and the evolution of the unsteady wake in time. The unsteady panel method overcomes many of the limitation of the analytic models by treating the aerodynamic phenomenon as unsteady and allowing for a free-wake analysis. However, vortex panel methods are based on inviscid aerodynamic approximations and are unable to capture viscous effects, such as the laminar flow separation that produces the leading edge vortex characteristic of many natural fliers at low Reynolds numbers.

Time-accurate Navier-Stokes based simulation of flapping wing fliers have been demonstrated using a variety of approaches over the course of the last decade. Finite volume solutions using body conformal grids have been computed by Liu [20], Liu *et al.* [19], Aono [24], and Aono *et al.* [25], Sun and Tang [46, 47] and Sun *et al.* [48], among others. Other formulations of the Navier-Stokes equations have been utilized for simulating natural fliers, such as the finite element formulation demonstrated by Ramamurti and Sandberg [49, 50] and Hamamoto [51], and finite difference solutions using non-body conforming solution domains and immersed boundary conditions by Mittal [52, 53] and Mittal *et al.* [54].

2.4 Overview of the Aerodynamic Simulation Method

For the purpose of numerical simulation, the large amplitude wing motions may be represented, or resolved, into two components; a rigid body rotation with respect to the wing root, and local deformations and rotations with respect to the undeformed wing. The large amplitude rigid body motions for three-dimensional configurations have been accommodated using a variety of techniques, including mesh regeneration, mesh deformation, overset methods, and immersed boundary techniques. Each technique has advantages and disadvantages in terms of gridding the complex geometric configurations, solution efficiency, and the extensibility of the method for including fluid-structure interaction and modeling multiple moving components.

After reviewing the solution methods and solvers utilized in previous investigations and the available commercial flow solvers, the OVERFLOW solver was selected for use in the current research effort. The OVERFLOW solver was selected because it offers time-accurate low Mach number preconditioning [55], higher-order solution capabilities [56], dynamic rigid body solution capabilities [57], and aeroelastic simulation capabilities [58]. In addition to the solver capabilities, OVERFLOW is a NASA research code. As such, the use of the software is not license-limited in the AFIT HPC or the AFRL MSRC environments, and the source code is available for examination and modification.

2.5 Overview of the OVERFLOW Flow Solver

The OVERFLOW code is a compressible Navier-Stokes flow solver for structured overset solution domains based on a finite difference Navier-Stokes formulation. The OVERFLOW solver has undergone multiple revisions and branching since the original code development, as illustrated in Figure 7. The versions of the code of particular interest for the current study are OVERFLOW-D, which introduced dynamic simulation capabilities for rigid moving bodies, OVERFLOW-D2 which introduced fluid-structure interaction capabilities, and the current development branch, OVERFLOW 2.1, which introduced higher-order solution capabilities.

The current development version of OVERFLOW, version 2.1, is capable of fifth order spatial accuracy using the Weighted Essentially Non-Oscillatory (WENO) scheme [56] and second-order temporal accuracy using Dual Time Stepping [59]. OVERFLOW 2.1 is capable of modeling flow-fields characterized by mixed Mach numbers, such as those experienced by a rotorcraft in hover, through the use of low Mach number preconditioning. In addition to higher-order solutions at low or mixed Mach numbers, OVERFLOW 2.1 is capable of modeling dynamic rigid-body motion for multi-body problems with relative motion, including six-degree-of-freedom simulations for motion due to aerodynamic forcing. A brief description of the relevant OVERFLOW features for modeling flapping wing flight will be provided here, while a full examination of the OVERFLOW solver may be found in the OVERFLOW 2.1 documentation [60,61] and related publications [62,63,64,65,66,55,67,68].

2.5.1 Chimera Solution Approach.

The overset, or Chimera solution methods enable structured flow solvers to compute flow solutions for complex domains. Overset techniques simplify the generation of solution domains about complex geometries and configurations by allowing separate computational domains to overlap in physical space. By allowing computational domains to overlap in physical space, complex geometric features, or combinations of features that are difficult to model using a single structured solution domain may be modeled using multiple overlapping computational domains [69].

Because solution domains are allowed to overlap in the physical space, an extra boundary condition is required to accommodate the overlapping domains. The additional boundary condition is a variation on a block-to-block boundary condition for multi-block solvers, but instead of passing information across an edge or face, the overset boundary condition interpolates the flow solution from points in the overlapping solution regions [70].

Much of the additional computational overhead and complexity traditionally associated with the Chimera solution approach is related to establishing interpolation stencils between solution domains for the overlapping boundary condition, as well as the identification and blanking of cells, or points, that fall within a specified distance of solid bodies or domain boundaries in the overlapping regions. The Chimera solution approach requires that additional care be taken when integrating aerodynamic forces

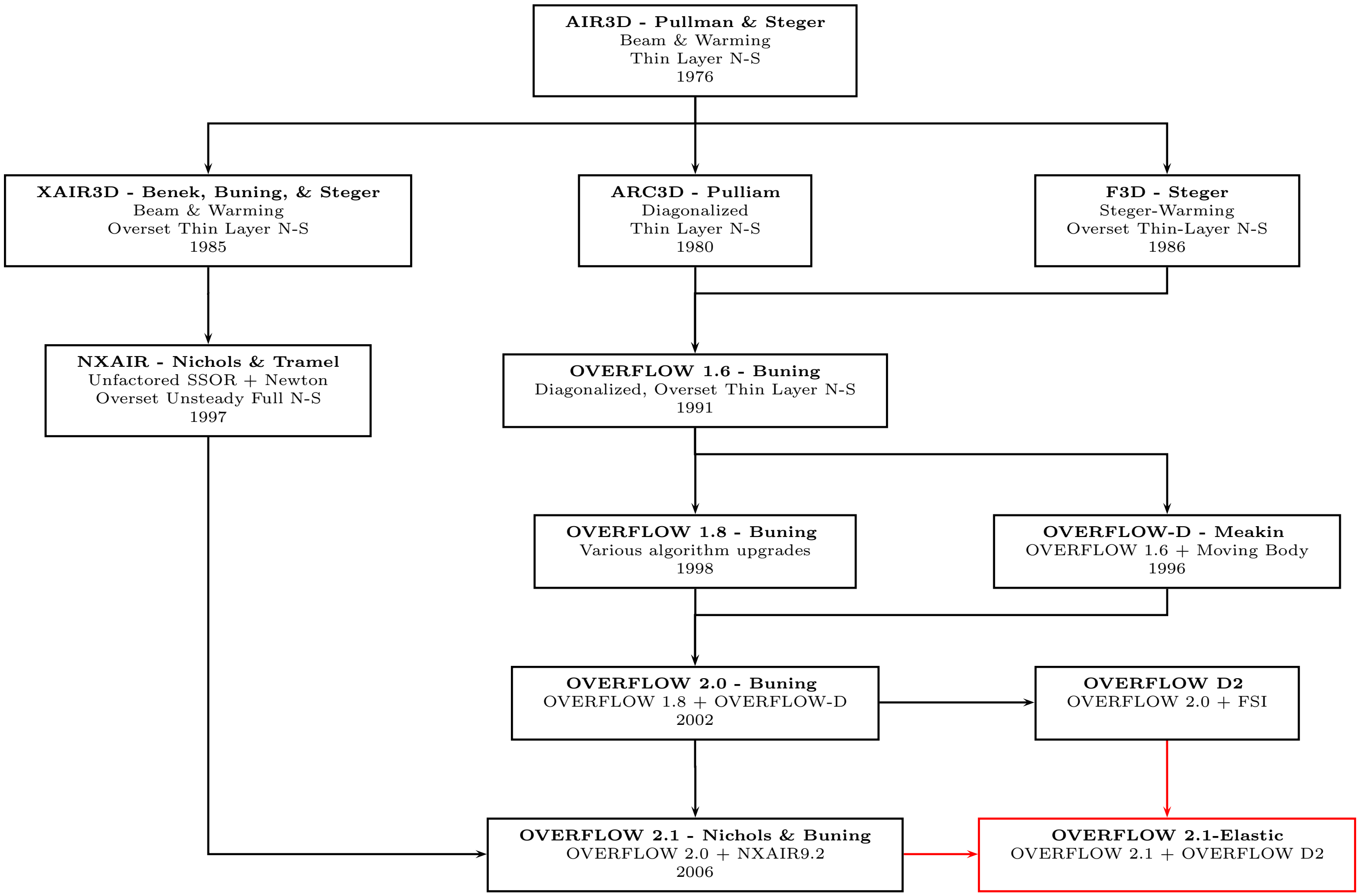

Figure 7: Evolution the OVERFLOW 2.1-Elastic flow solver developed for this study. OVERFLOW development history based on Slotnick [67].

and moments on surfaces with overlapping regions such that the overlapping regions are not integrated multiple times [71].

2.5.2 Dynamic Multi-body Simulation. The Chimera solution approach is well suited for computing dynamic or moving body flow simulations. Using the Chimera approach, computational domains may be grouped so as to represent a single water tight body. These grouped solution domains may be translated and rotated relative to other moving "bodies" or fixed solution domains. Because the solution domains are dynamic, the interpolation stencils and cell blanking required for the overlapping boundary condition must be updated at each time step for the new solution configuration. This introduces additional computational overhead at each time step. A constant cell quality may be maintained, however, and the overset method does not require the use of mesh deformation or mesh regeneration to represent rigid body motions [72].

OVERFLOW utilizes the Domain Connectivity Function utility (DCF) [60] incorporated from the OVERFLOW-D family of solvers to update hole-cutting and fringe point interpolations between near-body and off-body grids [73]. Arbitrary rigid body motion and domain grouping may be prescribed using the Geometry Manipulation Protocol (GMP) [74] or through a user defined subroutine [60]. OVERFLOW 2.1 also includes a six-degree of freedom (6DOF) model for computing rigid body motion due to aerodynamic forces.

2.5.3 Low Mach Number Preconditioning. The use of a compressible formulation of the Navier-Stokes equations, Equation (1), to compute the flow solution for configurations with low characteristic free-stream velocities generally results in poor solution accuracy and solution convergence [55]. The poor performance of the compressible formulation of the Navier-Stokes equations is caused by a large separation of the eigenvalues, Equation (2), which depend on the free-stream, or convective velocity, and the acoustic velocity, or speed-of-sound, which impose significant stability limitations for time marching solution methods.

$$\frac{\partial \vec{q}}{\partial t} + \frac{\partial \vec{E}}{\partial \xi} + \frac{\partial \vec{F}}{\partial \eta} + \frac{\partial \vec{G}}{\partial \zeta} = 0 \tag{1}$$

$$\lambda = \begin{bmatrix} U \\ U \\ U \\ U + c \\ U - c \end{bmatrix} \tag{2}$$

The efficient solution of low Mach number configurations may be achieved by using an incompressible formulation of the Navier-Stokes equations, such as the Marker-and-Cell (MAC) method of Harlow and Welch [75] or the Semi-Implicit Method for Pressure Linked Equations (SIMPLE) method of Patankar [76]. Alternatively, the compressible formulation of the Navier-Stokes equations may be modified with the addition of a pseudo-compressibility term that re-couples the conservation of mass and conservation of momentum equations for incompressible flows.

In order to solve low Mach number and mixed Mach number flows, OVERFLOW 2.1 incorporates the Smith-Weiss preconditioning scheme [55,61]. The Smith-Weiss preconditioning scheme introduces a preconditioning matrix, Γ_p, acting on the preconditioned conservative variables, $\vec{q}_p$. This formulation introduces a pseudo-time variable, τ, into the preconditioned Navier-Stokes equation, Equation (3).

$$\Gamma_p \frac{\partial \vec{q}_p}{\partial \tau} + \frac{\partial \vec{q}}{\partial t} + \frac{\partial \vec{E}}{\partial \xi} + \frac{\partial \vec{F}}{\partial \eta} + \frac{\partial \vec{G}}{\partial \zeta} = 0 \tag{3}$$

The preconditioned Navier-Stokes equation produces a set of eigenvalues, Equation (4), that are balanced at low Mach numbers.

$$\lambda = \begin{bmatrix} U \\ U \\ U \\ 0.5U\left(\beta+1\right) - \sqrt{0.5\left(\beta-1\right)^2 + \beta c^2} \\ 0.5U\left(\beta+1\right) + \sqrt{0.5\left(\beta-1\right)^2 + \beta c^2} \end{bmatrix} \tag{4}$$

This formulation depends on a "preconditioned" Mach number, β, which is defined in Equation (5).

$$\beta = \max\left[\min\left(M^2, 1\right), \beta_{min}\right] \tag{5}$$

In OVERFLOW 2.1, the default value of β_{min} is $3M^2_{REF}$. When used within a dual time stepping solution scheme, the implemented Smith-Weiss preconditioning provides a time-accurate solution when the pseudo-time variables reach convergence at each time step [60, 61].

2.5.4 Aeroelastic Framework. The OVERFLOW-D2 solver has been used to examine rotorcraft aeromechanics using both loose and tight coupled fluid-structure interaction (FSI) solution methods [57, 58, 77]. Loose aeroelastic coupling is implemented on a per-rotor revolution basis, while tight aeroelastic coupling may be achieved at the time iteration level. Both coupling methods utilize the same FSI framework which depends on external programs to provide structural deformations. Fortunately, the per-revolution loose coupling method has a corollary in the flapping wing problem. For a flapping wing flier, the wing kinematics for steady flight modes, both hover and forward flight, are time-periodic and may be mapped to a rotor revolution. Thus the loose coupling framework may be used to prescribe structural deformations on a per-flapping cycle basis.

2.5.5 Mesh Deformation. The OVERFLOW-D2 mesh deformation capabilities were developed for slender, elastic rotor blades exhibiting "beam" type deformations. Surface deformations and rotations are prescribed along an elastic axis as a function of span, r/R, and azimuth, $0 \leq \Psi \leq 2\pi$. Because of the focus on "beam" type deformations, the current mesh deformation implementation is unable to account for chord-wise deformations.

Surface deformations are interpolated for the rotor azimuth at each time step using a cubic spline which maintains C^1 continuity of the motion derivative in time. The computational surface is deformed using a transformation matrix incorporating both transformations and rotations. The computational volume is then deformed using the transformation matrix for each corresponding span-wise location. This algebraic method preserves grid quality and initial grid orthogonality at the boundary surface [58].

2.6 OVERFLOW 2.1-Elastic

In order to utilize the fluid-structure interaction capabilities of OVERFLOW-D2 and the higher-order solutions of OVERFLOW-2.1, the fluid-structure interaction framework and mesh deformation routines from OVERFLOW-D2, specifically OVERFLOW 2.0aa elastic 1.8, were incorporated into OVERFLOW-2.1h. This merged solver, developed by the author specifically for this research, is referred to as OVERFLOW 2.1-Elastic for the remainder of this document.

2.7 Summary

The Hawkmoth *Manduca sexta* was selected as the focus of this investigation based on the aerial capabilities of the Hawkmoth and the availability of an existing body of literature documenting the unsteady aerodynamic characteristics and the dynamic wing motions across a range of flight conditions. The aerodynamic phenomena utilized by the Hawkmoth to produce the aerodynamic forces are unsteady in nature and exhibit significant non-linearities in response to the dynamic wing motion.

In order to examine the influence of structural response on the unsteady aerodynamic phenomena and aerodynamic performance, the aerodynamic response will be simulated using Navier-Stokes based simulation using the OVERFLOW 2.1-Elastic flow solver. OVERFLOW 2.1-Elastic was developed specifically for this study, and represents an enhancement of OVERFLOW 2.1, which incorporates higher order solution capabilities, with the fluid-structure interaction capabilities of OVERFLOW-D2.

III. Verification and Validation of OVERFLOW 2.1-Elastic

Verification and validation of OVERFLOW 2.1-Elastic focused on two main tasks, demonstrating that the modified solver retained the baseline solution capabilities of OVERFLOW 2.1, and demonstrating the ability of OVERFLOW 2.1-Elastic to adequately capture the unsteady aerodynamic phenomena exhibited by the Hawkmoth in flight, as discussed in the previous chapter. The ability of OVERFLOW 2.1-Elastic to capture unsteady low-Mach number flows was demonstrated by computing the flow field about a two-dimensional circular cylinder in a cross flow across a range of Reynolds numbers. The circular cylinder solutions demonstrate the steady state, time-accurate, and dynamic solution capabilities of OVERFLOW 2.1-Elastic.

An additional demonstration of the dynamic solution capabilities at low Mach numbers was based on a two-dimensional heaving airfoil solution for which experimental flow measurements were available. The ability of OVERFLOW 2.1-Elastic to capture the unsteady aerodynamic phenomena exhibited by the Hawkmoth in flight was demonstrated for a baseline three-dimensional test case that produced sufficient vertical force to sustain the weight of a typical Hawkmoth at hover.

3.1 Cylinder in Cross-flow

The circular cylinder in cross-flow is a useful test case to examine both the steady and unsteady solution capabilities of OVERFLOW 2.1-Elastic. The circular cylinder in a cross-flow exhibits distinct flow characteristics that depend on Reynolds number. Of interest for this study are the steady flow regime between Reynolds number 5 and 45 in which the wake forms a laminar separation bubble on the downstream side of the cylinder, and the unsteady flow regime between Reynolds number 50 and 185 in which the laminar wake forms a two-dimensional von Karman vortex street downstream of a three-dimensional cylinder [78, 79].

3.1.1 Laminar Separation Bubble. At Reynolds numbers between 5 and 45 a laminar separation bubble, or recirculation, forms on the downstream side of a circular cylinder in cross-flow. The length of the recirculation region, L, relative to the diameter, D, of the cylinder, L/D, depends on the diameter based Reynolds number of the flow, $Re = DU/\nu$. To demonstrate the ability of the code to resolve the laminar separation at low Reynolds numbers, two-dimensional solutions were computed for Reynolds numbers between 15 and 40 in increments of 5.

Solutions were computed using a single O-type solution domain with 201 points in the circumferential direction and 201 points in the radial direction. The far field boundary was located at $95D$ from the cylinder surface, which had an initial spacing of $0.001D$. Solutions were computed using the HLLC upwind scheme for the Euler terms and the D3ADI algorithm with Huang sub-iteration for the viscous terms with a van Albada limiter. Solutions were computed using a freestream Mach number of 0.2 with low Mach preconditioning enabled [61].

The length of the laminar separation bubble produced by the steady simulations was determined by examining the u-velocity profile along the cylinder centerline extending in the freestream direction shown in Figure 8. The u-velocity component is negative within the separation bubble, transitioning to positive values outside the recirculation region. The length of the separation bubble expressed in units of L/D is compared to experimental values and previous numerical simulations in Figure 8. The current simulations provide good agreement to the previous experimental and numerical result presented in Bush and Baeder [79].

3.1.2 Unsteady Solution, $Re > 35$. At Reynolds numbers above 45, flow instabilities related to the length of the laminar separation bubble lead to a time-dependent wake. At Reynolds numbers between 50 and 185, the stationary circular cylinder produces a two-dimensional time-periodic wake structure in which vortices of alternating strength are shed from the cylinder and convect downstream. The shedding frequency of this von Karman vortex street can be expressed using a non-dimensional Strouhal number, $St = fD/U$, which exhibits a dependence on Reynolds number.

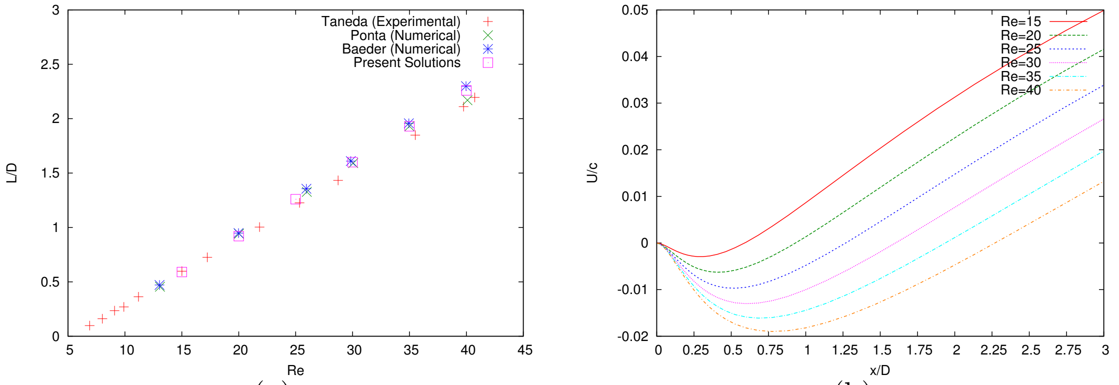

(a) (b)

Figure 8: L/D as a function of Reynolds number (a) and the u-velocity profile behind the cylinder as a function of x/D (b). Reference data digitized from Bush and Baeder [79].

Time-accurate solutions utilizing the same single block solution domain described for the steady solutions were computed at Reynolds numbers 60, 120, and 185 to demonstrate the ability of the low Mach number preconditioning to capture a time-dependent flow field. Solutions were computed using a non-dimensional time step of 0.005 with 20 dual time iterations per time step.

The non-dimensional shedding frequencies and force histories predicted by OVERFLOW 2.1-Elastic exhibit similar trends to those documented in previous experimental and numerical investigations, shown in Figure 9. The mean drag and r.m.s. lift for the solution at Re 185 are compared to previous numerical solutions of Guilmineau [80] presented in Table 1. The OVERFLOW 2.1-Elastic solution at Reynolds number 185 over-predicts mean drag and r.m.s. lift by 8% and 12% when compared to Lu and Dalton [81].

3.1.3 Prescribed Transverse Oscillation, Re = 185.

Dynamic motion of a circular cylinder influences the vortex wake and force history when compared to the wake produced by a stationary circular cylinder. An oscillating cylinder will experience a phase jump in the vortex wake for a frequency of excitation, f_e, near the natural shedding frequency, f_o [80]. This phenomenon was utilized to demonstrate

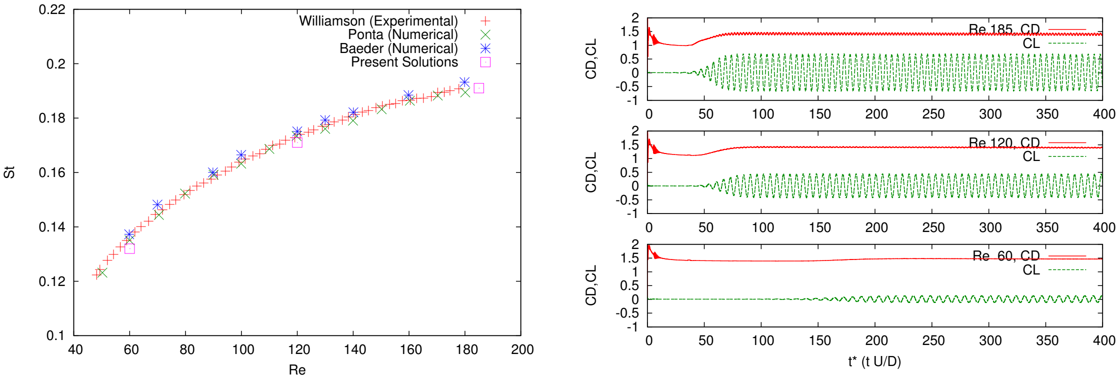

(a) (b)

Figure 9: Strouhal number as a function of Reynolds number (a) and the lift and drag history (b). Reference data digitized from Bush and Baeder [79].

Table 1: Comparison of the mean drag and r.m.s. lift produced by a circular cylinder at Reynolds number 185 to previous numerical simulations.

Source	Re	CD_{mean}	$CL_{\texttt{r.m.s}}$	St	Method
Present Simulation	60	1.47	0.088	0.132	Numerical
Present Simulation	120	1.41	0.304	0.171	Numerical
Present Simulation	185	1.42	0.477	0.191	Numerical
Lu and Dalton [81]	185	1.31	0.422	0.195	Numerical
Guilmineau [80]	185	1.29	0.443	0.195	Numerical

the ability of OVERFLOW 2.1-Elastic to simulate the unsteady flow field about a moving body.

Solutions were computed at Reynolds number 185 for excitation frequencies of f_e/f_o of 0.9 and 1.0 with an oscillation amplitude, A_e, of $0.2D$ to match previous solutions computed by Guilmineau and Queutey [80]. The behavior of the lift and drag force histories match those computed by Guilmineau and Queutey [80], as shown in Figure 10 (b). As with the stationary shedding cylinder, OVERFLOW 2.1-Elastic over predicts both lift and drag. However, OVERFLOW 2.1-Elastic does capture the trends in the mean drag and r.m.s lift exhibited by the transversely oscillating cylinder at different frequencies, shown in Figure 10 (a).

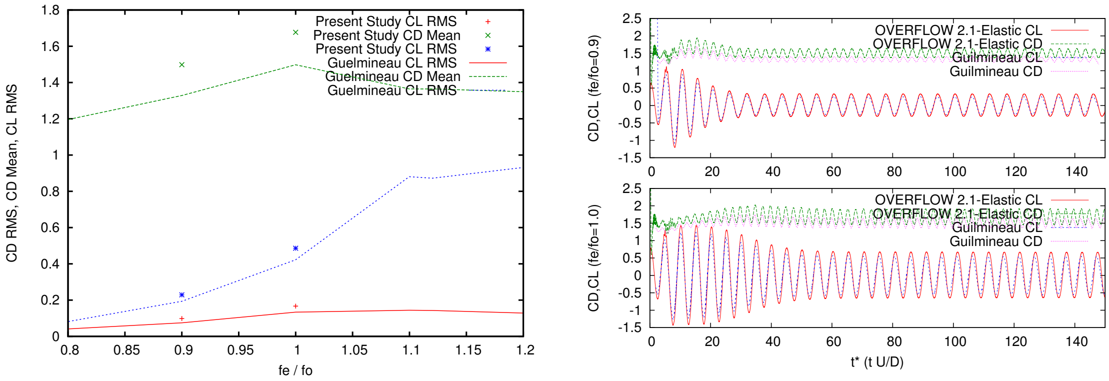

(a) (b)

Figure 10: Lift and drag as a function of f_e/f_o for an oscillation amplitude of $0.2D$, (a), and force histories (b). Reference data digitized from Bush and Baeder [79].

3.2 *Two-Dimensional Airfoil*

Additional two-dimensional dynamic solutions were used to demonstrate the ability of OVERFLOW to capture the time-dependent flow-field generated by a moving, or dynamic body at Reynolds numbers characteristic of the three-dimensional flapping wing problem. Solutions were computed to match experimental data for a SD7003 airfoil recorded in the AFRL Horizontal Free-surface Water Tunnel. Experimental data were available for sinusoidal heaving motions at Reynolds number 10,000.

The data set includes wake visualization using dye injection at the leading and trailing edges, as well as time-averaged velocity and vorticity measurements obtained with particle image velocimetry (PIV) [82]. Forces were not measured in the experimental investigation.

The two-dimensional heaving solutions were computed for a constant pitch angle of $\alpha(t) = 4$ degrees and a non-dimensional heaving amplitude of $h(t) = 0.05 \cos(\omega t)$ at a reduced frequency of $k = 3.93$. Solutions were computed at a chord-based Reynolds number of 10,000 to match the experimental conditions. At this Reynolds number the flowfield should remain laminar. Solutions were computed using low Mach number preconditioning at a freestream Mach number of 0.015.

The experimental data set does not include force measurements. Thus, the simulated flowfield was qualitatively compared to the experimental measurements of velocity magnitude in Figure 11 and vorticity magnitude in Figure 12. The time-dependent wake structures predicted by the OVERFLOW 2.1-Elastic solution achieve a good qualitative match to the wake structures documented in the experimental data set.

The heaving airfoil produced small vortical structures caused by flow separation close to the leading edge during the downward phase of motion, as seen in Figure 13. As the wing heaves, the vortex convects along the upper surface, slowing about the mid chord, then accelerating until it convects into the freestream from the trailing edge. The OVERFLOW 2.1-Elastic solution captures this unsteady phenomenon, which would likely be missed by lower order models.

3.3 3D Flapping Wing

The three-dimensional configuration is based on the geometry and dynamic wing motion of the Hawkmoth at hover. Published examinations of the Hawkmoth aerodynamics include a variety of numerical and experimental investigations that have documented the characteristic aerodynamic phenomena. However, precise experi-

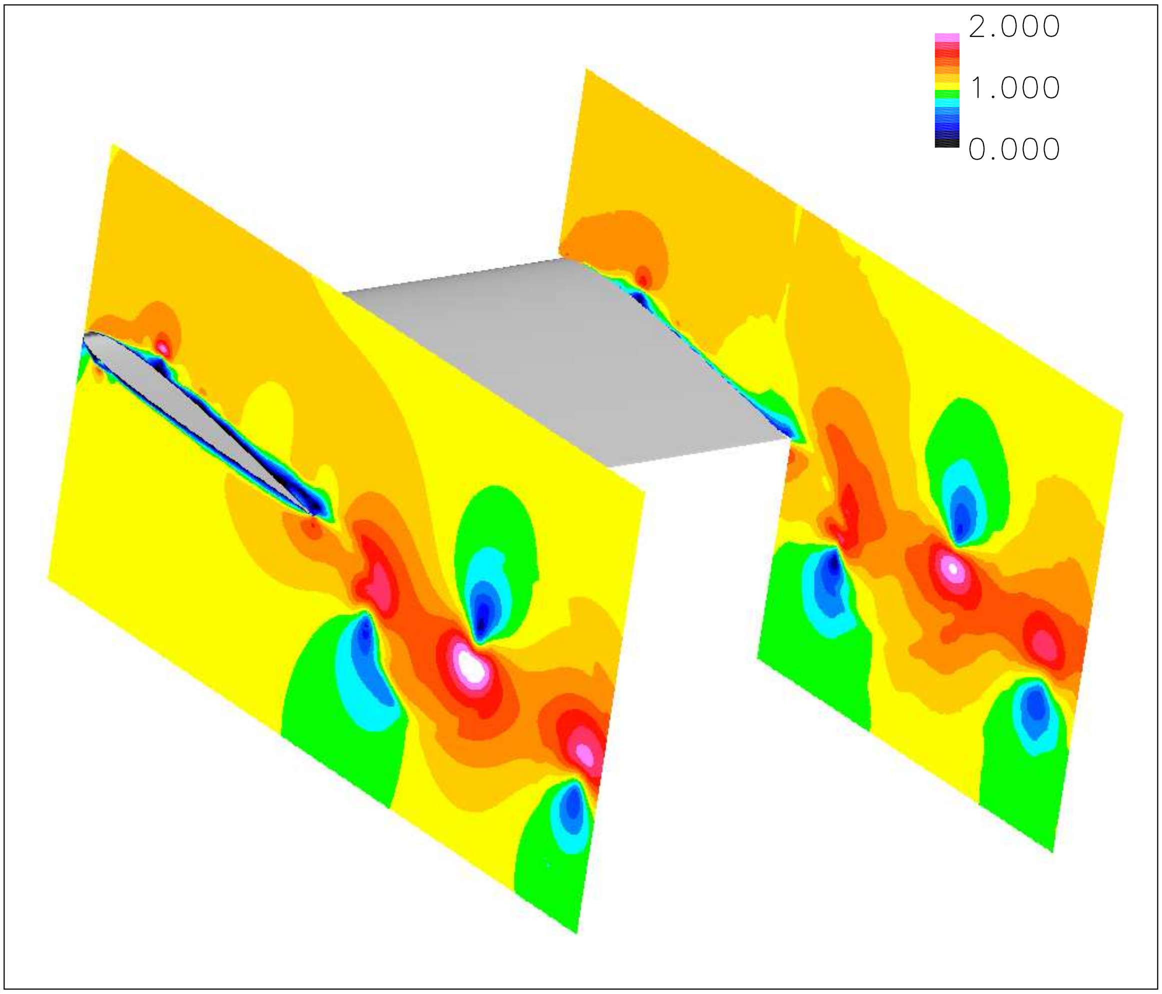

Figure 11: Contours of velocity magnitude normalized by freestream velocity for a heaving airfoil predicted using OVERFLOW 2.1-Elastic, left, and measured using PIV in the AFRL Horizontal Free-surface Water Tunnel, right. The CFD solution represents a single snapshot in time while the PIV represents a mean velocity magnitude over multiple snapshots at $t/\tau = 0$. The non-dimensional heaving motion is defined as $h(t) = 0.05cos(\omega t)$ and $\alpha(t) = 4$ for a reduced frequency of $k = 3.93$.

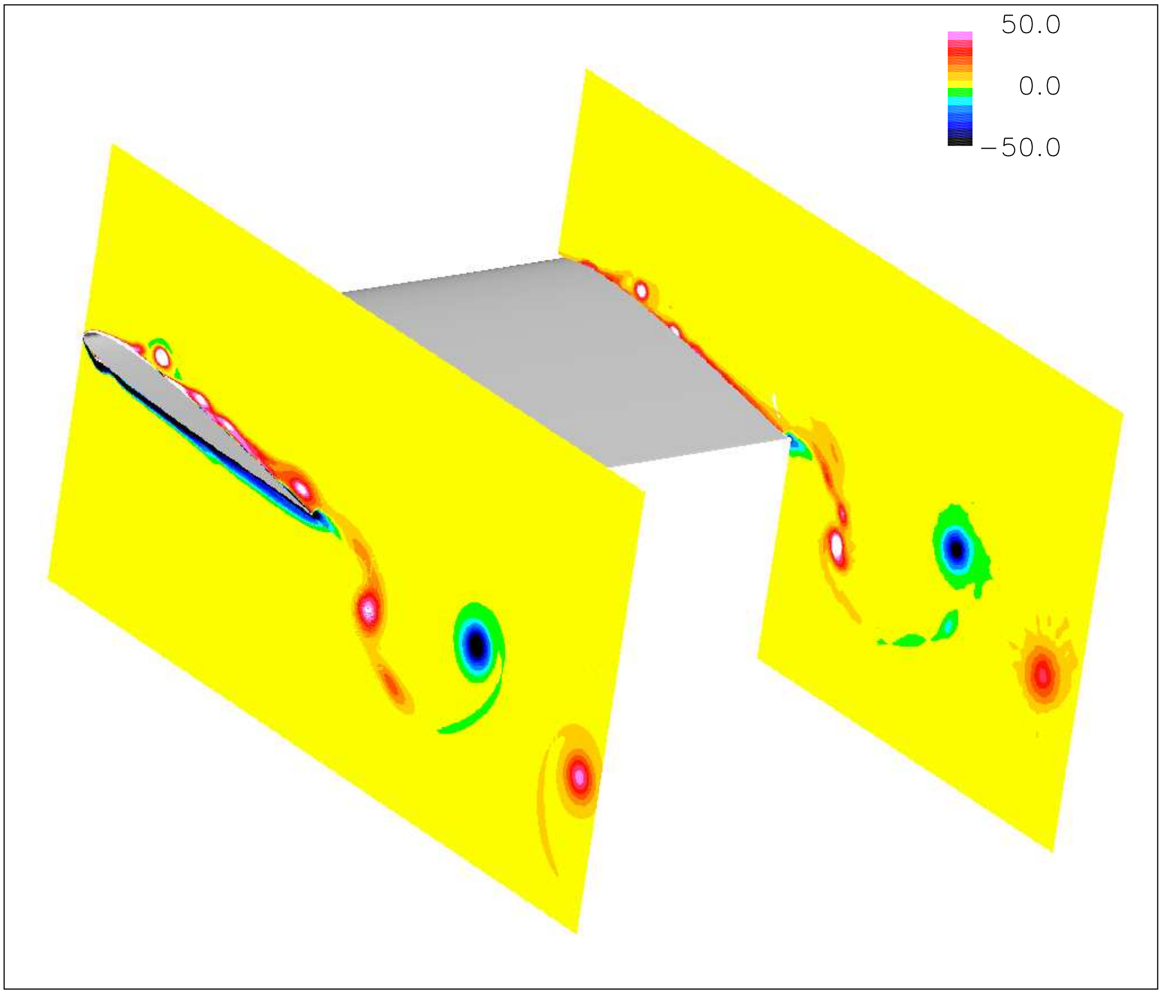

Figure 12: Contours of vorticity magnitude normalized by freestream velocity normal to the cut planes for a heaving airfoil predicted using OVERFLOW 2.1-Elastic, left, and measured using PIV in the AFRL Horizontal Free-surface Water Tunnel, right. The CFD solution represents a single snapshot in time while the PIV represents a mean velocity magnitude over multiple snapshots at $t/\tau = 0$. The non-dimensional heaving motion is defined as $h(t) = 0.05cos(\omega t)$ and $\alpha(t) = 4$ for a reduced frequency of $k = 3.93$.

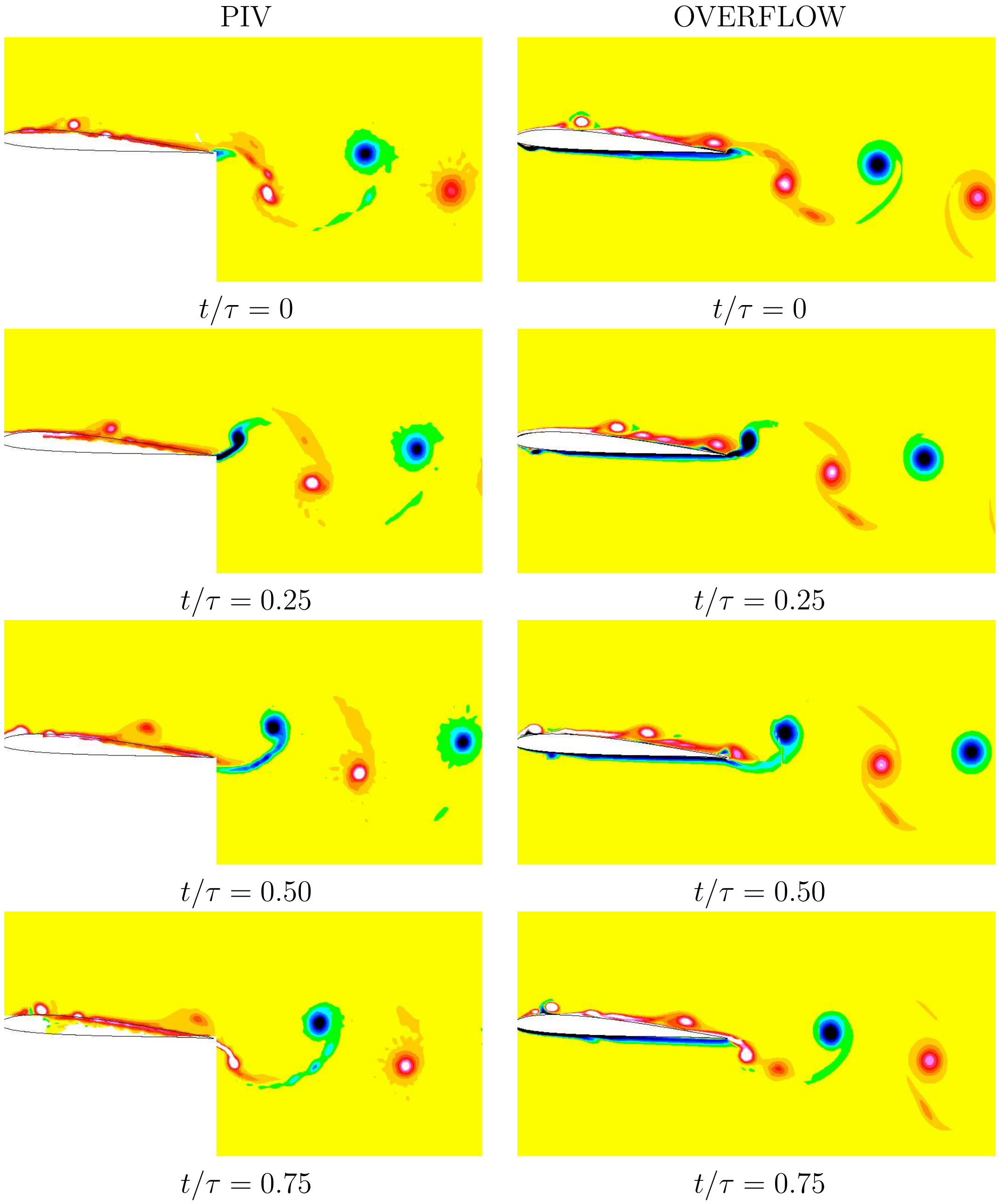

PIV

OVERFLOW

$t/\tau = 0$ $t/\tau = 0$

$t/\tau = 0.25$ $t/\tau = 0.25$

$t/\tau = 0.50$ $t/\tau = 0.50$

$t/\tau = 0.75$ $t/\tau = 0.75$

Figure 13: Contours of vorticity magnitude normalized by freestream velocity normal to the cut planes for a heaving airfoil measured using PIV in the AFRL Horizontal Free-surface Water Tunnel and predicted using OVERFLOW 2.1-Elastic.

mental measurements of the aerodynamic force histories produced by the Hawkmoth during flight are still elusive. Direct measurement of the aerodynamic forces are complicated by the small force amplitudes and high frequencies, as well as the need to differentiate the inertial elastic forces and the aerodynamic forces from a single signal.

The lack of experimentally determined, time-resolved aerodynamic forces limits the validation of three-dimensional flapping wing simulation to an order of magnitude comparison of the mean value of the simulated force history and the force required to support the weight of a typical Hawkmoth during hover. Beyond the single-point validation, the ability of the Navier-Stokes simulations to capture the documented unsteady aerodynamic phenomena provides further confidence in the simulation methods.

Numerical simulations may also be compared to prior simulation efforts, although the utility of a comparison to prior works depends on the specific configurations being compared. Geometric influences, such as wing planform and wing-body configurations, kinematic variations, and assumptions inherent in the simulation method can all influence the predicted aerodynamic forces. Details of the solution configuration used in this study are discussed in Chapter IV.

3.3.1 Test Configuration. The characteristic configuration developed for this study uses a symmetry solution for a single wing with a length of 50 millimeters, offset 20 millimeters from the centerline symmetry plane. Two wing planforms were considered, a Hawkmoth wing planform based on the work of Liu [20], and a rectangular wing with NACA 0009 cross section and a 30% wing chord, shown in Figure 14. For each planform, the kinematic rotations are prescribed about the intersection of the leading edge and the wing root. The large centerline offset was required in order to resolve the rigid body rotations while preventing the trailing edge of the wing from intersecting the idealized body, when included, or the symmetry plane.

The rigid wing rotations were based on the kinematic parameters documented by Willmott and Ellington [17,6] for a tethered Hawkmoth at hover. These kinematic

Table 2: Current and published mean aerodynamic forces for Hawkmoth hover simulations. Forces are presented for single wing symmetry solutions. Thrust to weight ratio, T/W, computed based on a mass of 1.48 grams.

Planform	Rectangular	*Manduca sexta*	*Agrius convolvuli*
Study	Current Work	Current Work	Aono and Liu [22]
Fx (N)	7.24×10^{-04}	8.42×10^{-04}	1.20×10^{-03}
Fy (N)	-1.46×10^{-03}	-1.65×10^{-03}	-1.20×10^{-03}
Fz (N)	7.26×10^{-03}	6.16×10^{-03}	8.48×10^{-03}
T/W	1.0	0.8	1.2

parameters formed the basis for previous numerical simulations by Liu *et al.* [20, 19] and Aono *et al.* [22, 24, 25]. In both cases, a 4-term Fourier approximation of the experimental data set was used to define the dynamic wing motions for the numerical simulations.

3.3.2 Aerodynamic Forces. Simulations using the Liu Hawkmoth planform and the rectangular planform produced mean vertical forces able to sustain the mass of a Hawkmoth at hover, as outlined in Table 2. These mean aerodynamic forces are comparable to the published simulation of Aono and Liu [22]. However, the time history of the vertical forces does vary between the simulations, as shown in Figure 15. The time resolved aerodynamic forces computed for the rectangular wing and the Hawkmoth planform exhibit a somewhat decreased lift amplitude compared to the forces computed by Aono and Liu [22], but match the shape of the force history and the phase of the peak force magnitudes. In particular, the current simulations capture the "double bump" exhibited during both half-strokes of the 4-term rigid wing simulations. Variations in the wing planforms, based on the species *Agrius convolvuli* in the case of the Aono simulations, the location of the wing root, or simulation configuration could account for the variation in the force magnitudes. These variations also influence the time history of the aerodynamic power, shown in Figure 16.

3.3.3 Wake Structures. The ability of the mean vertical force component to sustain the mass of the Hawkmoth at hover provides a single point validation

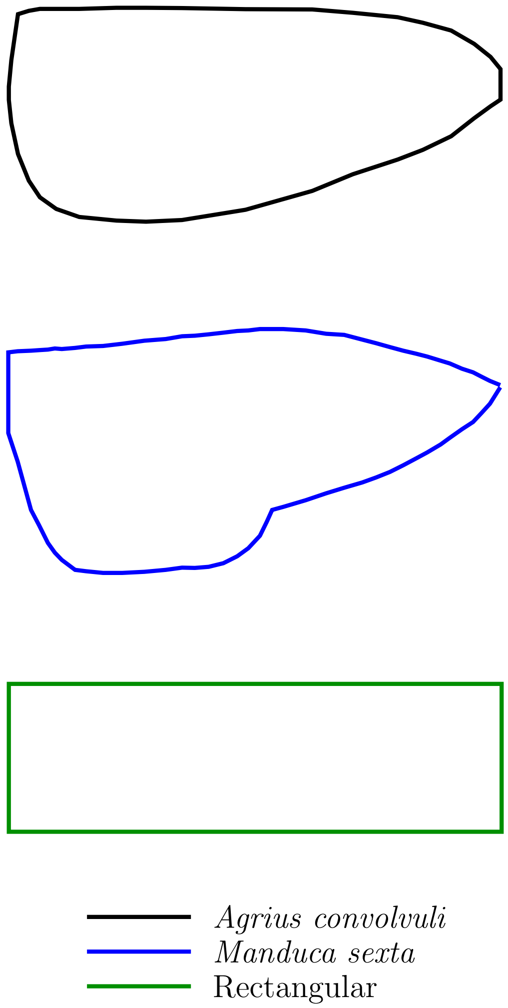

Figure 14: Wing planforms based on the *Manduca sexta* used by Liu and Kawachi [20], the *Agrius convolvuli* used by Aono and Liu [22], and the Rectangular wing planform used in the current work.

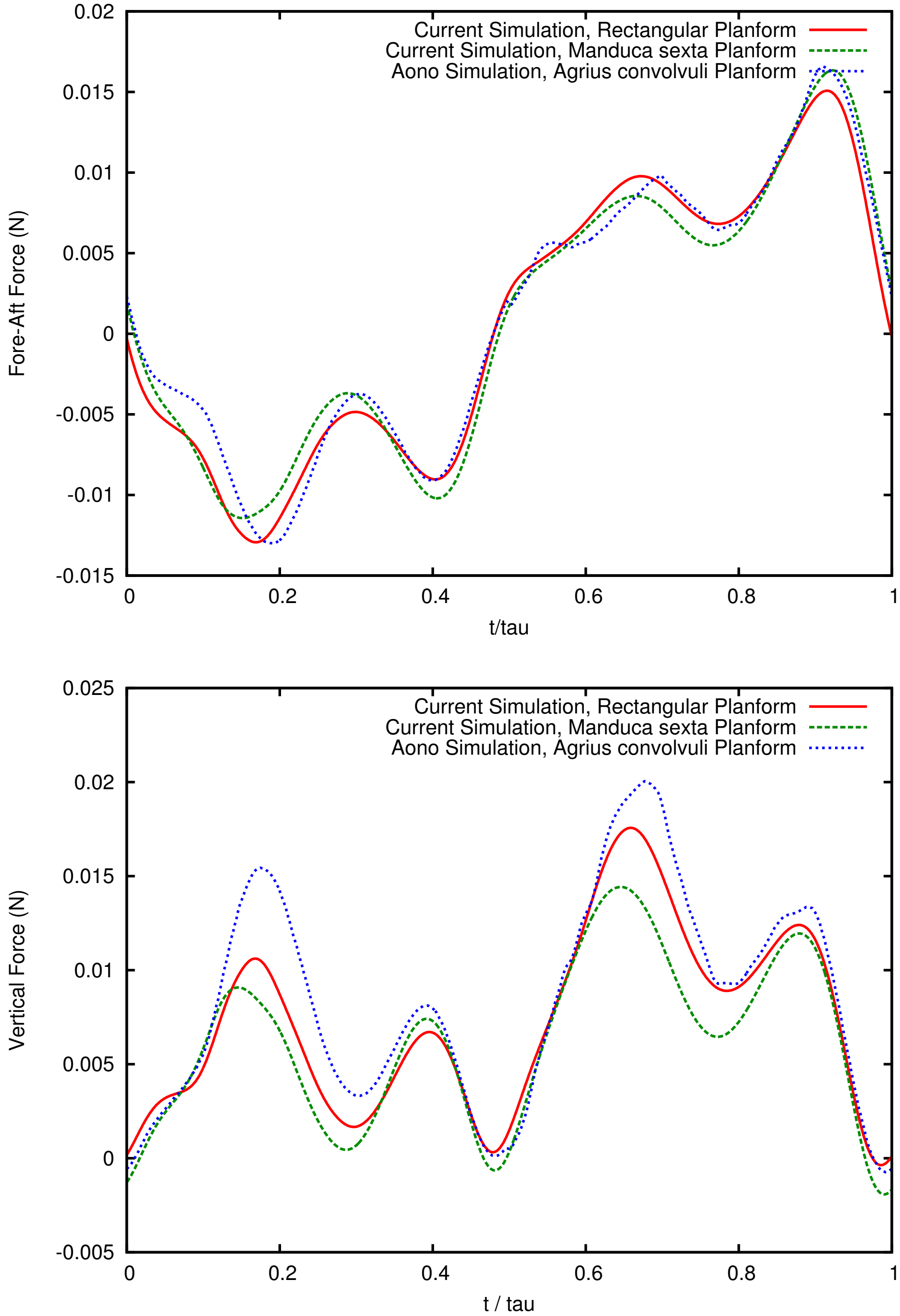

Figure 15: Time resolved rearward and vertical force histories for the Hawkmoth at hover. Force histories represent a current simulation for a rectangular planform, a current simulation for the *Manduca sexta* planform, and digitized forces computed by Aono and Liu [22] using the *Agrius convolvuli* planform.

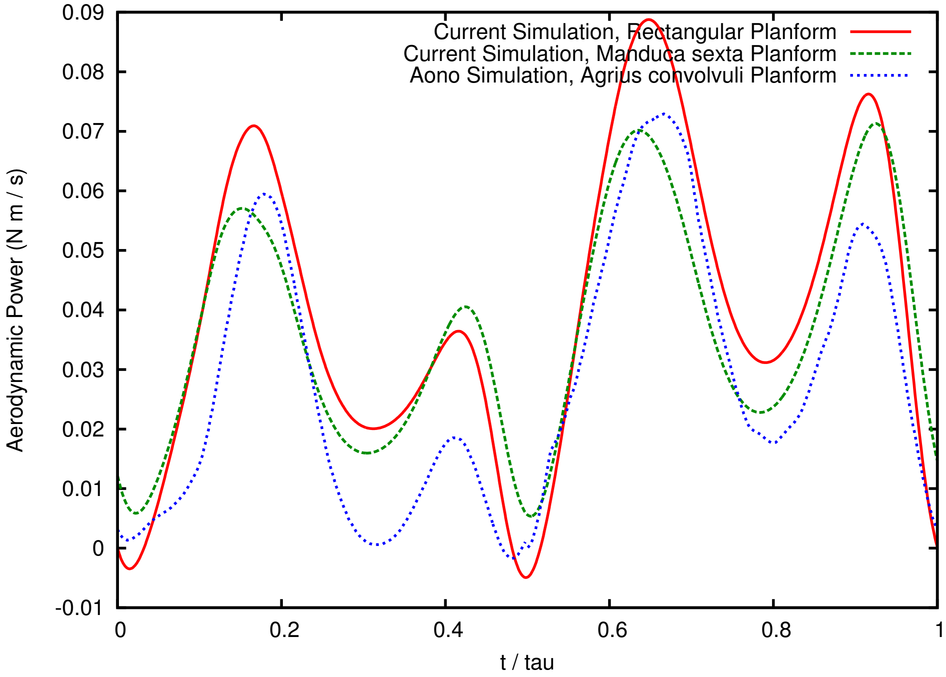

Figure 16: Time resolved aerodynamic power history for a rectangular planform, a current simulation for the *Manduca sexta* planform, and digitized aerodynamic power computed by Aono and Liu [22] using the *Agrius convolvuli* planform.

of the aerodynamic forces predicted by the Navier-Stokes simulation. Comparing the aerodynamic phenomena exhibited by the time-accurate Navier-Stokes simulation to previously documented aerodynamic phenomenon and wake structures provides confidence that the Navier-Stokes simulation is capturing the relevant aerodynamic phenomena.

The rectangular and Hawkmoth planforms each produce the characteristic wake structures previously documented for the Hawkmoth at hover using experimental [15, 16] and numerical [19, 24] investigations. The leading edge vortex and tip vortex documented by van den Berg and Ellington [16] are shown in Figure 17 along with vortical wake structures produced by the rectangular wing planform. The present simulations capture the characteristic horseshoe wake structure formed by the leading edge vortex, the tip vortex, and the vortices shed at the start of the half-stroke, highlighted in Figure 17. The smoke visualizations used by van den Berg and Ellington [15, 16] highlight the leading edge vortex and the evolution of the tip vortex, but do not highlight the other wake structures such as the starting and stopping vortices that may be seen in the wake structures produced by the present simulations. Examining the wake produced by the rectangular wing planform at the end of the upstroke, shown in Figure 18, shows the shed circulation at the trailing edge of the wing as well as three-dimensional influences at the wing root produced by the rigid wing rotations.

3.3.4 Summary. The three-dimensional simulations based on the rectangular wing planform and the Hawkmoth planform first used by Liu produce the aerodynamic forces necessary to sustain the weight of a Hawkmoth at hover. In addition, the simulations reproduce the characteristic aerodynamic phenomena previously documented for the Hawkmoth at hover.

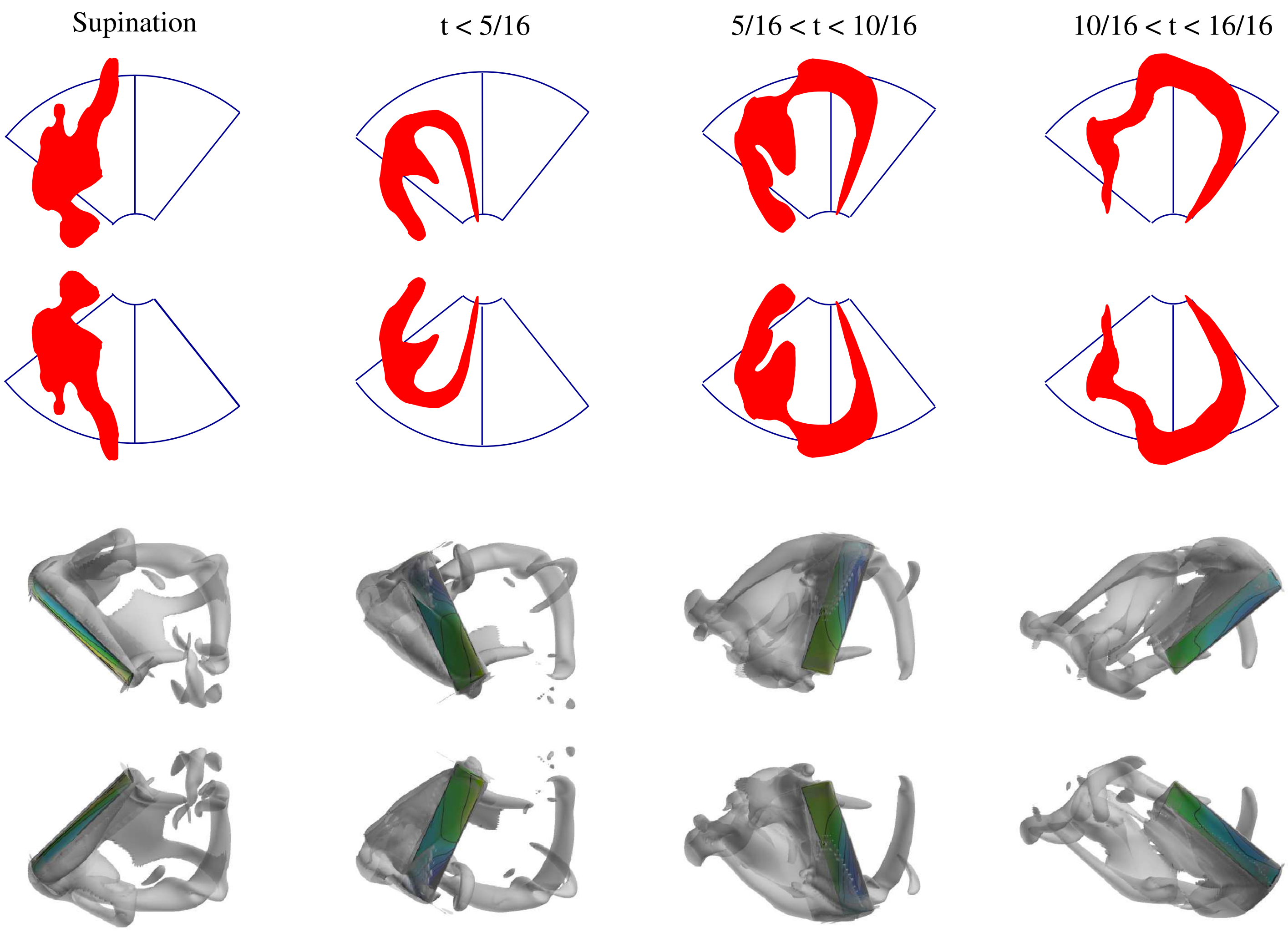

Figure 17: Leading edge vortex and tip vortex structures documented by van den Berg and Ellington [16] using a scaled mechanical flapping mechanism, shown in red, and the wake structures produced by a rigid rectangular planform, below, using contours of vortcity magnitude. The vorticity contours show all the near body wake structures, not just the leading edge vortex and tip vortex highlighted using smoke visualization by van den Berg and Ellington.

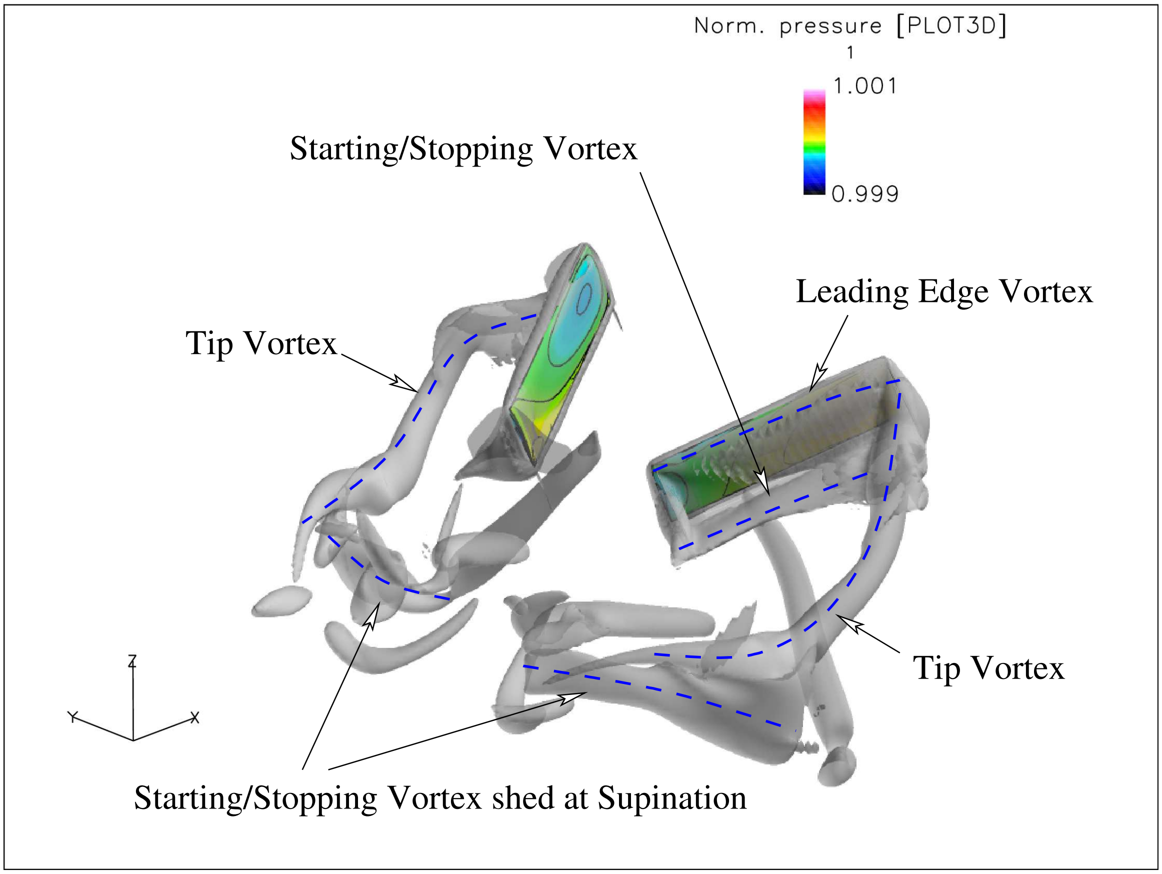

Figure 18: Vortical wake structures at the end of the upstroke. The vortical structures shed at the beginning of the stroke can be seen in the fore-field, combining with the tip vortex and the leading edge vortex to form a horseshoe vortex. The Leading edge vortex has not yet shed into the wake as the wing rotates about the leading edge.

IV. Configuration Study

In order to understand how geometric variations influence the predicted aerodynamic performance of the Hawkmoth at hover, a configuration study was performed that considered the influence of wing planform, wing-body interactions, and wing length on the time resolved aerodynamic forces, unsteady aerodynamic phenomena, and overall performance metrics. By understanding how the geometric properties influenced the numerical simulations, a baseline, or characteristic configuration was developed which reproduced the previously documented aerodynamic attributes for the Hawkmoth at hover while being easily reproducible and requiring a reasonable amount of computational resources.

4.1 Performance Metrics

In order to understand the influence of configuration on performance, simulations were examined using a set of quantifiable performance metrics based on the computed aerodynamic forces and aerodynamic power. The ability of the configuration to reproduce the characteristic aerodynamic phenomena was based on a qualitative assessment of the wake structure and unsteady aerodynamic mechanisms.

4.1.1 Aerodynamic Forces and Moments. When computing time-accurate solutions, OVERFLOW 2.1-Elastic reports aerodynamic force and moment coefficients as a function of time step in the *fomoco.out* output file for each integration surface defined in the MIXSUR input file, *mixsur.inp.* The force and moment coefficients reported in the FOMOCO output are non-dimensionalized by the reference velocity defined in the OVERFLOW input deck and the surface area defined for each integration surface in the MIXSUR input.

$$CF^*_{FOMOCO} = \frac{F}{0.5\rho_{REF}U^2_{REF}S_{REF}} \tag{6}$$

$$CM^*_{FOMOCO} = \frac{M}{0.5\rho_{REF}U^2_{REF}S_{REF}L_{REF}} \tag{7}$$

For dynamic solutions, the position, orientation, and non-dimensional velocity of each moving component are recorded in the ANIMATE output file, *animate.out*. The ANIMATE output also includes the non-dimensional forces and moments for each moving component.

$$F^*_{ANIMATE} = \frac{F}{\rho_{REF} U^2_{REF} L^2_{REF}} \tag{8}$$

$$M^*_{ANIMATE} = \frac{M}{\rho_{REF} U^2_{REF} L^3_{REF}} \tag{9}$$

From this data, mean and peak aerodynamic forces may be computed. In addition, the time resolved forces may be combined with the prescribed wing kinematics to examine the phase relationships between the aerodynamic forces and the prescribed wing motions.

4.1.2 Aerodynamic Power and Efficiency. For dynamic solutions, the ANIMATE output may be used to compute the aerodynamic power for each moving component. The aerodynamic power required to actuate a rigid body may be computed using the inner product of the aerodynamic forces and moments with the body's translational and rotational velocities using Equation (10).

$$P_{aero} = \vec{M}_{aero} \cdot \vec{\dot{\theta}}_{wing} + \vec{F}_{aero} \cdot \vec{v}_{wing} \tag{10}$$

The aerodynamic power may be used to compute an aerodynamic efficiency based on the ratio of vertical aerodynamic force component to aerodynamic power.

$$\eta_{aero} = \frac{F_{vertical}}{P_{aero}} \tag{11}$$

This efficiency is analogous to the definition of Power Loading, PL, used in the rotor craft community [83].

4.1.3 Inertial Power. Included in the ANIMATE output are the rotational velocities of each moving component in the body reference frame. This allows for a simplified computation of inertial power requirements for rigid body motion. The inertial power for the rigid body wing motion may be computed using the inertial moment at the wing root and the rotational velocities due to the wing motion.

$$P_{inertial} = \vec{M}_{inertial} \cdot \dot{\vec{\theta}}_{wing} + \vec{F}_{inertial} \cdot \vec{v}_{wing} \tag{12}$$

The moment at the wing root due to inertial forces for a rigid wing may be computed using the inertia tensor and rotational accelerations due to body motion.

$$\vec{M}_{inertial} = [I]\, \ddot{\vec{\theta}}_{wing} \tag{13}$$

The inertia tensor, $[I]$, represents the mass distribution of the specific wing configuration being studied. The center of mass of various insect wings have been previously documented [12,30], which may be used to approximate an inertia tensor. In the case of a flexible wing structure, the inertia tensor will be time variant with the structural response. As with the aerodynamic power, the inertial power may be used to compute an inertial efficiency metric.

$$\eta_{inertial} = \frac{|F_{inertial}|}{P_{inertial}} \tag{14}$$

4.1.4 Aerodynamic Force and Moment as a Function of Span. Included as part of the fluid-structure coupling framework in OVERFLOW 2.1-Elastic, aerodynamic forces and moments are reported as a function of span along the elastic axis defined for each flexible body. These aerodynamic forces may be reported as lumped aerodynamic forces for each wing section or as a force per unit span based on the **&EROTOR** namelist inputs. The ROTOR forces are non-dimensionalized by reference parameters specified in the **&EROTOR** namelist in the OVERFLOW input deck.

$$F^*_{ROTOR} = \frac{F}{0.5\rho_{ROTOR}(a_{ROTOR}M_{rotor})^2 L^2_{REF}} \tag{15}$$

$$M^*_{ROTOR} = \frac{M}{0.5\rho_{ROTOR}(a_{ROTOR}M_{rotor})^2 L^3_{REF}} \tag{16}$$

Visualizing the aerodynamic forces as a function of span provides insight into the force distribution along the wing surface, and provides insight into which regions of the wing contribute to the vertical and side force production throughout the wing stroke.

4.1.5 Non-dimensionalization Based on Tip Velocity. Non-dimensional aerodynamic forces and moments as defined above are based on an arbitrary reference velocity which does not have significant meaning as the freestream velocity approaches zero. However, an alternate non-dimensionalization for a flier in a hover condition may be formulated based on the maximum tip velocity of the oscillating wing.

$$CF^{*t} = \frac{F}{\rho_{REF} V^2_{tip} S_{REF}} \tag{17}$$

$$CM^{*t} = \frac{M}{\rho_{REF} V^2_{tip} S_{REF} R} \tag{18}$$

$$CP^{*t} = \frac{P}{\rho_{REF} V^3_{tip} S_{REF}} \tag{19}$$

This non-dimensionalization has a corollary for rotorcraft, where it is referred to as an area weighted thrust coefficient [83]. Unless otherwise specified, the reader may assume that the tip velocity used in the non-dimensionalization is based on a sinusoidal approximation of the wing kinematics, given in Equation (20), based on the flapping frequency, f, peak-to-peak sweep amplitude, Φ, and wing length, R.

$$V_{tip} = (2\pi f)\,(0.5\Phi)\,R \tag{20}$$

4.2 Wing Planform

The two planforms considered for this study were the Hawkmoth wing planform based on wing geometry published by Liu [20], and an idealized rectangular wing with a 30% chord based on wing length. The surface domains used to model the left wing for each planform are shown in Figure 19. The simulations presented were computed for the same torsionally flexible configuration with the wing root and pivot location offset from the centerline by 40% of the wing length described in Section 4.3. The two planform configurations with wing motion are shown in Figure 20.

The Hawkmoth planform defined by Liu represents an approximation of the two wing pairs that overlap during the wing stroke to form a single aerodynamic surface. During the wing stroke, the two wing pairs exhibit small relative movements that influence the shape of the wing planform, the area of the combined aerodynamic surface, and the relative incidence of the two wings. Capturing the dynamic behavior into a single wing represents a best approximation of this dynamic wing structure. The Liu planform represents an approximation of a particular wing pair, which varies with time and exhibits small variations between individual Hawkmoth samples. The rectangular wing represents a simplified planform that is easily reproducible for future numerical and experimental investigations.

The time-resolved aerodynamic forces for the rectangular planform and the Hawkmoth wing planform are presented in Figure 21. The rectangular wing and the Hawkmoth wing planforms both produce force histories of a similar character, but with deviations of the peak vertical forces during each half stroke of up to 30%.

The vortical wake structures for the rectangular wing planform and the Hawkmoth wing planform are illustrated in Figure 22. Both wing planforms produce similar

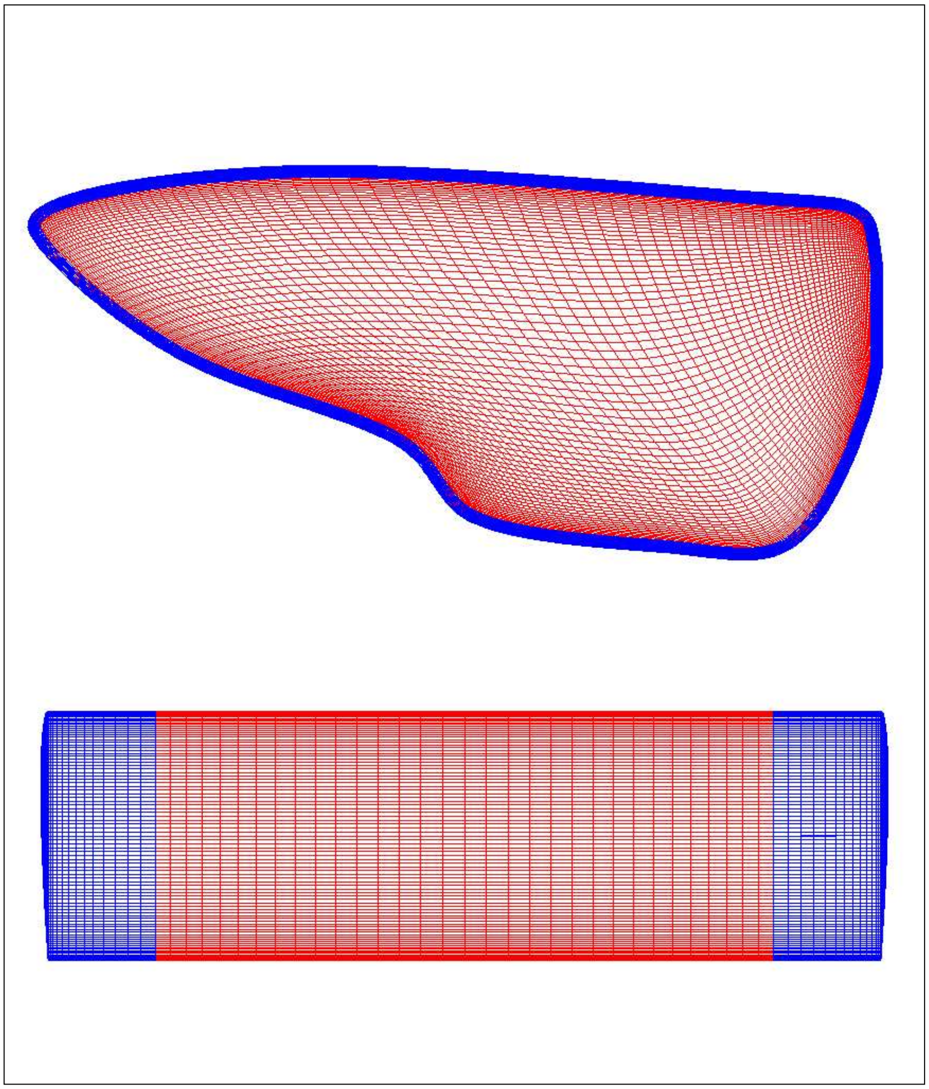

Figure 19: Comparison of Hawkmoth wing planform, upper, with the rectangular wing planform, lower. Wings correspond to the left wing when viewed from above. Each wing consists of three overset solution domains. For the Hawkmoth planform, the domains are a collar (blue), an upper skin (red), and a lower skin (not shown). For the rectangular wing, the solution domains are a main wing skin, shown in red, an outer wing cap, and an inner wing cap, each shown in blue.

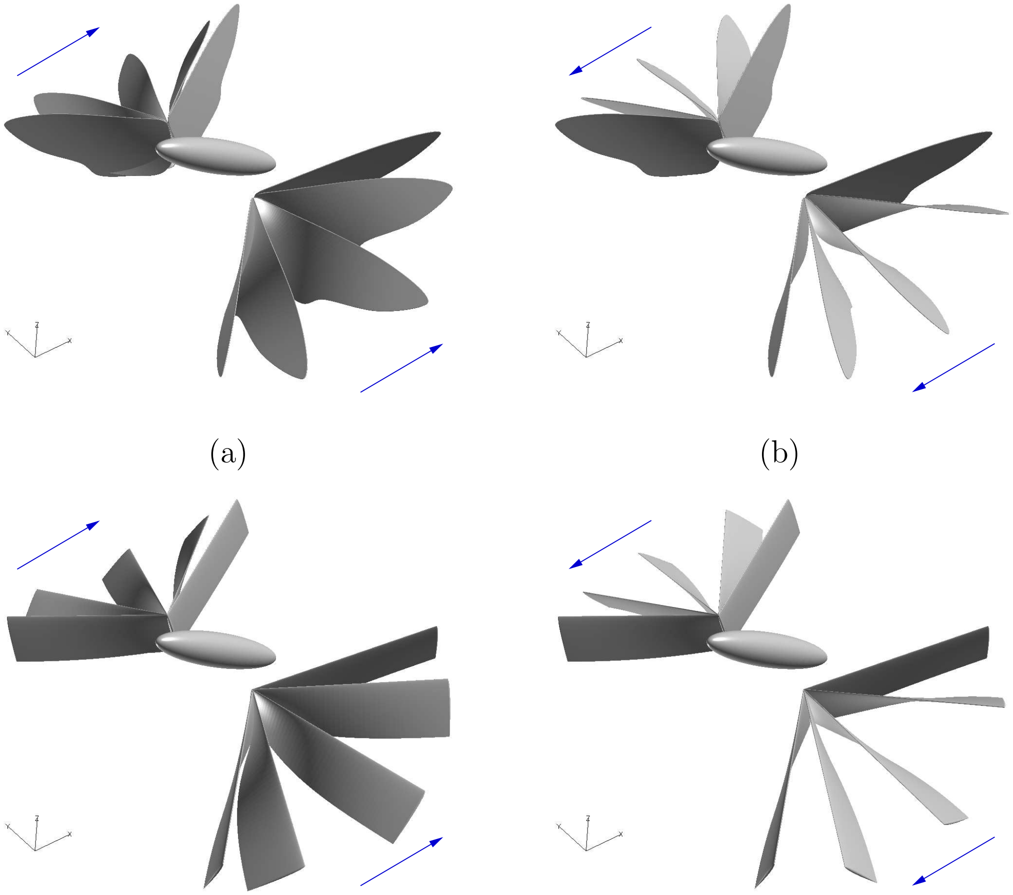

(a) (b)

(c) (d)

Figure 20: Illustration of the Hawkmoth wing planform configuration, (a) and (b), and the rectangular wing planform configuration, (c) and (d). The direction of the wing motion is indicated using blue arrows. Wing motions represent the 4-term kinematic approximation with prescribed feathering along the wing length.

overall wake structures, reproducing the character of the unsteady Hawkmoth wake. However there are local small variations in the magnitude and the strength of the wake structures produced by the two planforms.

4.3 Wing-Body Interactions

The Hawkmoth wing is a flexible structure that is joined to the body with a compliant membrane at the wing root. It is not possible to model this flexible membrane and preserve the observed wing-body interactions when using a rigid wing simulation. The ability to examine the performance of a rigid wing necessitated that the wing root be offset from the body in order to resolve the motion of the wing root while preventing contact between the wing surface and the body surface.

To understand the influence of wing-body interactions on the unsteady aerodynamic mechanisms, simulations were computed with and without an idealized Hawkmoth body. The Hawkmoth body was represented using an elliptical body with a circular cross section. The body length was 80% of the wing length and the body diameter was 10% of the wing length. The simulations presented were computed for torsionally flexible wings with the wing root and pivot location offset from the centerline by 40% of the wing length. The 40% centerline offset was the minimum offset that allowed full kinematic motion of the rigid Hawkmoth wing while maintaining the grid spacing requirements in the regions where the wing and body solution domains overlapped in physical space. For wing offsets less than 40%, the wing root trailing edge of the rigid Hawkmoth wing would pierce the body surface at pronation and supination, which correspond to the maximum wing stroke angles. Smaller wing offsets may be achieved for alternative wing planforms or for flexible wings, depending on the specific planform or set of wing deformations. The solution domains used to compute the flexible rectangular wing-body configuration are illustrated in Figure 23. The solution configuration for the wing-only simulations utilized the same near-body and off-body solution domains with the exception of the body domain.

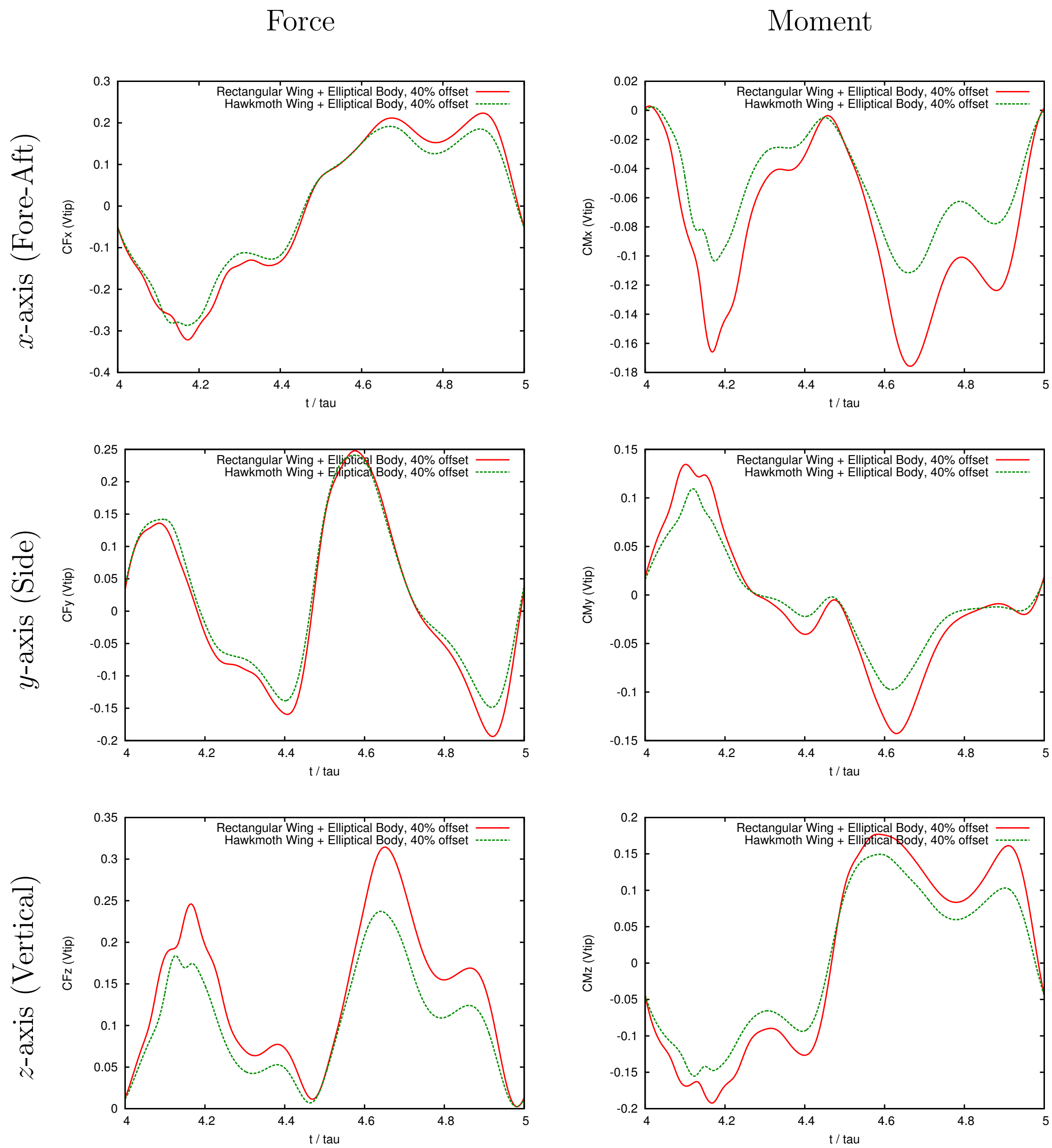

Figure 21: Comparison of the rectangular wing solution with elliptical body to the Hawkmoth planform simulations with elliptical body. Simulations are based on a 4-term kinematic approximation with prescribed feathering along the wing length.

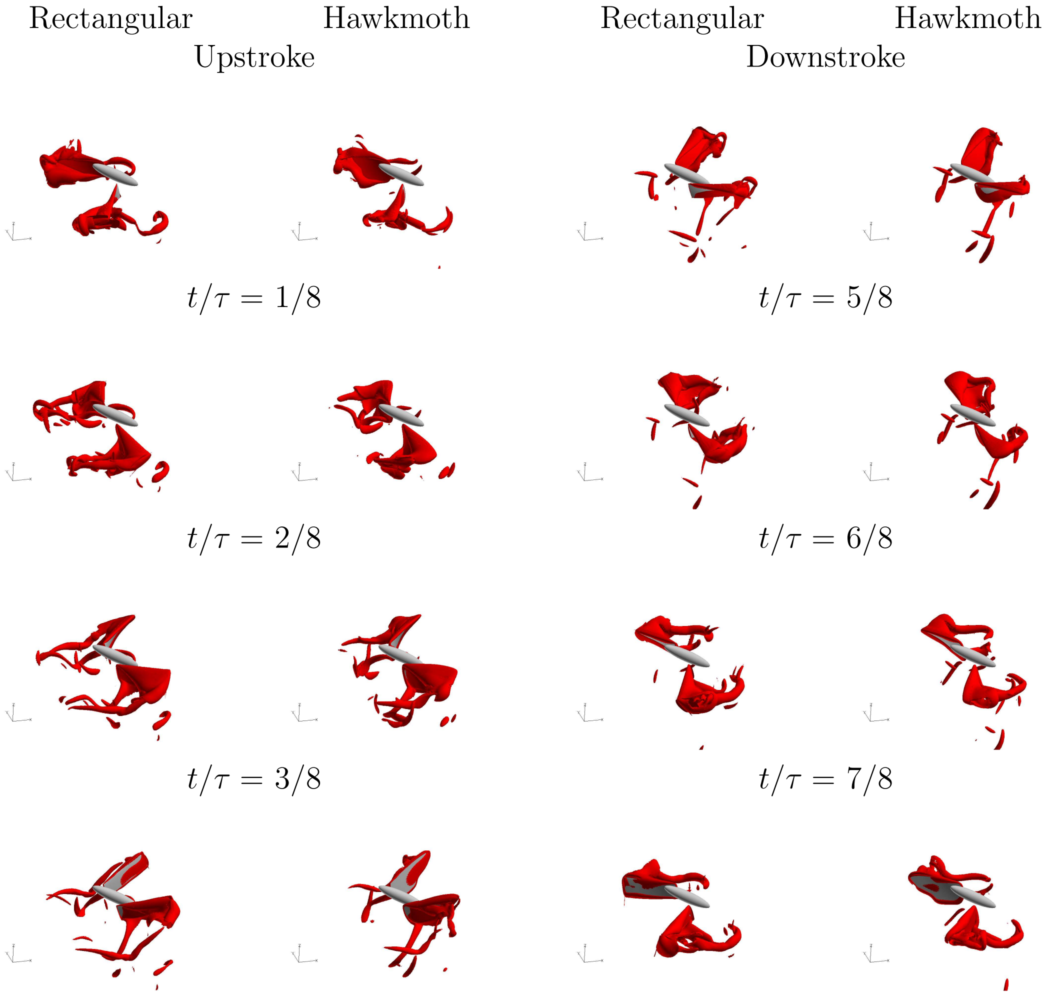

$t/\tau = 1/8$ $t/\tau = 5/8$

$t/\tau = 2/8$ $t/\tau = 6/8$

$t/\tau = 3/8$ $t/\tau = 7/8$

$t/\tau = 4/8$ $t/\tau = 8/8$

Figure 22: Comparison of the wake structures of the rectangular wing planform to the Hawkmoth wing planform. Simulations are based on a 4-term kinematic approximation with prescribed feathering along the wing length. Wake structures are iso-surface of vorticity magnitude.

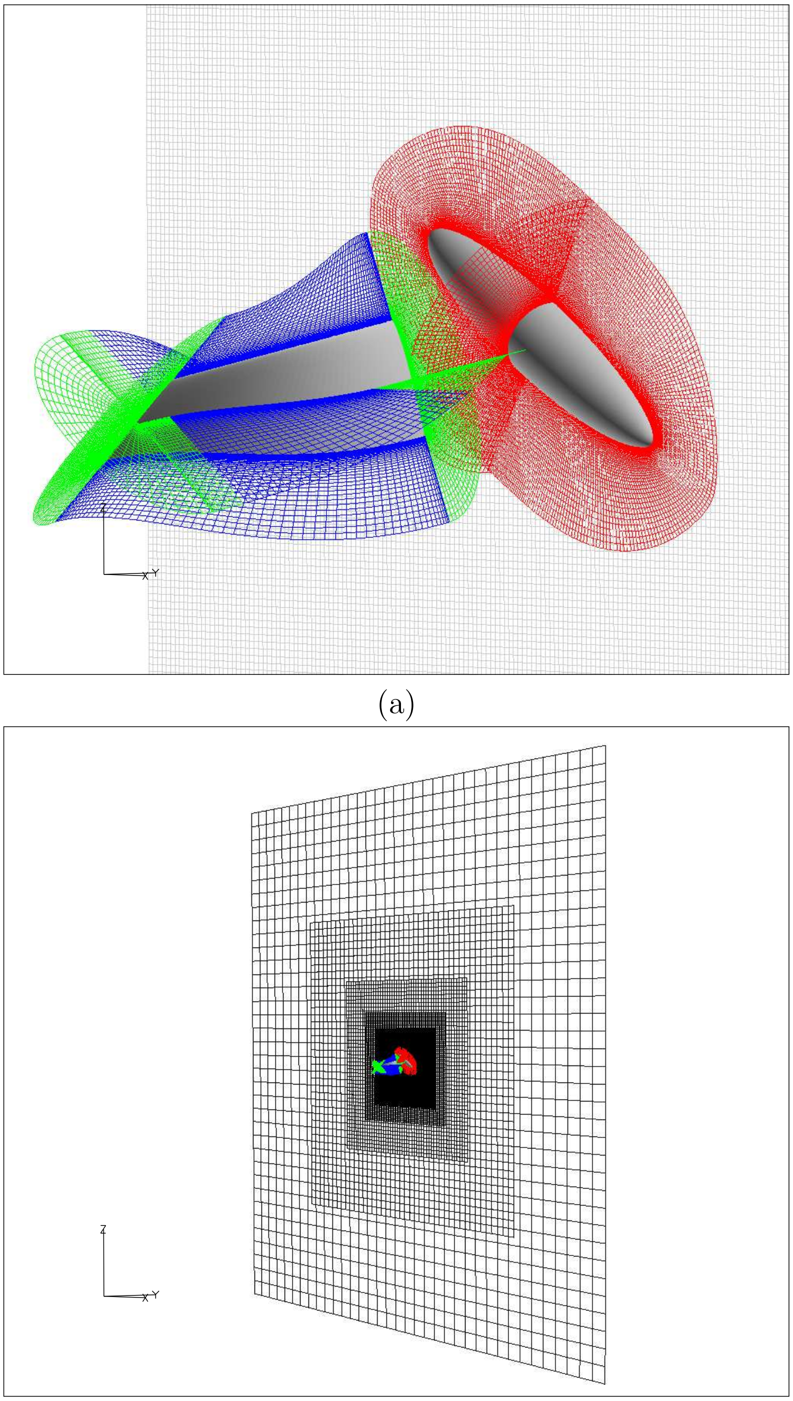

(a)

(b)

Figure 23: Near-body solution domains (a) and off-body solution domains (b) for the flexible wing-body configuration at $t/\tau = 0.25$. The solution domains representing the wing are colored in blue and green while the solution domain representing the elliptical body is colored in red. In (a), the first off-body domain is represented in grey, while the set of off body domains are represented in black in (b).

The computed aerodynamic forces for the two rectangular wing simulations, with and without the elliptical body, are shown in Figure 24. The force histories are almost identical, indicating that the body does not significantly impact the aerodynamic mechanisms generated by the wing motions for simulations with the large wing-body gap. The wake structures produced by the two configurations show minimal variation between the wing-body and the wing only simulations, shown in Figure 25.

4.4 Influence of Wing Length

To understand the influence of wing length on the unsteady aerodynamic mechanisms, flow solutions were computed for three wing lengths utilizing identical wing kinematics. Solutions were computed for dimensional wing lengths of 30, 50, and 80 mm, with a constant aspect ratio. It was observed that the magnitude of the dimensional forces and moments produced by the three wing lengths, shown in Figure 26, scaled with the square of the tip velocity, V_{tip}^2. When the forces and moments are non-dimensionalized based on the tip velocity, using Equations (17) and (18), the non-dimensional force histories reduce to similar time histories of same order of magnitude, as shown in Figure 27. The non-dimensional force histories do show small variations in the peak lift amplitude. It is possible that the force variations are due to variations in the Reynolds numbers used for each simulation. The Reynolds number used for the three simulations was held constant, and not updated for the change in tip velocity due to the change in wing length. That the time resolved aerodynamic forces produced by wings of different lengths may be non-dimensionalized by tip velocity is significant in that it removes wing length from the design space to be considered when examining the influence of kinematic variations and structural response on aerodynamic performance.

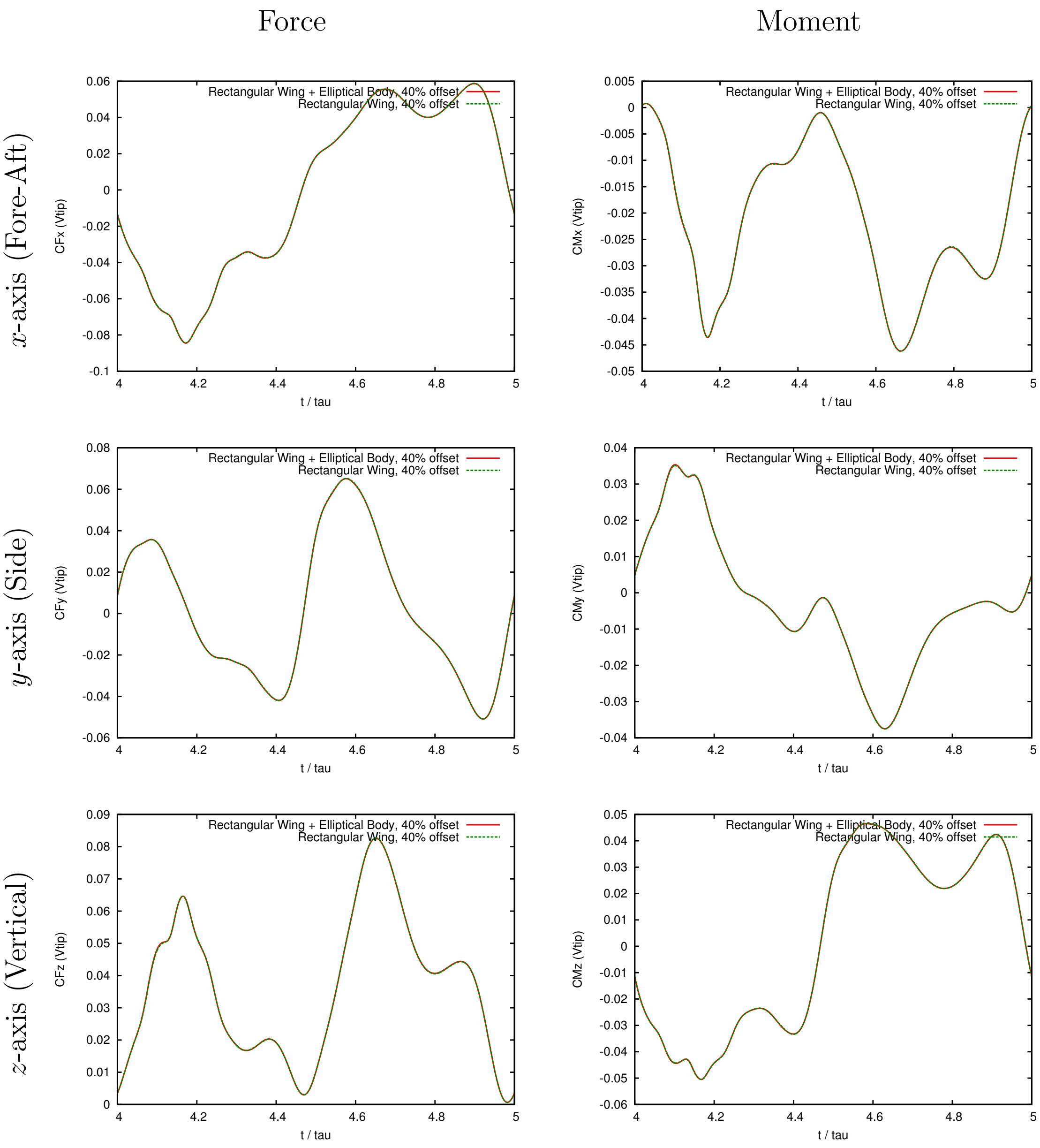

Figure 24: Comparison of the wing-body solution to the wing-only solution for the rectangular planform. Simulations are based on a 4-term kinematic approximation with prescribed feathering along the wing length. The time-resolved aerodynamic force coefficients are not significantly influenced by the presence of the elliptical body.

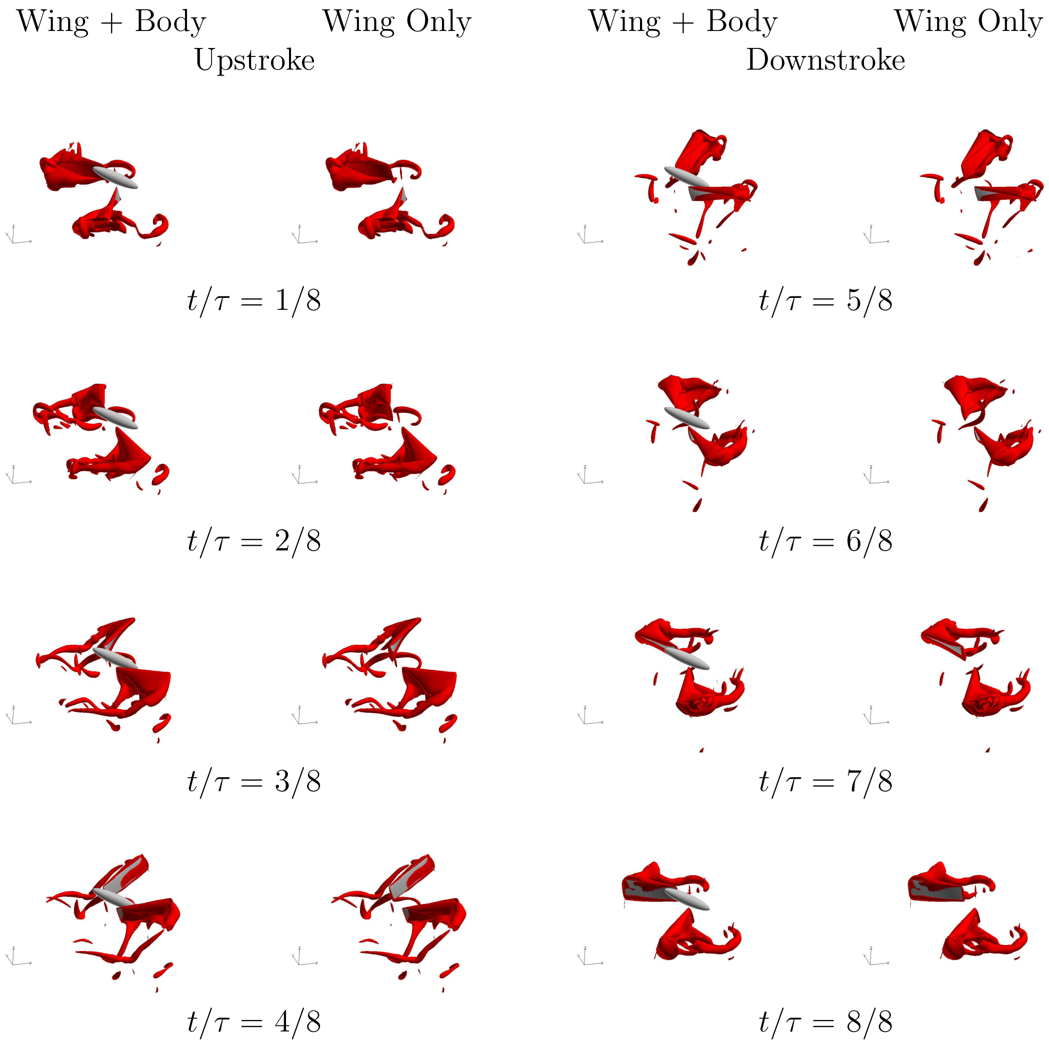

Figure 25: Comparison of the wake structures of the rectangular wing solution with and without the elliptical body. Simulations are based on a 4-term kinematic approximation with prescribed feathering along the wing length. Wake structures are iso-surface of vorticity magnitude.

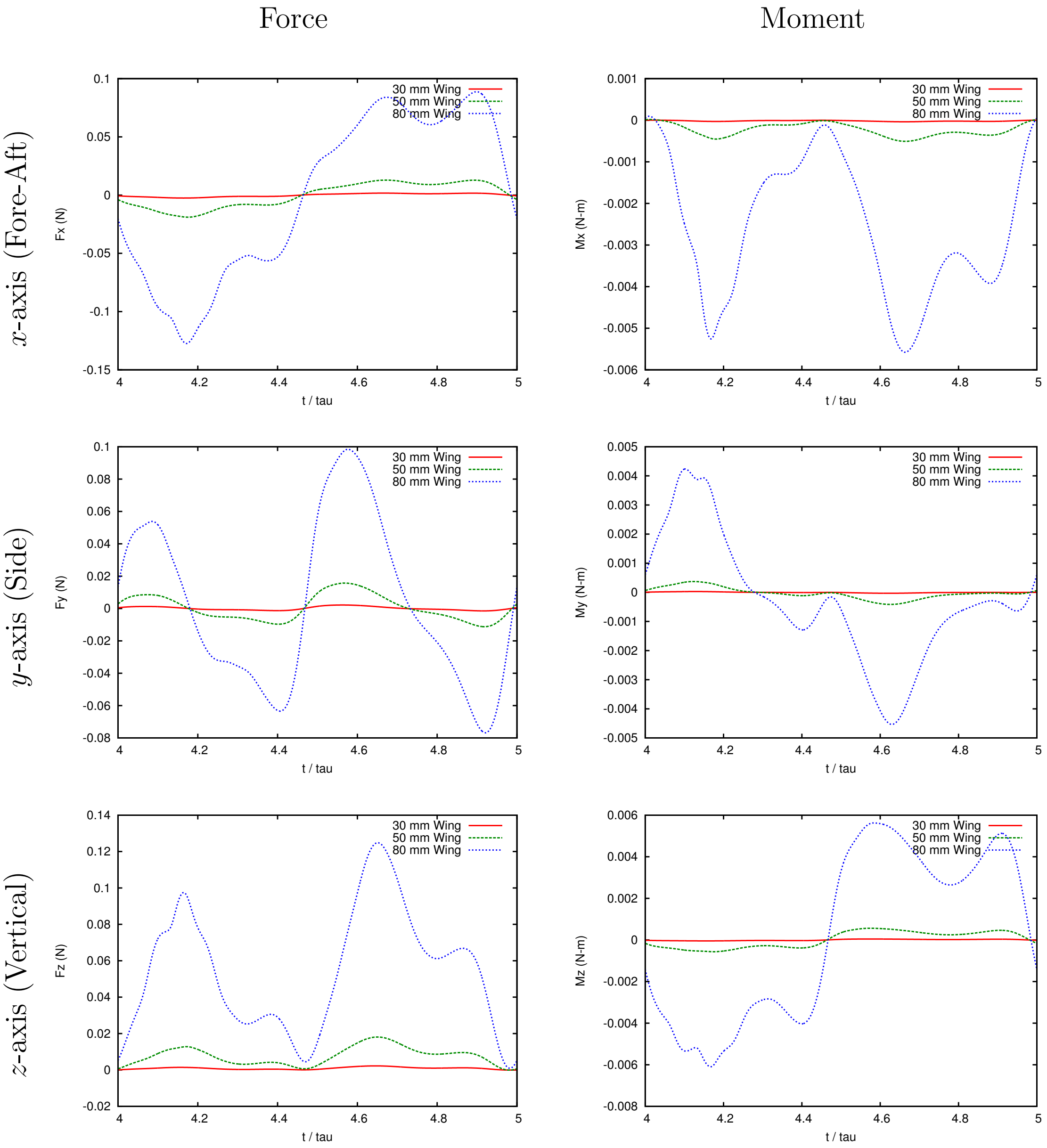

Figure 26: Comparison of the dimensional forces computed for the 30 mm, 50 mm, and 80 mm rectangular wings with prescribed torsion.

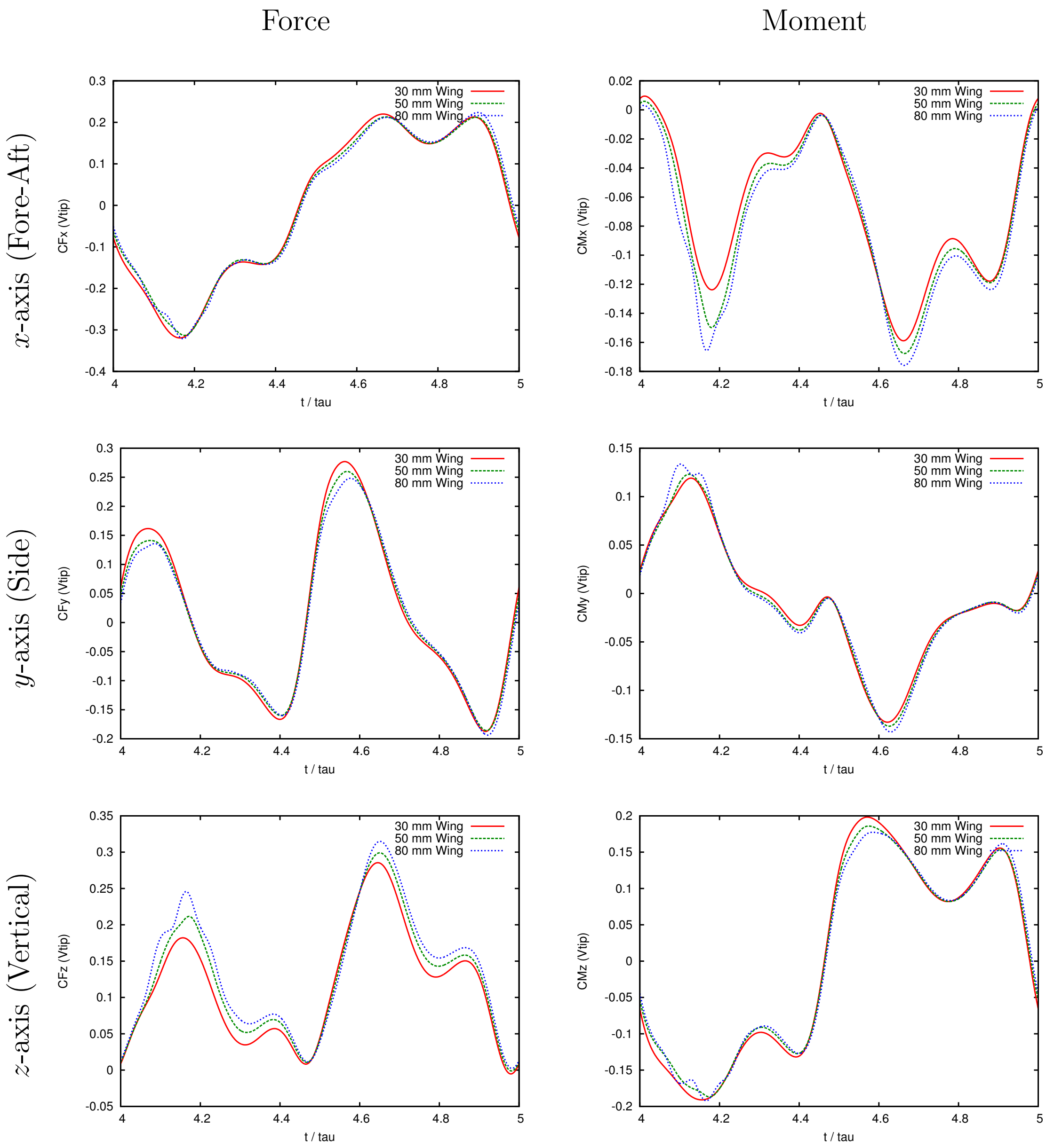

Figure 27: Comparison of the force coefficients based on tip velocity computed for the 30 mm, 50 mm, and 80 mm rectangular wings with prescribed torsion.

4.5 Summary

The aerodynamic forces, moments, and power requirements non-dimensionalized based on the approximate peak tip velocity provide a set of performance metrics that may be used to compare solutions for varying configurations.

Of the geometric parameters considered, wing-body interaction, wing planform, and wing length, wing planform had the most significant influence on the unsteady aerodynamic mechanisms. The influence of wing-body interaction was minimal for the size of the gap necessary to resolve the rigid wing motion without contacting the body surface. It was shown that the influence of wing length on the aerodynamic performance could be accounted for by non-dimensionalizing the aerodynamic forces by the square of the peak of the wing tip velocity.

The influence of the wing planform could be seen in the time-resolved aerodynamic forces and vortical wake structures produced during the wing stroke. Unfortunately, the Hawkmoth planform used in this study is a rough approximation of an actual Hawkmoth wing, and does not provide a good representation of the wing-body junction. Realizing that the Hawkmoth planform was a rough approximation of an actual Hawkmoth wing and that the rectangular wing planform captures the relevant unsteady aerodynamic mechanisms exhibited by the Hawkmoth in flight, the baseline configuration used for the remainder of the study is based on a symmetry solution with a single rectangular wing planform and no body, as described in Section 3.3.

V. Analysis of Kinematic Variations

Due to the correlation between the unsteady aerodynamic phenomena and the dynamic wing motion, variations in the dynamic wing motions have a direct influence on the unsteady aerodynamic mechanisms and aerodynamic performance [2, 3, 4, 5, 6, 7]. Thus, it is important to have a basic understanding of the influence of the kinematic profile on the unsteady aerodynamic phenomena before examining the influence of structural response on aerodynamic performance.

The motion of a rigid flapping wing may be defined using a set of time-dependent translations and rotations about the wing root using any of the standard engineering notations. There are, however, alternative notations that describe the wing motion based on the physiology of a given flier, often referred to in literature as kinematic parameters. The choice of kinematic parameters used to describe the wing motion of a given organism may be based on skeletal, musculature, or other physiological constraints of the organism, or they may be defined for convenience in the collection of experimental data.

5.1 The Kinematic Parameters

The kinematic parameters used for this study to define the rigid wing motion are based on the experimental work of Willmott and Ellington [84, 17, 6]. Willmott and Ellington documented the time-dependent motion of the Hawkmoth wing using four kinematic rotations. The four kinematic parameters that define the wing orientation in a global reference frame are sweep, $\phi(t)$, elevation, $\theta(t)$, feathering, $\alpha(t)$, and stroke-plane inclination, β, as shown in Figure 28. The stroke-plane passes through the wing root and is inclined with respect to the freestream orientation. The stroke-plane represents a reference plane that captures the dominant sweep rotation, as shown in Figure 29. The sweep angle, $\phi(t)$, represents the angle of the wing axis, or feathering axis, projected onto the stroke-plane. Wing sweep is often referred to as the in-plane rotation. The elevation angle, $\theta(t)$, represents the deviation from the stroke-plane, or the angle measured between the feathering axis and its projection onto the stroke-plane. The elevation angle is also known as the out-of-plane rotation. Together, the sweep and elevation angle define the three-dimensional motion of the wing tip. The feathering angle, $\alpha(t)$, represents the rotation about the feathering axis. The feathering axis corresponds to the leading edge of the wing for the rectangular wing simulations, and a line from the wing root to the wing tip for simulations using the Hawkmoth planform. A fifth angle, χ, defines the orientation of the body with respect to the freestream direction in the inertial reference frame. Body orientation as defined does not directly influence the dynamic wing motion, but it does influence the geometric configuration and wing-body relationship. For this analysis, sweep, elevation, and feathering angles vary as a function of time, while stroke-plane inclination and body angle are constants. Together, these five parameters describe the orientation of the body and the rigid body motion of the wing in the inertial reference as a function of time.

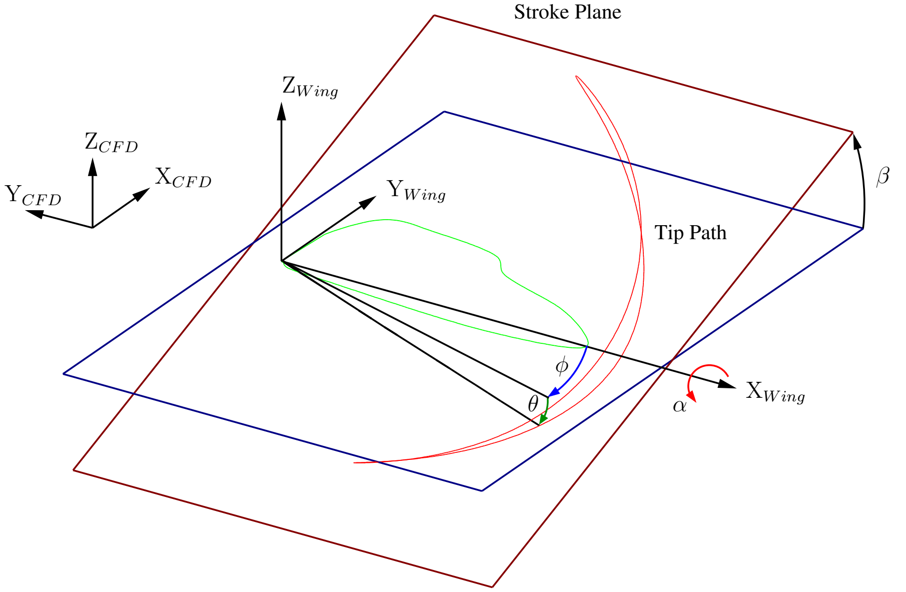

Figure 28: Hawkmoth kinematic parameters defined by Willmott and Ellington [17]. The sweep angle, $\phi(t)$, represents the orientation of the wing projected onto the stroke-plane. The elevation angle, $\theta(t)$, represents the angle of the wing measured between the feathering axis and the stroke-plane, and the feathering angle, $\alpha(t)$, represents the rotation about the feathering axis.

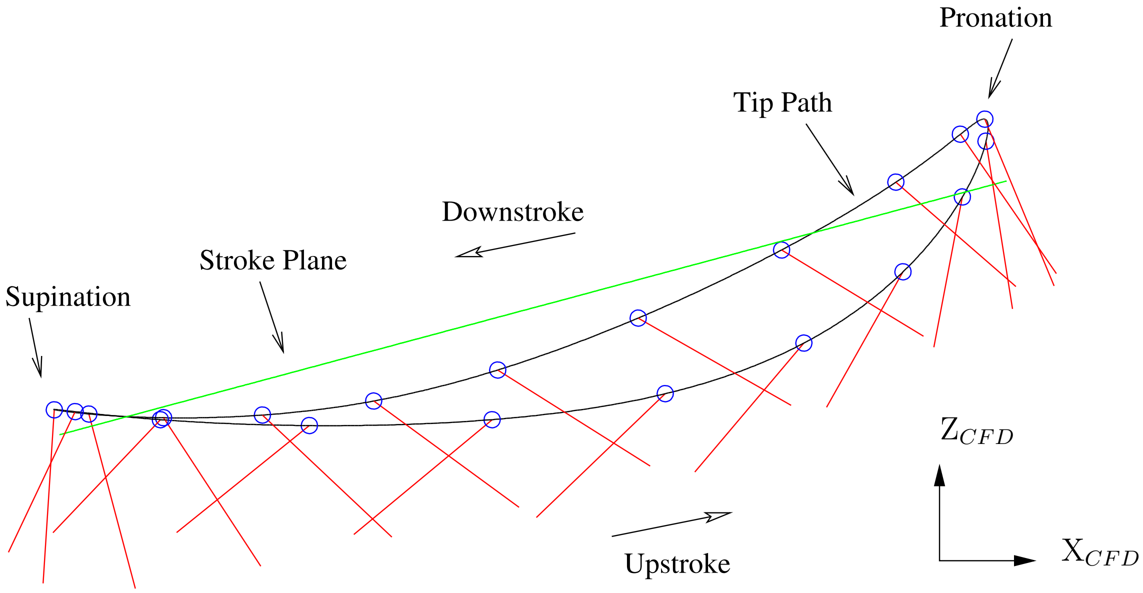

Figure 29: The leading edge tip path of the left wing, shown in black, with respect to the stroke-plane, shown in green. The wing orientation during the stroke cycle is shown in red with blue circles indicating the leading edge.

5.1.1 Phases of Motion. When examining the influence of the kinematic profile, it is convenient to decompose the wing motion into phases based on the type of motion. The wing motion during the flapping cycle is composed of two dominant types of motion: a wing sweep in which the wing moves "up" or "down", and a feathering rotation about the longitudinal, or span-wise, wing axis. The use of "up" and "down" to define the direction of wing motion is often misleading, as "up" in this case refers to the upstroke based on the Hawkmoth morphology. The direction of the upstroke in the inertial reference frame depends on the inclination of the stroke-plane, which is only 15 degrees from freestream direction for the Hawkmoth at hover, as shown in Figure 29. The wing sweep is characterized by large tip velocities as the wing sweeps through 111 degrees. The wing sweep, or "translational motion", and the feathering, or rotational motion, are not separated in time; rather they overlap at the end of one half-stroke and the beginning of the following half-stroke as shown in Figure 30. For the Hawkmoth, the wing feathers through 120 degrees at the end of each sweep cycle such that the same edge of the wing leads during both the up- and downstrokes. With a flapping frequency of 26 Hz, the wing motion is dominated by large rotational rates and accelerations during each flapping cycle.

5.1.2 Kinematic Parameters to Rigid Wing Motion. In order to utilize the kinematic parameters to prescribe the wing motion for the numerical simulations, a direction cosine matrix was computed by applying the kinematic parameters in the following order:

1. Apply the feathering rotation, α, about wing-local x-axis
2. Apply the elevation rotation, θ, about body-fixed y-axis
3. Apply the sweep rotation, ϕ, about body-fixed z-axis
4. Apply the stroke-plane inclination rotation , β, about body-fixed x-axis

The direction cosine matrix may then be used to transform the wing from an initial location to the time-dependent orientation, or the direction cosine matrix may be used to compute the quaternions utilized by OVERFLOW 2.1-Elastic to define wing orientation as a function of time. This approach was used to compute the wing orientation throughout the wing stroke cycle illustrated in Figure 30 (a) for the kinematic parameters in Figure 30 (b).

5.2 Influence of the Kinematic Approximations on Aerodynamic Force Production

In order to remove discontinuities in the experimentally determined kinematic parameters and interpolate those parameters at a time resolution suitable for numerical simulation, a truncated Fourier series, as defined in Equation (21), was utilized to approximate each of the three time-dependent kinematic parameters given in Equations (22), (23), and (24).

$$\phi(t) = \frac{\phi_{c0}}{2} + \sum_{n=1}^{\infty} \left(\phi_{cn} \cos\left(\omega n t\right) + \phi_{sn} \sin\left(\omega n t\right)\right) \tag{21}$$

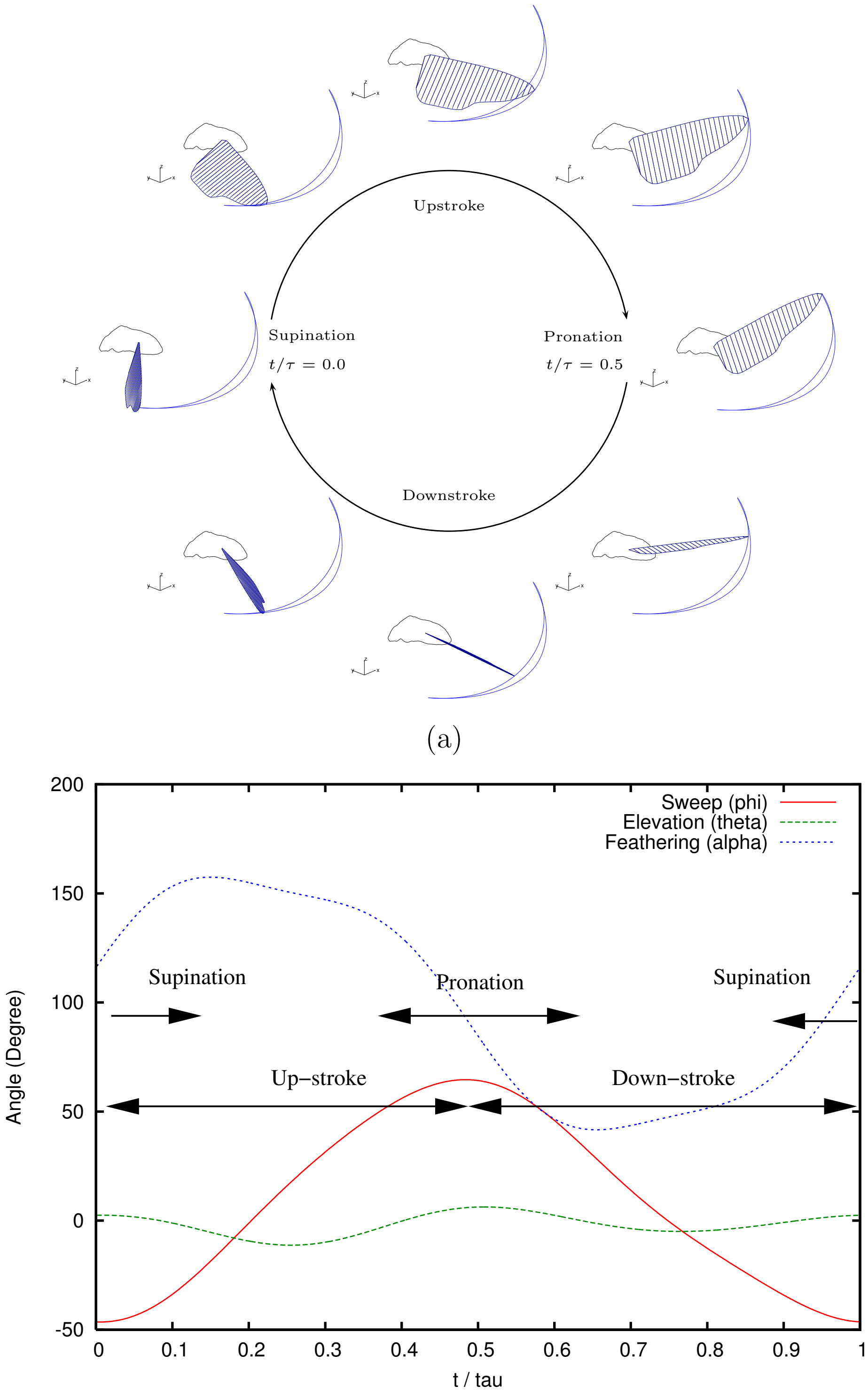

(a)

(b)

Figure 30: Rigid wing motion in the inertial reference frame (a) for the Hawkmoth hover kinematics used by Liu [19,20] and Aono [24] (b). The outline of the Hawkmoth body is included for orientation.

Both Liu and Aono utilized a four-term Fourier approximation to smooth the experimental kinematic data measured by Willmott and Ellington. However, the influence of the truncated Fourier approximation on the aerodynamic performance of the resulting numerical simulations was not addressed in the available literature.

$$\phi(t) = \frac{\phi_{c0}}{2} + \sum_{n=1}^{3} \left(\phi_{cn} \cos\left(\omega n t\right) + \phi_{sn} \sin\left(\omega n t\right)\right) \tag{22}$$

$$\theta(t) = \frac{\theta_{c0}}{2} + \sum_{n=1}^{3} \left(\theta_{cn} \cos\left(\omega n t\right) + \theta_{sn} \sin\left(\omega n t\right)\right) \tag{23}$$

$$\alpha(t) = \frac{\alpha_{c0}}{2} + \sum_{n=1}^{3} \left(\alpha_{cn} \cos\left(\omega n t\right) + \alpha_{sn} \sin\left(\omega n t\right)\right) \tag{24}$$

Prior investigations examining the influence of kinematic variations on rigid wing performance by Bos [85, 86, 87, 88] indicate that wing kinematics that mimic the observed kinematics of insects in flight produce greater lift-to-drag ratios than simplified or harmonic kinematic approximations. This has a direct influence on aerodynamic power requirements. Other investigations examining the influence of wing kinematics [89, 90, 91, 7, 2, 3, 4, 5, 6] support similar conclusions that simplified wing kinematics are often unable to recreate the aerodynamic performance of natural flapping wing fliers. Thus, it is important to understand the influence of the kinematic approximation on aerodynamic performance prior to examining the influence of structural flexibility on aerodynamic performance.

A full sensitivity study examining the influence of kinematic variation is outside the scope of the current research. However, by varying the number of terms used in the Fourier approximation of the kinematic parameters, the sensitivity of the aerodynamic mechanisms and aerodynamic performance to the Fourier approximation may be examined, and by extension, lead to a greater understanding of the role of the kinematic parameters and kinematic rates in determining aerodynamic performance.

5.2.1 The Fourier Approximation of the Kinematic Parameters. To assess the influence of the kinematic approximation on aerodynamic performance, simulations were computed for hover wing kinematics published by Aono [24] approximated using 2-, 3-, and 4-term Fourier series. The 4-term Fourier series represents a complete reconstruction of the kinematic parameters used by Liu and Aono, as their kinematic parameters were based on a 4-term approximation of the experimentally measured kinematic parameters of Willmott and Ellington [17,6]. The approximated kinematic parameters and kinematic rates for the 2-, 3-, and 4-term Fourier approximations are shown in Figure 31 along with the digitized points representing the 4-term kinematic profile used by Aono.

Comparing the 2-term Fourier approximation, or harmonic approximation, of the kinematic parameters in Figure 31 to the digitized 4-term approximation, the 2-term approximation captures the amplitude of the flapping and feathering rotations but does not capture the out-of-plane rotation. The 2-term kinematic approximation also preserves the phase relationship between the sweep and feathering parameters, but does not capture the phase relationship between the peak sweep and feathering rates. It is not until all four terms are included in the Fourier approximation that the phase relationship between the peak sweep and feathering rates used by Aono are captured.

Because the 2-term approximation represents a harmonic approximation of the kinematic parameters, it is not able to capture the shortened duration of the upstroke compared to the downstroke, nor does it capture the squared-off shape of the feathering curve. Compared to the 2-term approximation, the 3-term approximation captures a bias in the duration of the upstroke to downstroke, and provides a slightly better capture of the sweep rate. The 3-term approximation also captures the out-of-plane rotation as well as the elevation rate. However, the 3-term approximation still does not capture the squared off shape of the feathering parameter or the complex shape of the feathering rate. The 4-term approximation provides a complete reconstruction of the kinematic parameters as used by Liu and Aono. Compared to the 2- and

3-term Fourier approximations, the 4-term approximation exhibits a complex phase relationship between the sweep, elevation, and feathering rates which influences the tip velocity of the wing and the duration of the feathering rotation during pronation and supination.

5.2.2 Influence of Kinematic Variations on Aerodynamic Performance. The rigid wing simulations based on the 2-, 3-, and 4-term Fourier approximations of the wing kinematics each produce distinct aerodynamic force histories, shown in Figure 32. The 2- and 3-term rigid wing solutions both produce force histories with a single peak in the force magnitude late in each half-stroke, while the 4-term rigid wing solution produces a force history with two peaks per half-stroke. Though the rigid wing solutions for the 2- and 3-term kinematic profiles both produce a single peak in the aerodynamic force magnitude, the amplitude and history of the directional forces are unique to each kinematic profile. For example, the 2-term rigid wing solution is the only solution presented that generates a negative, or downwards vertical force at any point in the flapping cycle. Yet, the 2-term kinematic profile also generates peak vertical forces that are almost twice the amplitude of the vertical forces generated by the 3-term kinematic profile.

To understand why the three kinematic approximations produce the distinct force histories, the relationship between the aerodynamic forces and the kinematic parameters was examined by plotting the aerodynamic forces against the time-dependent kinematic parameters, kinematic rates, and kinematic accelerations, as shown in Figures 33, 34, and 35. These phase plots highlight correlations between the kinematic parameters and the aerodynamic forces.

Examining the phase plots, the relationship between the peak aerodynamic force magnitude and the sweep and elevation rates stand out in Figure 34. Based on an understanding of unsteady aerodynamic mechanisms and delayed stall, it is a logical assumption that the wing should produce peak aerodynamic force during the translation phase when the wing reaches peak translational velocity at a moderate angle

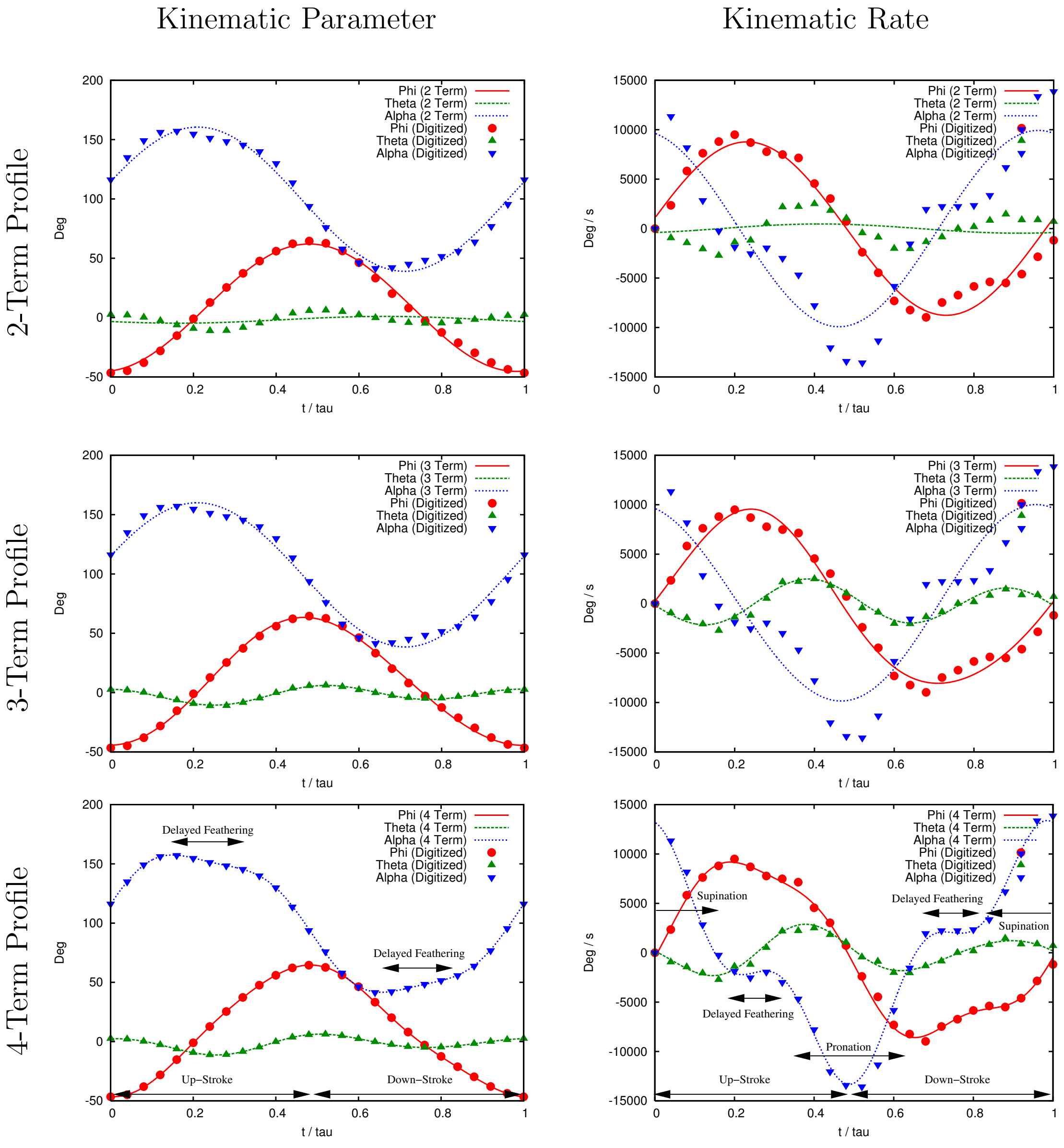

Figure 31: Smoothed kinematic parameters and kinematic rates based on 2-term, 3-term, and 4-term Fourier approximations of the published Aono kinematic parameters [24]. The digitized Aono parameters were based on a 4-term Fouier approximation of the Willmott and Ellington parameters [17].

of attack. Examining the phase relationship between aerodynamic force magnitude and the sweep rate for the 2-, 3-, and 4-term kinematic profiles shown in Figure 34, the correlation between peak force magnitude and sweep rate was strongest for the 4-term kinematic profile, while the peak aerodynamic force magnitude lagged behind the peak sweep rate for the 2- and 3-term kinematic profiles. In Figure 34, the kinematic rates are plotted along the horizontal axis and the force magnitude is plotted on the vertical axis. When the peak aerodynamic force magnitude occurs in phase with a peak kinematic rate, the plot of the force history forms a sharp peak, as exhibited by the 4-term profile. When the peak kinematic rate precedes the peak force magnitude, the force plot forms an open loop as exhibited by the 3-term kinematic profile.

The 3- and 4-term kinematic profiles both exhibited strong correlations between peak aerodynamic forces and peak elevation rate, while the 2-term profile exhibited a very different relationship with the elevation rate. During the translational phase of the wing stroke, wing velocity is only one component that influences the bound circulation about the wing. Feathering orientation, along with the wing velocity, determines the geometric angle of attack. Examining the relationship between the force magnitude and the feathering orientation in Figure 33 shows that the peak force production and maximum feathering orientation occur in phase for the 4-term kinematic profile, while the peak force magnitude lags behind the peak feathering orientation for the 2- and 3-term kinematic profiles.

It is possible that the phase lag between the peak force magnitude and the 2- and 3-term sweep and elevation rates and the feathering orientation are due to phase variations between the kinematic parameters within a given profile. It is also possible that the phase variation between the forces and the parameters are due to the influence of unsteady aerodynamic mechanisms that may not be represented as functions of the kinematic parameters alone. Such aerodynamic mechanisms include the influence of interactions between the wing and previously shed wake structures, and the influence of local variations in the aerodynamic mechanism along the wing span.

The 4-term kinematic profile exhibits a second peak in the force history as the sweep rate is decreasing and the wing starts the rotational phase of motion characterized by the large feathering rotation at the end of the half-stroke. The 4-term kinematic profile differers significantly from the 2- and 3-term kinematic profiles in the shape of the feathering parameter and the magnitude and timing of the feathering rates and accelerations. The shape of the 2- and 3-term feathering parameters is nearly sinusoidal, while the 4-term feathering parameter exhibits a delayed feathering rotation, or a squared off feathering profile. The delay corresponds to a reduced duration of the 4-term feathering rotation, leading to increased feathering rates and accelerations. This variation is significant because the second peak in the force history associated with the 4-term kinematic profile corresponds to the second peak in the feathering acceleration during each half-stroke, as shown in Figure 35. The influence of the feathering acceleration on the aerodynamic mechanisms is examined in the next chapter.

Why the force history produced by the 4-term kinematic profile exhibits the two peaks during each half stroke is not yet fully clear. Examining the phase plots, the first aerodynamic peak corresponds to peak translational velocities and feathering orientation during the translational phase of wing motion, and the second aerodynamic peak corresponds to peak feathering acceleration as the wing enters the rotational phase of motion. Yet, it is not clear what causes the dramatic drop in the force magnitude between the peak translational velocity and the peak feathering acceleration. This phenomenon may also be observed in simulations previously computed by Aono [24,25] for his examination of the wake of a hovering Hawkmoth. The influence of the sharp decline in force magnitude may be seen as a dramatic drop at a constant feathering rate in Figure 34, and as dips near the peak elevation accelerations in Figure 35. Understanding this interaction and identifying a cause and effect relationship would benefit from further study of the influence of the kinematic parameters based on a systematic variation of the kinematic parameters.

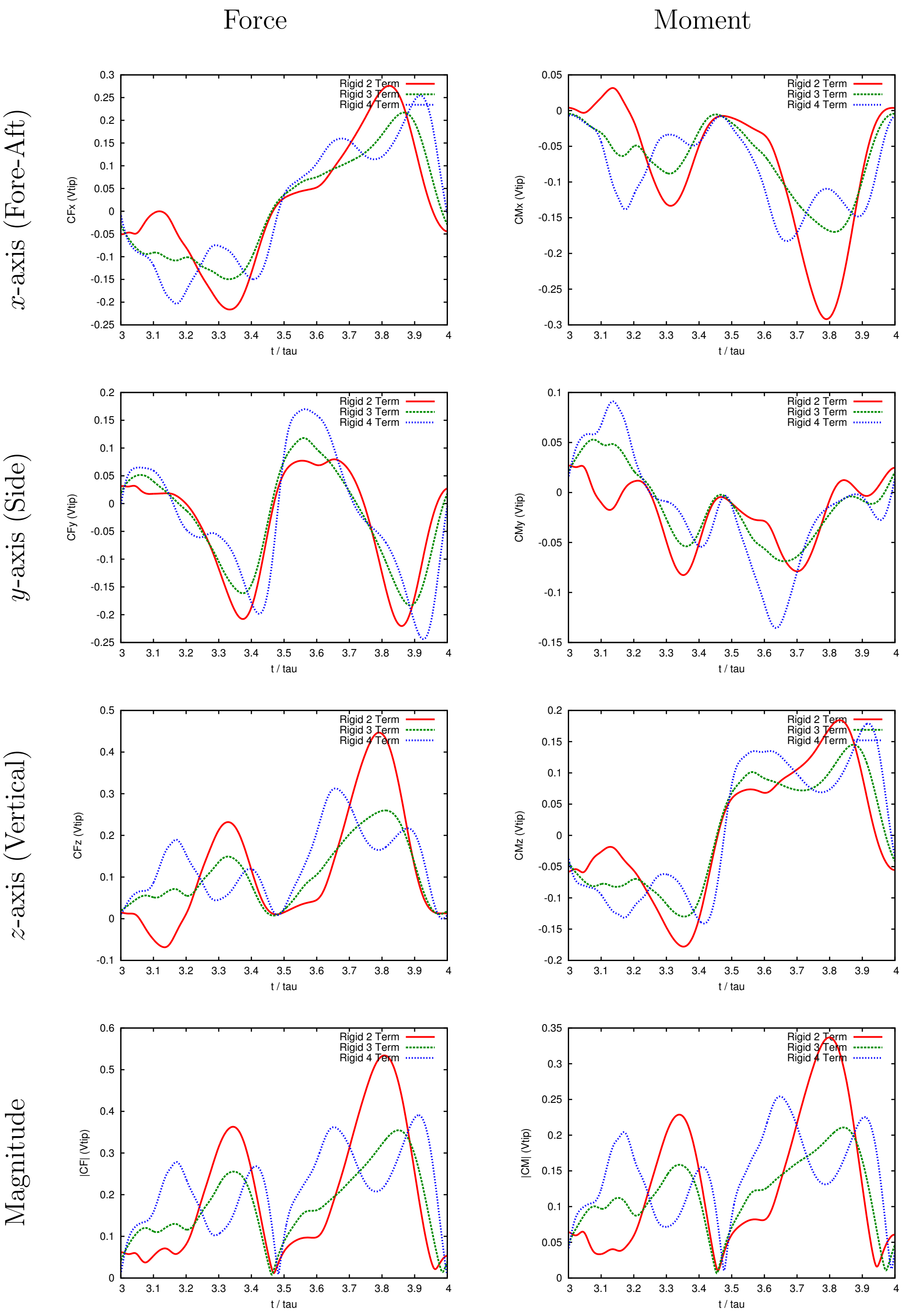

Figure 32: Aerodynamic force and moment histories for the third flapping cycle of the rigid wing solutions based on the 2-, 3-, and 4-term Fourier kinematic profiles. The flier is oriented in a reference system with the x-axis aligned in the aft direction, the z-axis aligned in the vertical direction, and the y-axis aligned with the right wing.

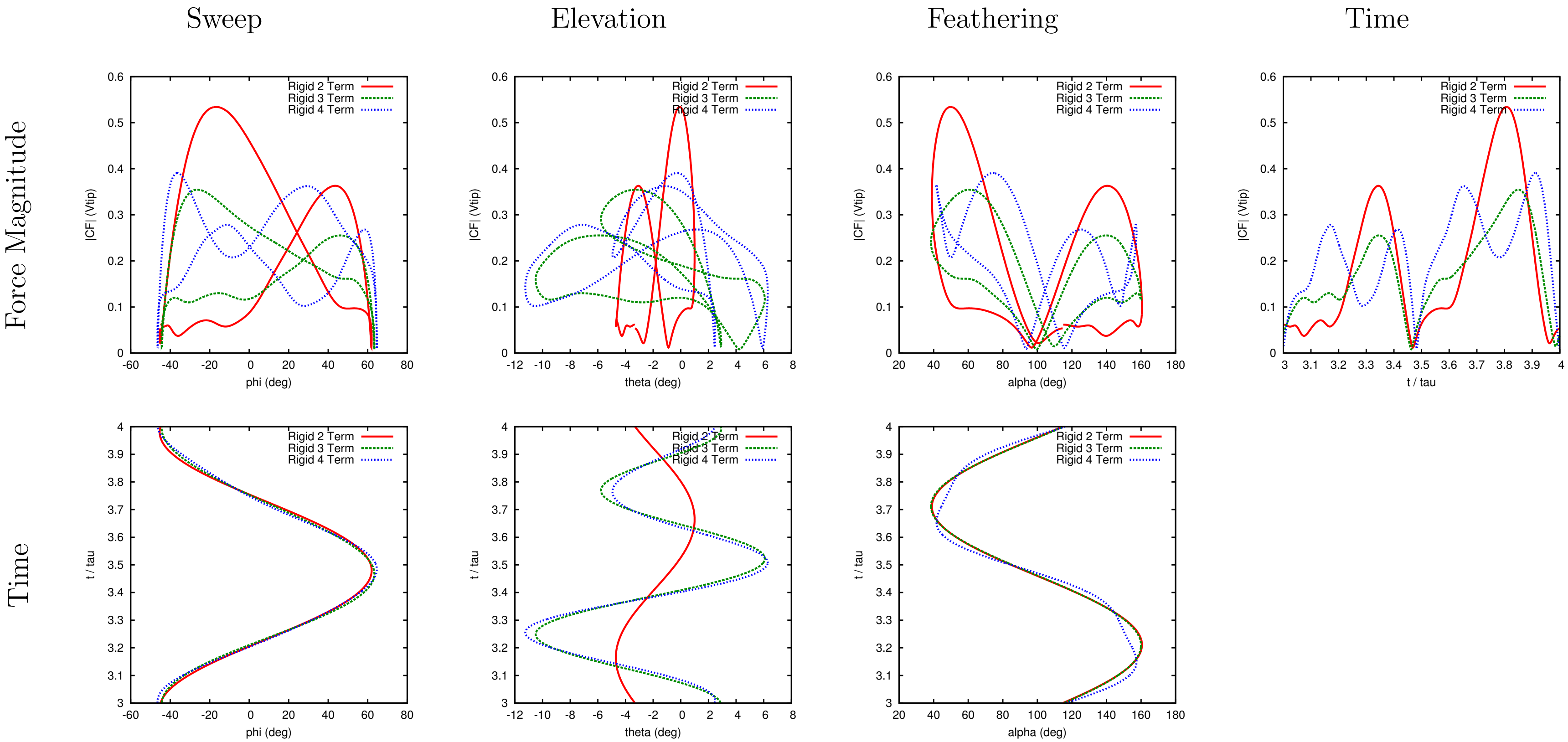

Figure 33: Plotting aerodynamic forces against the time-dependent kinematic parameters for the 2-, 3-, and 4-term Fourier approximations highlight the sensitivity of the aerodynamic forces to the kinematic parameters. Rigid wing solution.

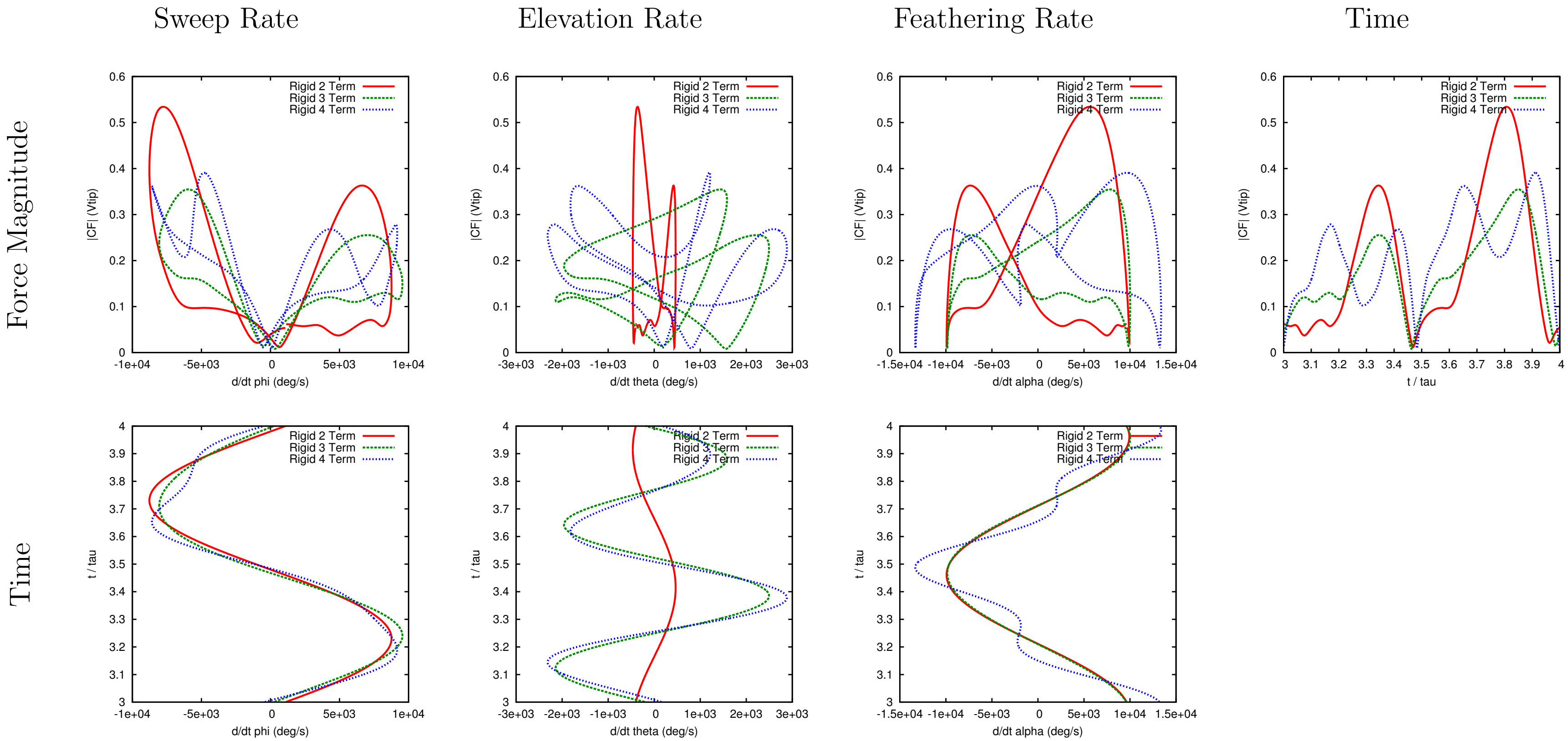

Figure 34: Plotting aerodynamic forces against the time-dependent kinematic rates for the 2-, 3-, and 4-term Fourier approximations highlight the sensitivity of the aerodynamic forces to the kinematic rates. Rigid wing solution.

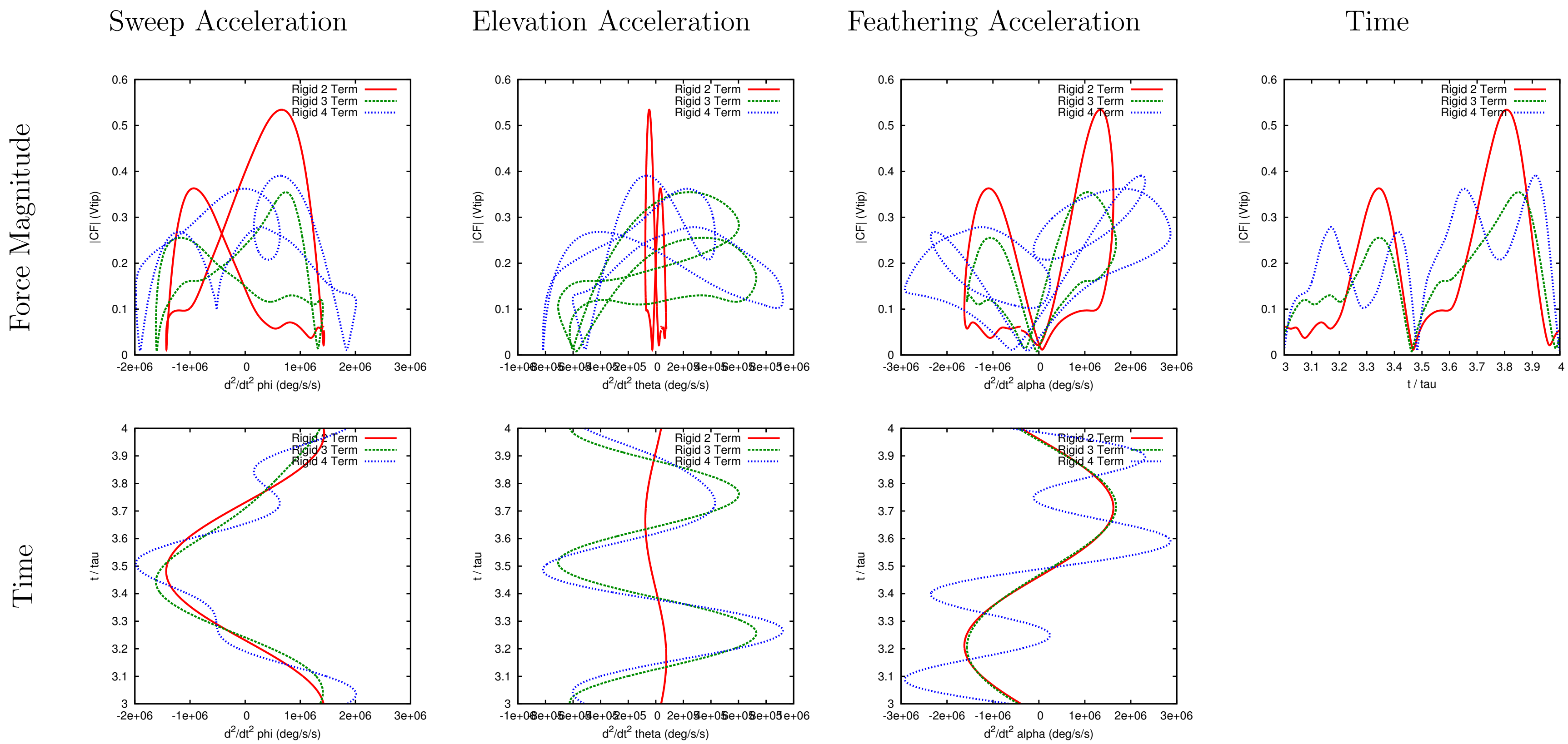

Figure 35: Plotting aerodynamic forces against the time-dependent kinematic accelerations for the 2-, 3-, and 4-term Fourier approximations highlight the sensitivity of the aerodynamic forces to the kinematic accelerations. Rigid wing solution.

5.2.3 Relationship of the Aerodynamic Forces to Wing Orientation. The timing of the maximum and minimum x-, y-, and z-direction forces is determined by the wing orientation during the wing stroke cycle. The peak aerodynamic forces occur near the maximum sweep rate, and the maximum sweep rate occurs at small values of the sweep parameter. At small sweep angles, the wing surface normals are primarily aligned in the x-z plane, producing peak x- and z-direction forces.

Peak side forces for the single wing simulations occur at the end of each half-stroke during the rotational phase of motion. The rotational phase of motion is characterized by large feathering rotations, during which the wing surface normals are rotating through the x-y plane. Because the surface normals are aligned close to the x-y plane, the pressure-based force contribution in the side, or y-direction is much greater than during the translational phase of motion.

The rotational phase of motion is also characterized by the role reversal of the "upper" and "lower" wing surfaces and the associated transition of the leading edge vortex from one wing surface to the opposite surface. There are also significant non-circulatory aerodynamic forces associated with the wing wake interaction and the acceleration of the wing as it changes direction of motion. The "upper" and "lower" wing surface transition is accompanied by a sharp change in the sign of the y-direction force at the beginning of the next half-stroke.

5.2.4 Spanwise Distribution of Aerodynamic Forces. Examining the spanwise force distribution highlights spatial variations in the force history that are not readily apparent when examining the time history of the net aerodynamic forces and provides insight into the timing and phase of the aerodynamic forces relative to the wing motion. Spatial force variations also highlight regions of the wing influenced by local fluctuations in the aerodynamic phenomena. Plotting the aerodynamic forces as a function of span and time provides a visual correlation between local wing orientation and the directionality of the net aerodynamic force.

Spanwise force distributions for the rigid wing solutions based on the 4-term kinematic profile are shown from the side, front, and top perspectives in Figures 36, 37, and 38. Following the spanwise forces through the flapping cycle, the 4-term forces peak early in each half-stroke, as seen at $t/\tau = 1/8$ and $5/8$, followed by a decrease in forces in the middle of each half-stroke, at $t/\tau = 1/2$ and 1. The decrease in forces is followed by another aerodynamic peak late in each half-stroke, seen at $t/\tau = 3/8$ and $7/8$. The aerodynamic forces produced early in the half-stroke exhibit a spanwise force distribution that peaks near the wing tip. This corresponds to the observed distribution of the strength and size of the leading edge vortex, which produces a conical structure increasing in diameter towards the wing tip. However, the increase in aerodynamic forces late in the half-stroke exhibit a more uniform force distribution when compared to the force distribution associated with the first aerodynamic peak. Compared to the early aerodynamic peak, the later peak at $t/\tau = 3/8$ and $7/8$ exhibits a significant force contribution near the wing root and a reduced contribution near the wing tip.

As discussed previously, the second aerodynamic peak corresponds with an increase in the feathering acceleration, or the rotational acceleration about the leading edge of the wing. Because the rectangular wing has a uniform chord length, the non-circulatory aerodynamic phenomena associated with the feathering rotation should have a consistent influence along the entire length of the wing. However, because of three-dimensional influences due to the finite length of the wing, and interactions with the other aerodynamic phenomena and the non-uniform wake, the actual force distribution is non-uniform.

Examining the force distribution at the transition from one half-stroke to the next, at $t/\tau = 0$ and $1/2$, the aerodynamic forces are acting in different directions along the wing length. This spanwise phase variation in the directionality of the aerodynamic forces illustrates how circulatory and non-circulatory forces interact to produce the complex force histories exhibited by flapping wing fliers. At the end of the half-stroke, the role of the "upper" and "lower" wing surfaces is changing as the wing undergoes the large feathering rotation. This is accompanied by the release of the leading edge vortex produced during the preceding the half-stroke into the wake, and the formation of a new leading edge vortex on the opposite wing surface as the wing changes direction of motion. The leading edge vortex is strongest towards the wing tip where the translational velocities are greatest, while the non-circulatory aerodynamic forces associated with the feathering rotation produce a more uniform set of forces along the wing length. It should be noted that this is a simplified discussion that neglects the influence of wing-wake interactions and the non-circulatory forces induced by the feathering and elevation accelerations.

The spanwise force distributions for the rigid wing solutions based on the 3-term kinematic profile, shown from the side, front, and top perspectives in Figures 39, 40, and 41, exhibit a similar spanwise force distribution to the 4-term rigid wing solutions through the wing stroke. The difference in spanwise forces early in the down stroke is shown in Figure 42. At $t/\tau = 5/8$, the aerodynamics should be dominated by the leading edge vortex, and variations in the aerodynamic forces will be due to variations in the strength of the leading edge vortex.

5.2.5 Three-Dimensional Wake.

Figure 43 highlights the wake structures produced by the rigid wing at pronation. The wake structure at pronation is influenced by the deceleration of the wing, which initializes the leading edge vortex on the "upper" wing surface and the starting vortex at the trailing edge of the wing. The wake is also influenced by the feathering rotation, which influences the starting vortex and pressure distribution along the wing surface. Visualizing the wake using iso-surfaces of vorticity in Figures 44 and 45, the leading edge vortex can be seen behind the leading edge on the "upper" wing surface, expanding in diameter from the wing root to the wing tip for the rigid wing simulations based on the 3- and 4-term kinematic profiles. Other vortical structures, such at the tip vortex and the starting and stopping vortices, can also be identified in the wake. The interaction of the leading edge vortex

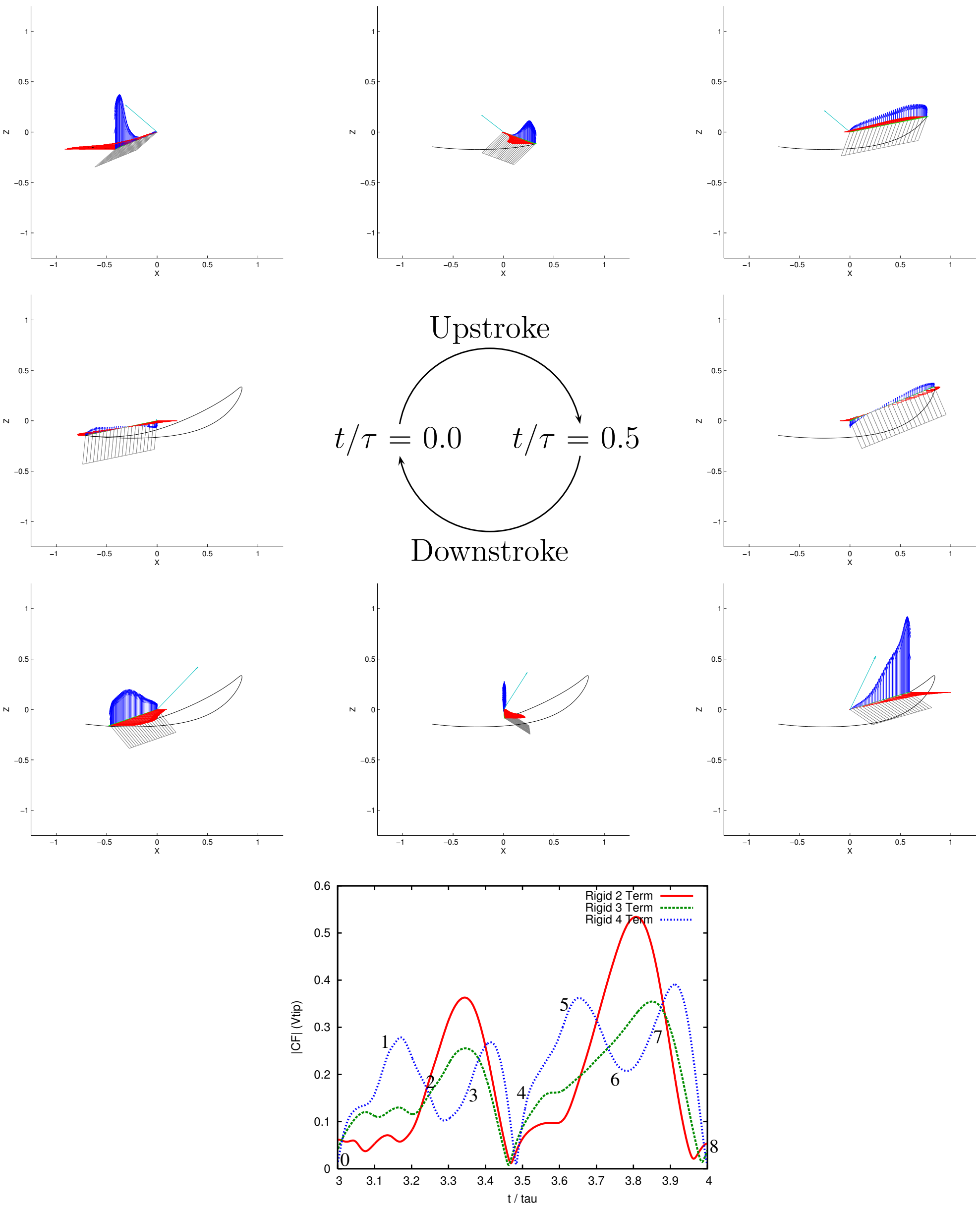

Figure 36: Span-wise force distribution for the rigid wing based on the 4-term kinematic profile. Left wing viewed from the left side. The three components of the sectional aerodynamic force are shown in red for the x-direction, in green for the y-direction, and in blue for the z-direction. The total aerodynamic force is shown in cyan at the wing root. The wing surface with chordwise marking is shown in gray and the tip path is shown in black.

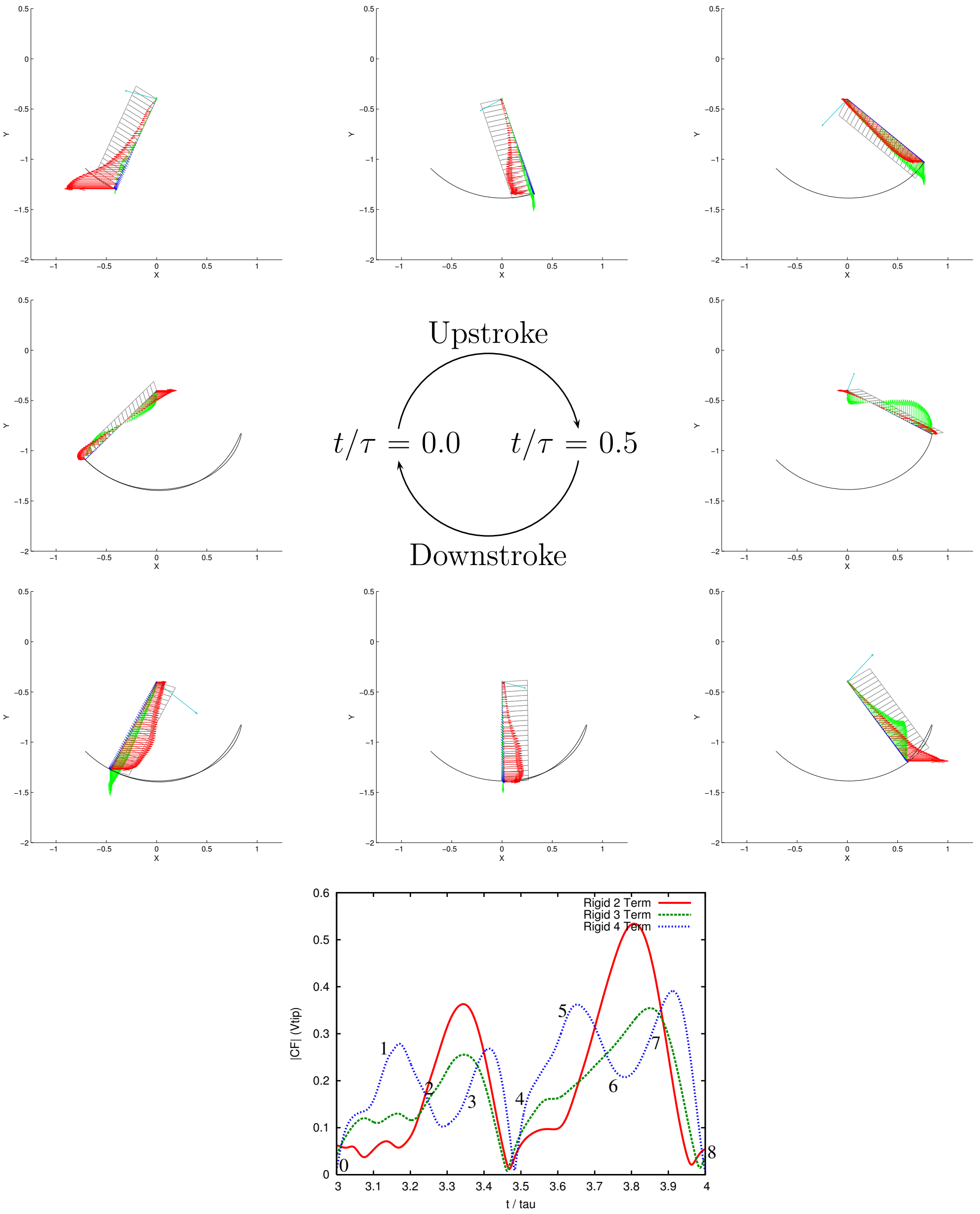

Figure 37: Span-wise force distribution for the rigid wing based on the 4-term kinematic profile. Left wing viewed from above. The three components of the sectional aerodynamic force are shown in red for the x-direction, in green for the y-direction, and in blue for the z-direction. The total aerodynamic force is shown in cyan at the wing root. The wing surface with chordwise marking is shown in gray and the tip path is shown in black.

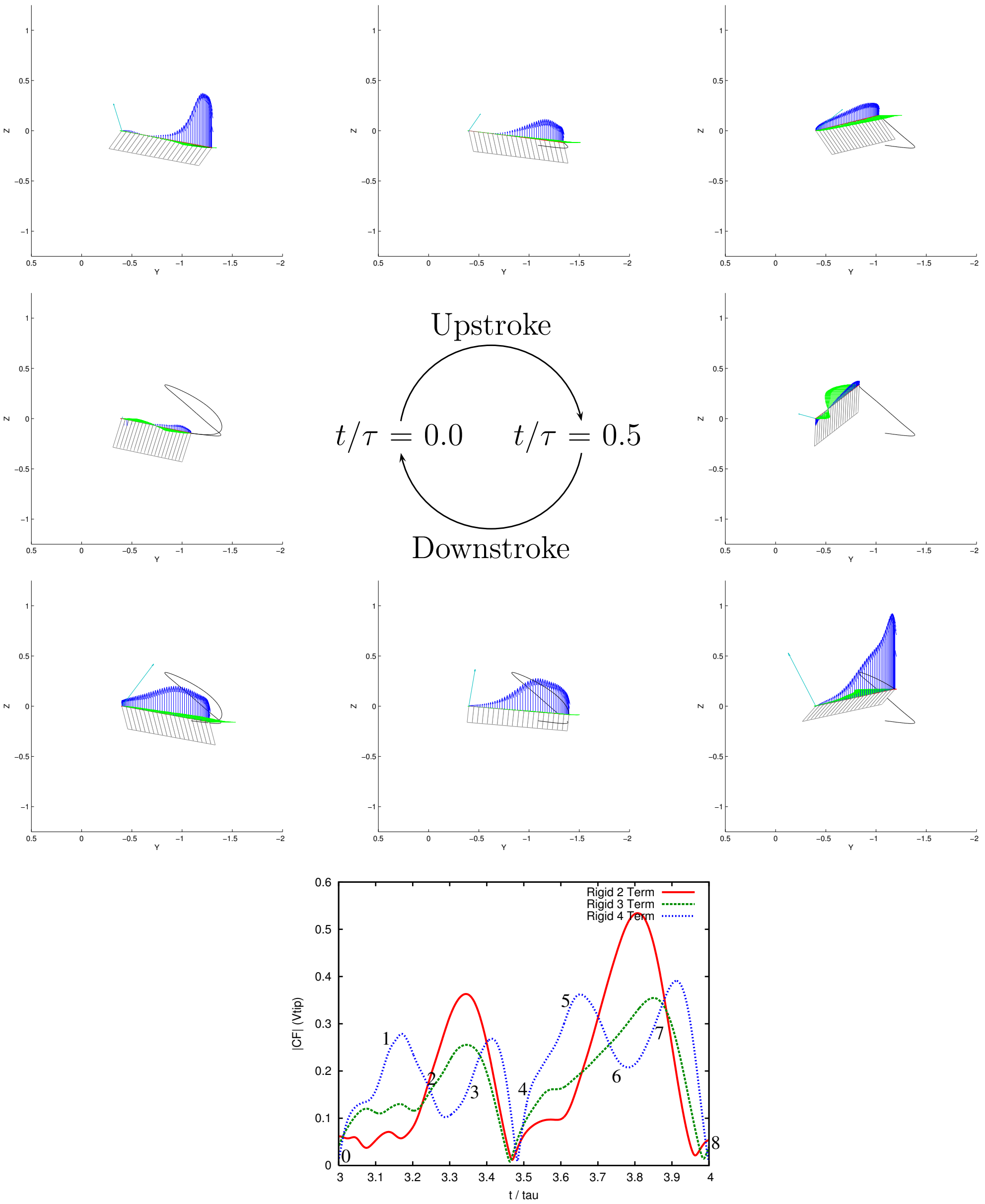

Figure 38: Span-wise force distribution for the rigid wing based on the 4-term kinematic profile. Left wing viewed from the front. The three components of the sectional aerodynamic force are shown in red for the x-direction, in green for the y-direction, and in blue for the z-direction. The total aerodynamic force is shown in cyan at the wing root. The wing surface with chordwise marking is shown in gray and the tip path is shown in black.

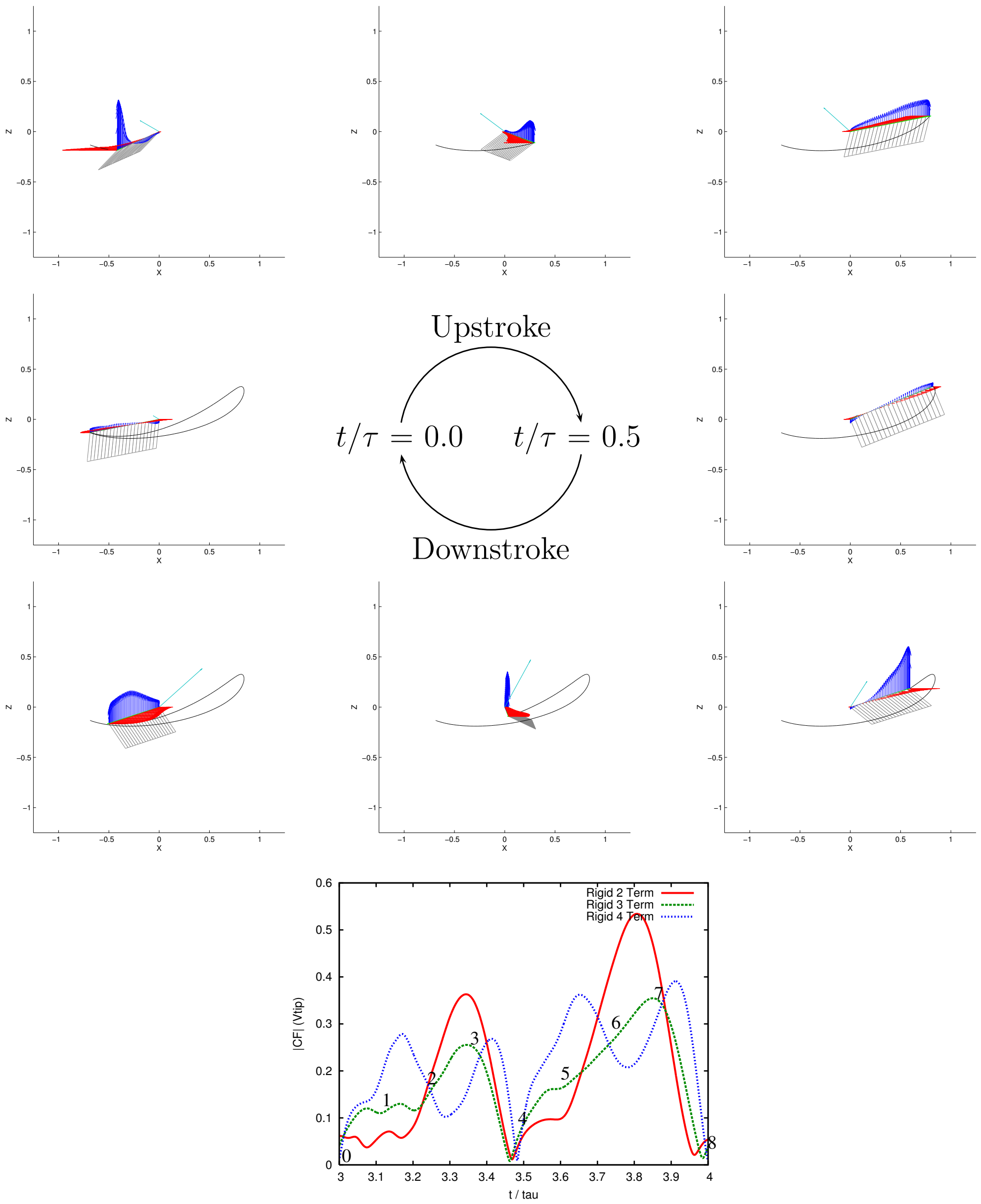

Figure 39: Span-wise force distribution for the rigid wing based on the 3-term kinematic profile. Left wing viewed from the left side. The three components of the sectional aerodynamic force are shown in red for the x-direction, in green for the y-direction, and in blue for the z-direction. The total aerodynamic force is shown in cyan at the wing root. The wing surface with chordwise marking is shown in gray and the tip path is shown in black.

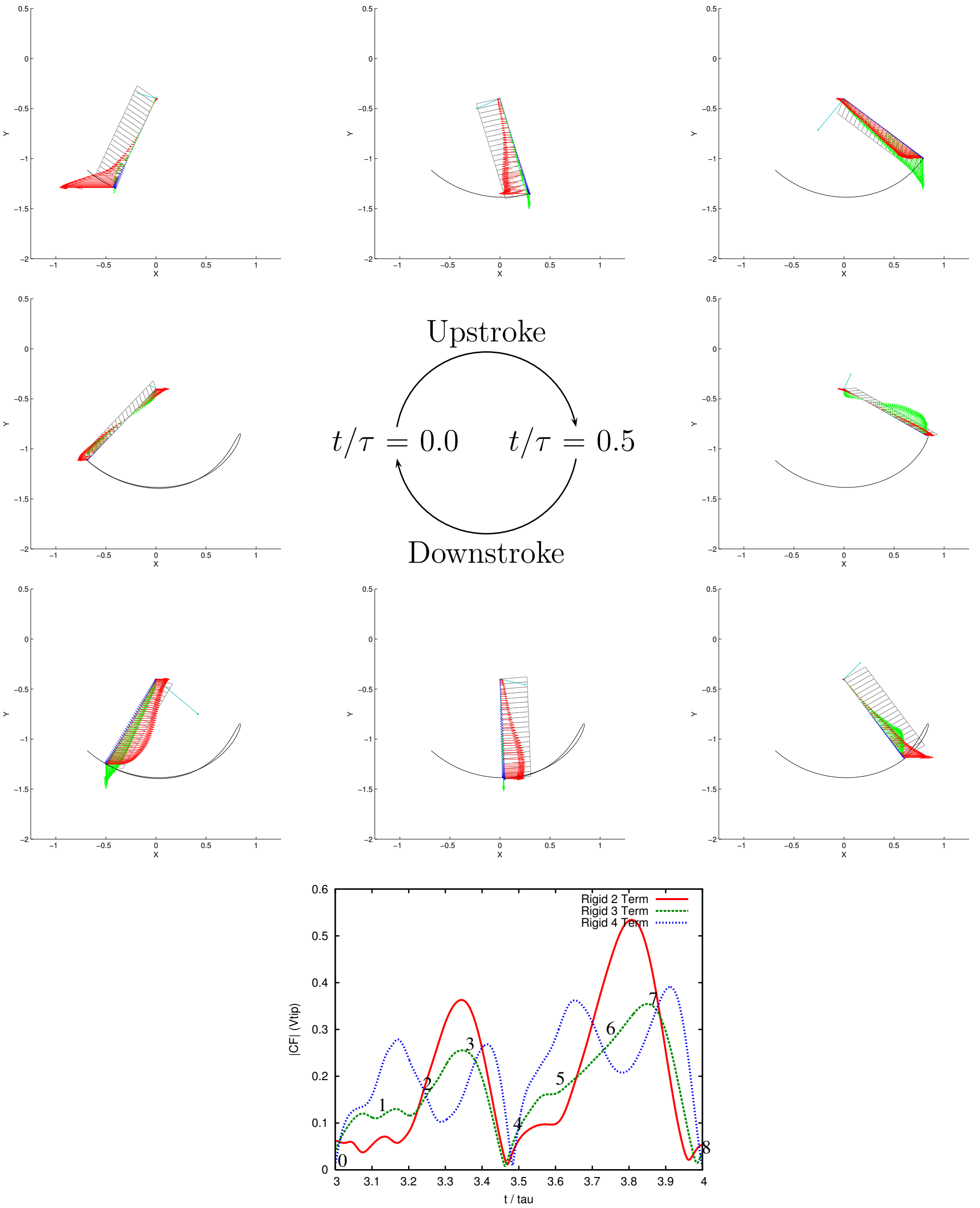

Figure 40: Span-wise force distribution for the rigid wing based on the 3-term kinematic profile. Left wing viewed from above. The three components of the sectional aerodynamic force are shown in red for the x-direction, in green for the y-direction, and in blue for the z-direction. The total aerodynamic force is shown in cyan at the wing root. The wing surface with chordwise marking is shown in gray and the tip path is shown in black.

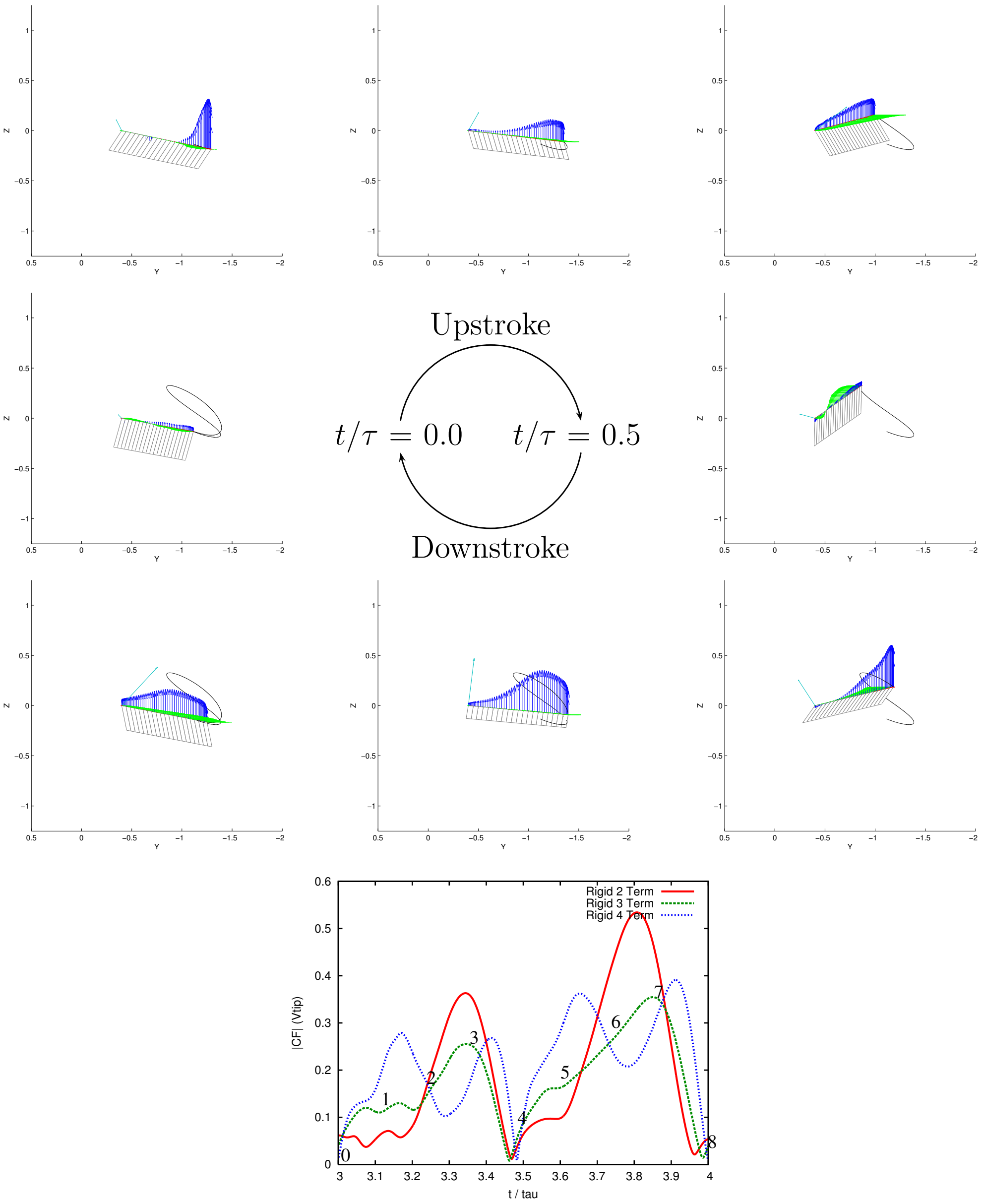

Figure 41: Span-wise force distribution for the rigid wing based on the 3-term kinematic profile. Left wing viewed from the front. The three components of the sectional aerodynamic force are shown in red for the x-direction, in green for the y-direction, and in blue for the z-direction. The total aerodynamic force is shown in cyan at the wing root. The wing surface with chordwise marking is shown in gray and the tip path is shown in black.

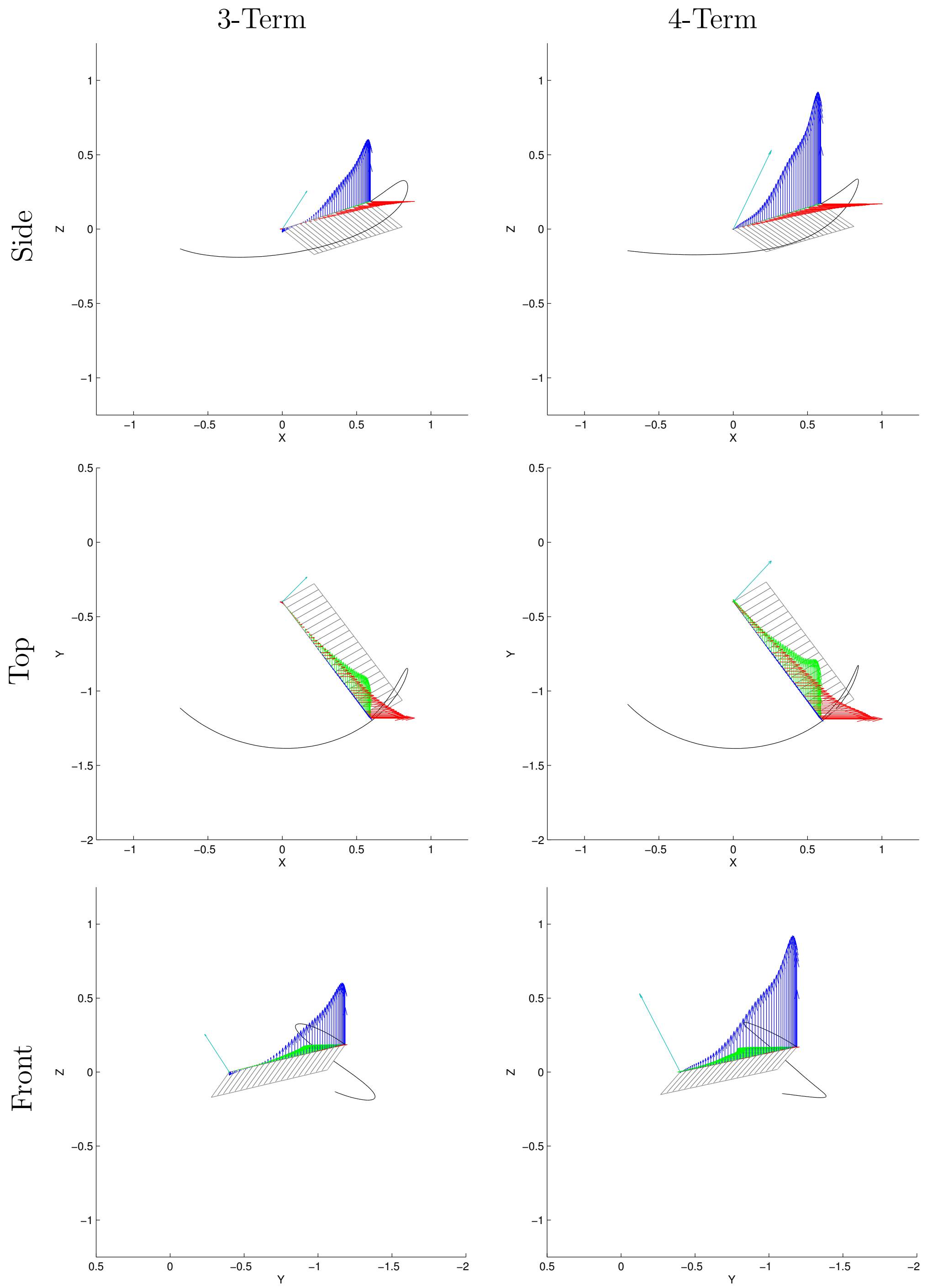

Figure 42: Spanwise forces at $t/\tau = 5/8$ for the 3-term and 4-term rigid wing solutions. The solutions exhibit similar force distributions with a significant variation in force magnitudes.

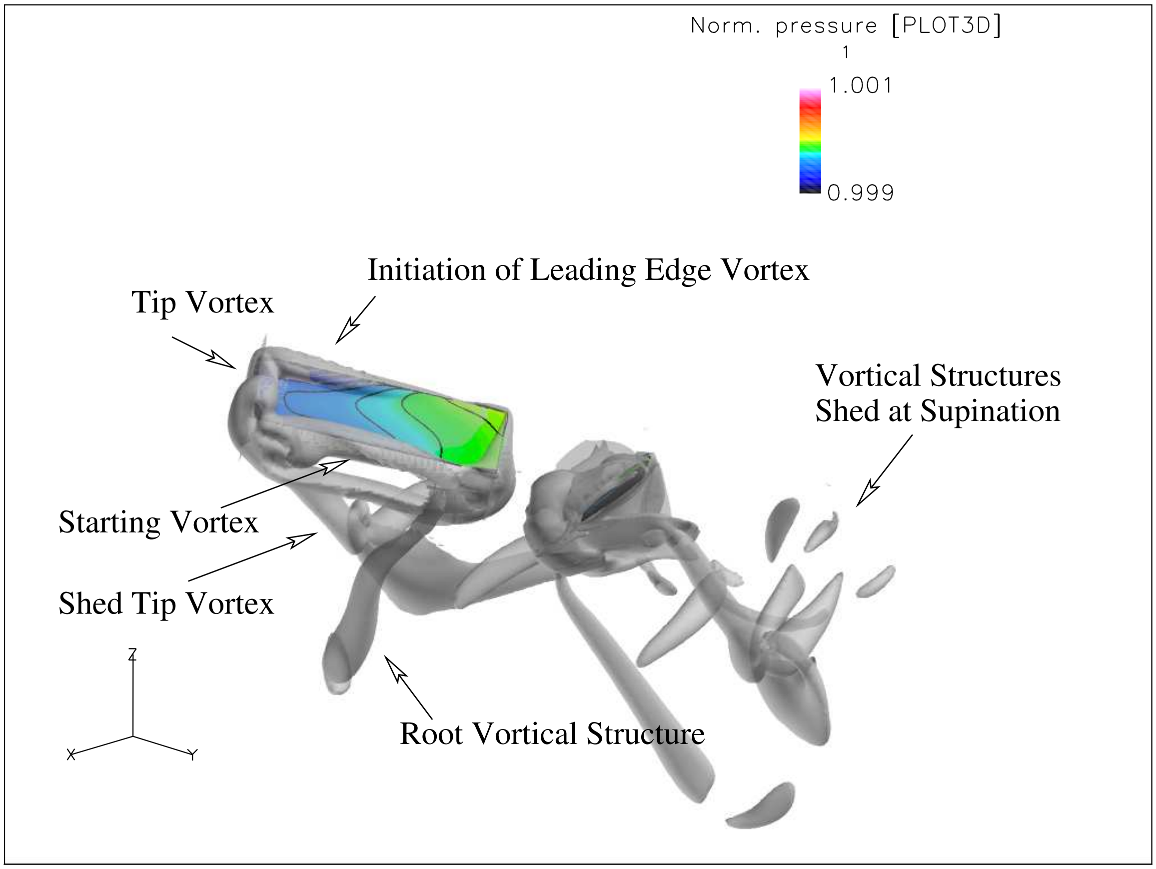

Figure 43: Annotated wake structures for the 4-term rigid wing simulations at $t/\tau = 0.6$. The wing is near the end of the feathering rotation at pronation and starting the sweep rotation for the downstroke.

with the tip vortex and the starting and stopping vortices leads to the complex wake structures and influence the evolution of the wake structure with time.

When the timing and orientation of the wake structures align, a momentum jet is produced, providing both lift and thrust for hover and forward flight. At hover, the momentum jet is aligned in the vertical direction, sustaining the weight of the Hawkmoth. The momentum jet produced by the rigid wing 3- and 4-term kinematic simulations are shown in Figures 46 and 47 using contours of the mean velocity field computed over the duration of one flapping cycle.

5.2.6 Mean Aerodynamic Forces and Aerodynamic Power Requirements.

Mean aerodynamic forces, moments, and power requirements were computed for the

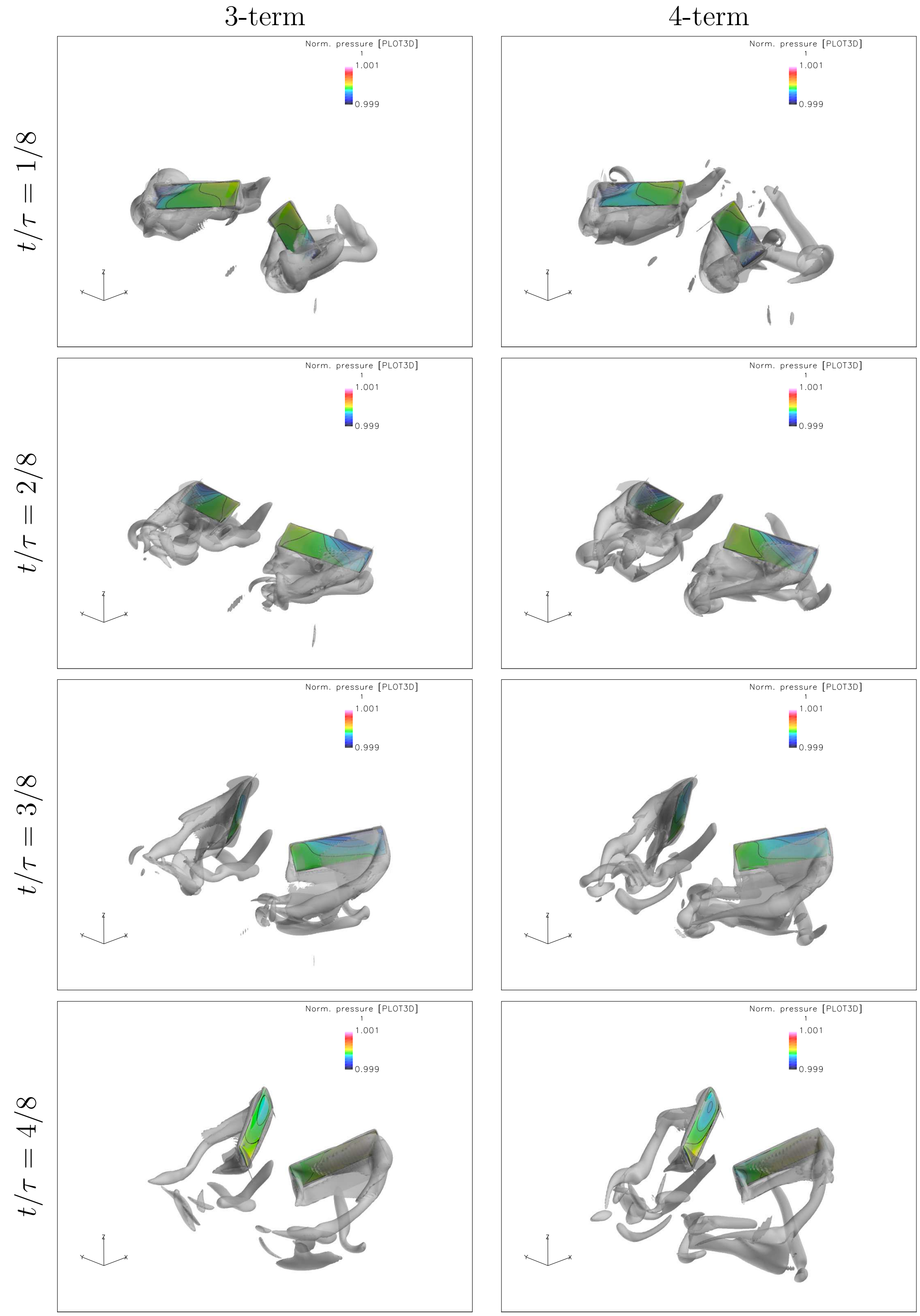

Figure 44: Iso-surface of vorticity magnitude for the 3- and 4-term kinematic profiles shown during the upstroke.

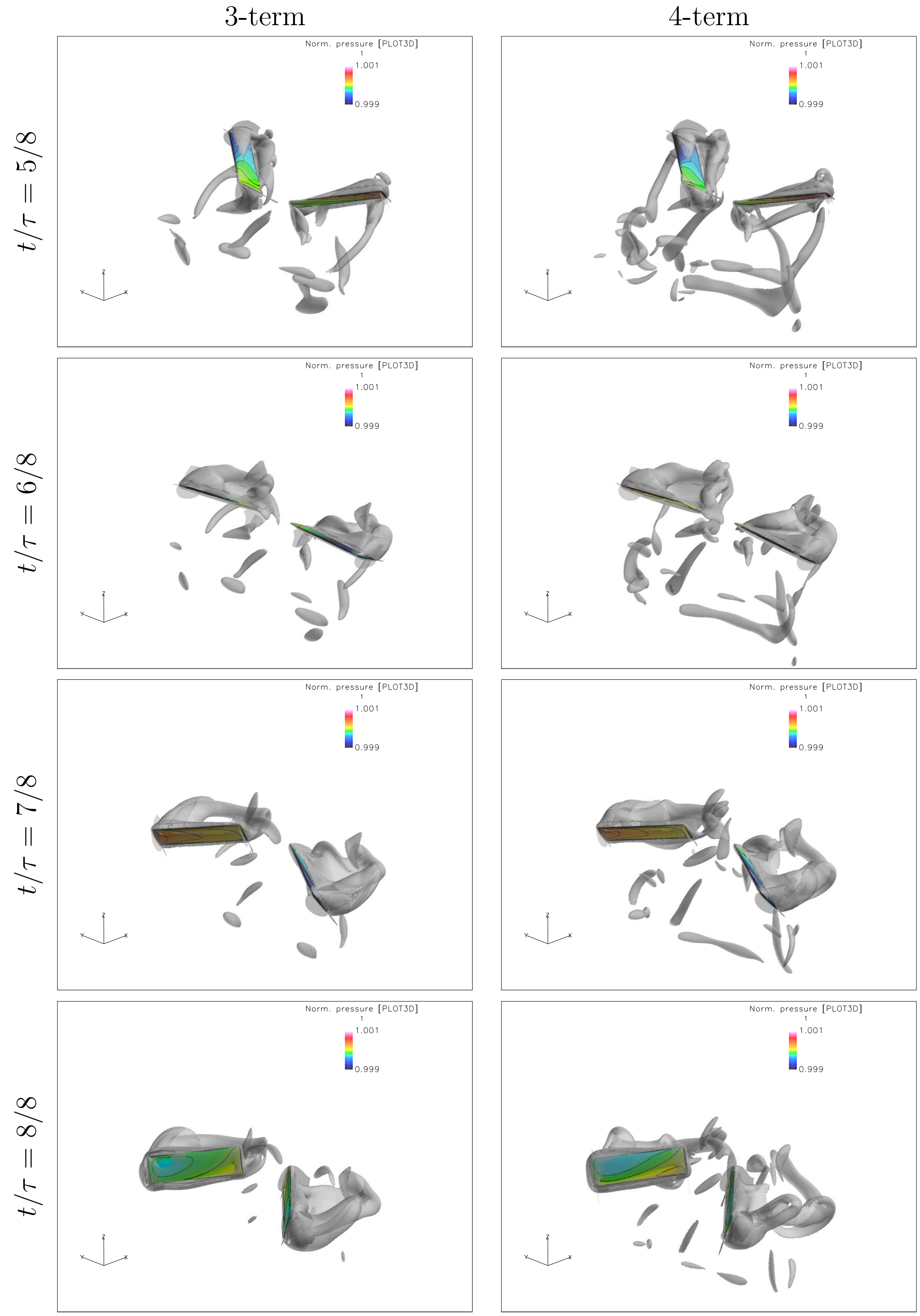

Figure 45: Iso-surface of vorticity magnitude for the 3- and 4-term kinematic profiles shown during the downstroke.

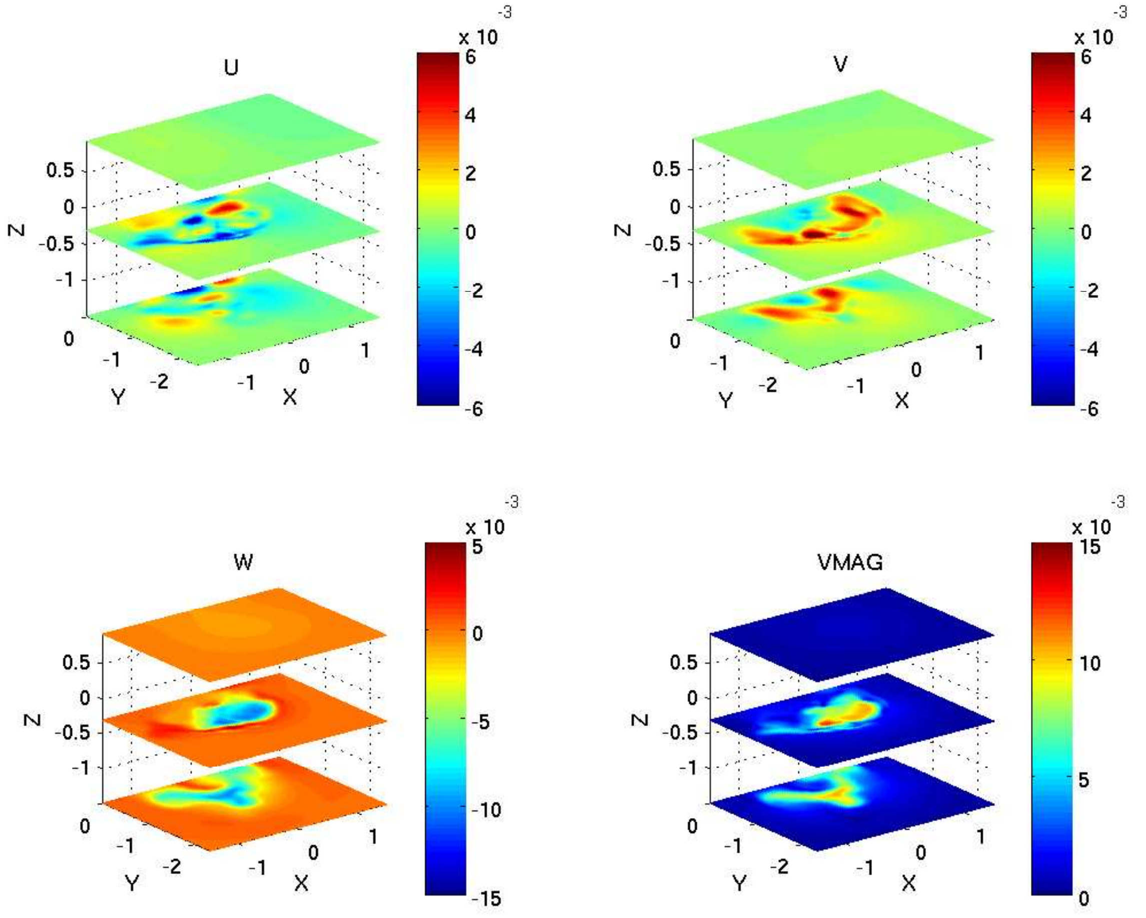

Figure 46: Mean velocity components normalized by tip velocity for the 3-term rigid wing simulation. The three xy-planes are above, immediately below, and below the stroke-plane. The coherent vertical momentum jet can be seen in the plots of the w-velocity component and the velocity magnitude.

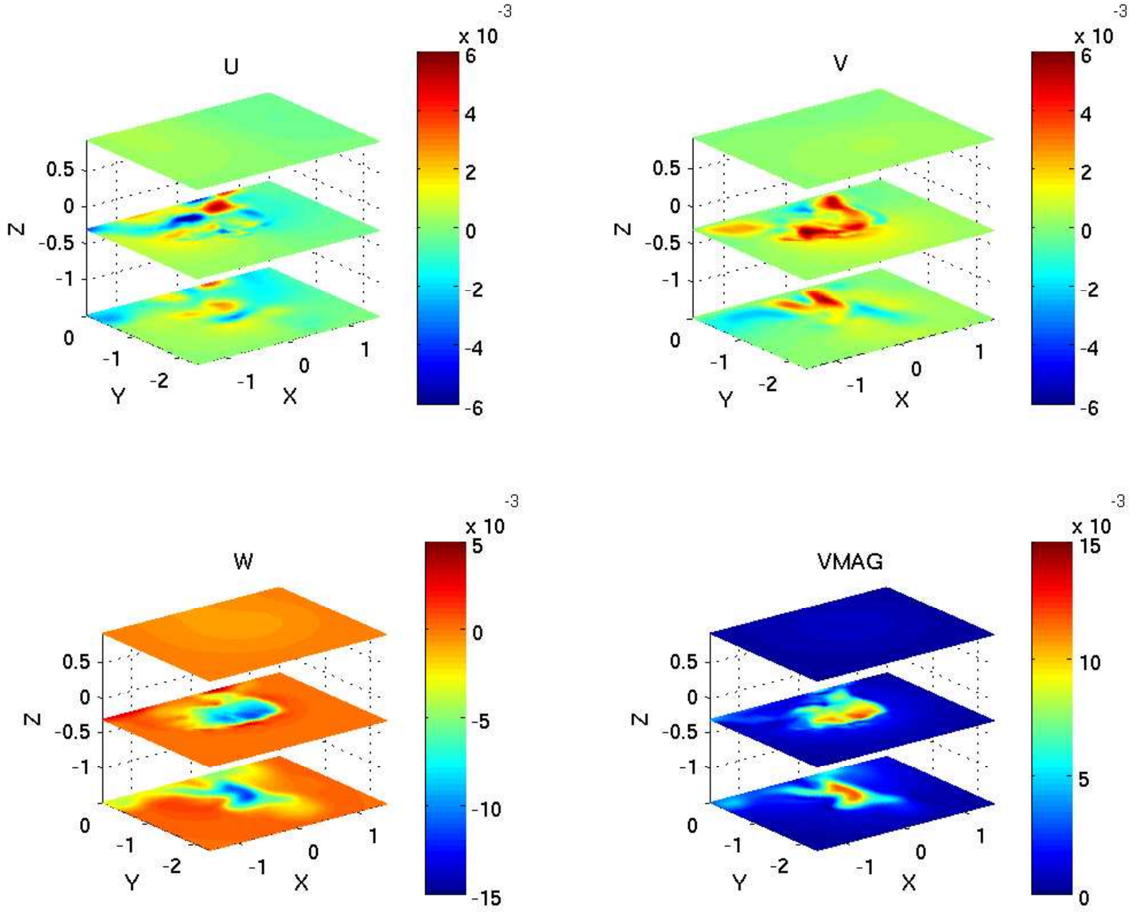

Figure 47: Mean velocity components normalized by tip velocity for the 4-term rigid wing simulation. The three xy-planes are above, immediately below, and below the stroke-plane. The vertical momentum jet can be seen in the plots of the w-velocity component and the velocity magnitude.

2-, 3-, and 4-term kinematic profiles in order to compare the performance. The mean aerodynamic forces, moments, and power requirements for the rigid wing solutions are presented in Table 3. Of the three kinematic profiles, the 4-term profile produced the largest mean vertical force, followed by the 2-term and 3-term profiles. However, the 3-term kinematic approximation was the most efficient of the three kinematic approximations in terms of mean vertical force compared to the mean aerodynamic power required.

Table 3: Computed aerodynamic forces, moments, and power requirements non-dimensionalized by the dynamic pressure at the wing tip for the 2-, 3-, and 4-Term kinematic profiles, rigid wing solution

	2-Term	3-Term	4-Term
CFx	1.165×10^{-02}	3.638×10^{-03}	1.779×10^{-04}
CFy	-2.919×10^{-02}	-1.625×10^{-02}	-2.841×10^{-04}
CFz	1.136×10^{-01}	1.249×10^{-01}	1.211×10^{-01}
CMx	-7.325×10^{-02}	-7.608×10^{-02}	-7.390×10^{-02}
CMy	-1.388×10^{-02}	-1.280×10^{-02}	-1.087×10^{-02}
CMz	6.108×10^{-03}	4.001×10^{-03}	4.942×10^{-03}
CP	6.755×10^{-02}	7.229×10^{-02}	7.752×10^{-02}
η_{aero}	$1.682\times10^{+00}$	$1.728\times10^{+00}$	$1.562\times10^{+00}$

5.3 Summary

Examining the influence of kinematic variation on the unsteady aerodynamic phenomena using a truncated Fourier approximation of the kinematic parameters does not allow for the influence of a specific kinematic parameter to be examined. Documenting the influence of a specific kinematic parameter on aerodynamic performance would require the kinematic parameters to be defined such that specific parameters could be perturbed, or by mixing the number of Fourier terms used to define a given kinematic profile. A kinematic profile could be defined using a 1-term Fourier approximation of elevation, a 3-term Fourier approximation of feathering, and a 2-term Fourier approximation of sweep, and so forth. However, such analysis would require a significant increase in the number of required simulations.

Examining the influence of the Fourier approximation on aerodynamic performance provides insight into the sensitivity of the aerodynamic forces and unsteady aerodynamic phenomena to the kinematic approximation used as a baseline for examining the influence of structural response. This examination highlighted the coupling between the strength of the leading edge vortex, a circulatory aerodynamic mechanism, with sweep rate and feathering orientation. Also highlighted was the influence of the feathering acceleration on the non-circulatory aerodynamic forces produced during the rotational motion at the end of each half-stroke. Identifying and understanding each of these interactions provides insight into how structural response may alter the strength and timing of the aerodynamic phenomena and aerodynamic forces, as the influence of structural response may be conceptualized as local kinematic variations.

Willmott and Ellington noted that the 4-term Fourier approximation of the kinematic parameters defined in Equations (22), (23), and (24) adequately represented the experimentally documented wing motion while minimizing the influence of spurious higher order harmonics due to the experimental approach on the kinematic rate and acceleration profiles [6]. Comparing the aerodynamic force histories and the unsteady aerodynamic phenomena produced by the 2-, 3-, and 4-term kinematic profiles presented in this chapter, the aerodynamic response is clearly sensitive to variations in the kinematic rate and acceleration profiles, as well as phase variations between the kinematic parameters.

VI. Analysis of Feathering Variation

As discussed in the previous chapter, the unsteady aerodynamic phenomena are sensitive to variations in velocity, acceleration, and orientation of the wing throughout the wing stroke. It has been demonstrated that variations in the rigid wing kinematics impact the time history of the aerodynamic forces and the wake structures by altering the local aerodynamic phenomena. Incorporating structural response into the current analysis introduces local variations into the velocity profile and orientation of the wing. These local variations have the potential to influence aerodynamic performance in a similar manner to the kinematic variations. Yet, the influence of structural response on aerodynamic performance has not been well studied.

To understand the influence of structural flexibility on the underlying unsteady aerodynamic mechanisms and aerodynamic performance, deformations of the wing surface were prescribed as a function of spanwise location and time in the wing local reference frame. When these local deformations are superimposed onto the rigid wing motion defined by the kinematic parameters, it is possible to mimic the flexible wing motion observed for natural fliers in free-flight.

OVERFLOW 2.1-Elastic is able to simulate the flow-field about flexible bodies exhibiting "beam type" deformations where the time-dependent deformation of the body is described using a combination of local displacements, δ_x, δ_y, δ_z, and rotations, θ_x, θ_y, θ_z, along a defined elastic axis. Applied to the flapping wing problem, these beam-type deformations may be used to model feathering, or torsion about the feathering axis, and bending along the wing length. The algebraic mesh deformation scheme is not able to accommodate "plate type" deformations associated with chordwise deformations, or adaptive camber, of the wing section as implemented. The types of flexible wing motion that may be modeled using this approach are illustrated in Figure 48.

With the ability to simulate flexible wing structures using local rotations and deformations along a defined elastic axis, the limited kinematic data documenting the spanwise feathering variation was used to examine the influence of spanwise feathering on the local aerodynamic phenomena.

6.1 Prescribed Feathering as a Function of Span and Time

The feathering profile used by Liu [19] and Aono [24] to define the "rigid-wing" motion of the Hawkmoth wing in time is based on a mean of the feathering profiles recorded at multiple spanwise locations. The rigid feathering profile is based on feathering profiles at spanwise locations from $r/R = 0.6$ to 0.9 recorded by Willmott and Ellington [17]. The feathering profiles measured along the wing length form the basis of the simulations incorporating prescribed feathering variations.

6.1.1 The Flexible Feathering Parameter. As with the time history of the kinematic parameters, the spatial distribution of the feathering parameter must be smoothed in such a way that the feathering variation is continuous from the wing root to wing tip for use with the numerical simulations. The spatial distribution of the feathering parameter could be represented using a set of experimentally determined modal contributions from a characterization of the Hawkmoth wing structure. Lacking this structural characterization of the Hawkmoth wing, it was assumed for this research that the spanwise feathering distribution could be represented using the first torsion mode of a fixed-free beam defined in Equation (25).

$$\Gamma_T(r) = \sin\left(\frac{r\pi}{2R}\right) \tag{25}$$

The full definition of the "flexible" feathering parameter in space and time, $\alpha(r,t)$, depends on a spatial distribution of the feathering parameter and time-dependent boundary conditions to scale the feathering variation in time. The amplitude of the first torsion mode defined in Equation (25) ranges from 0 to 1 along the wing length. If the orientation of the wing root is fixed, or constant in time, and the feathering orientation at the wing tip is centered about zero, the spatial distribution may simply

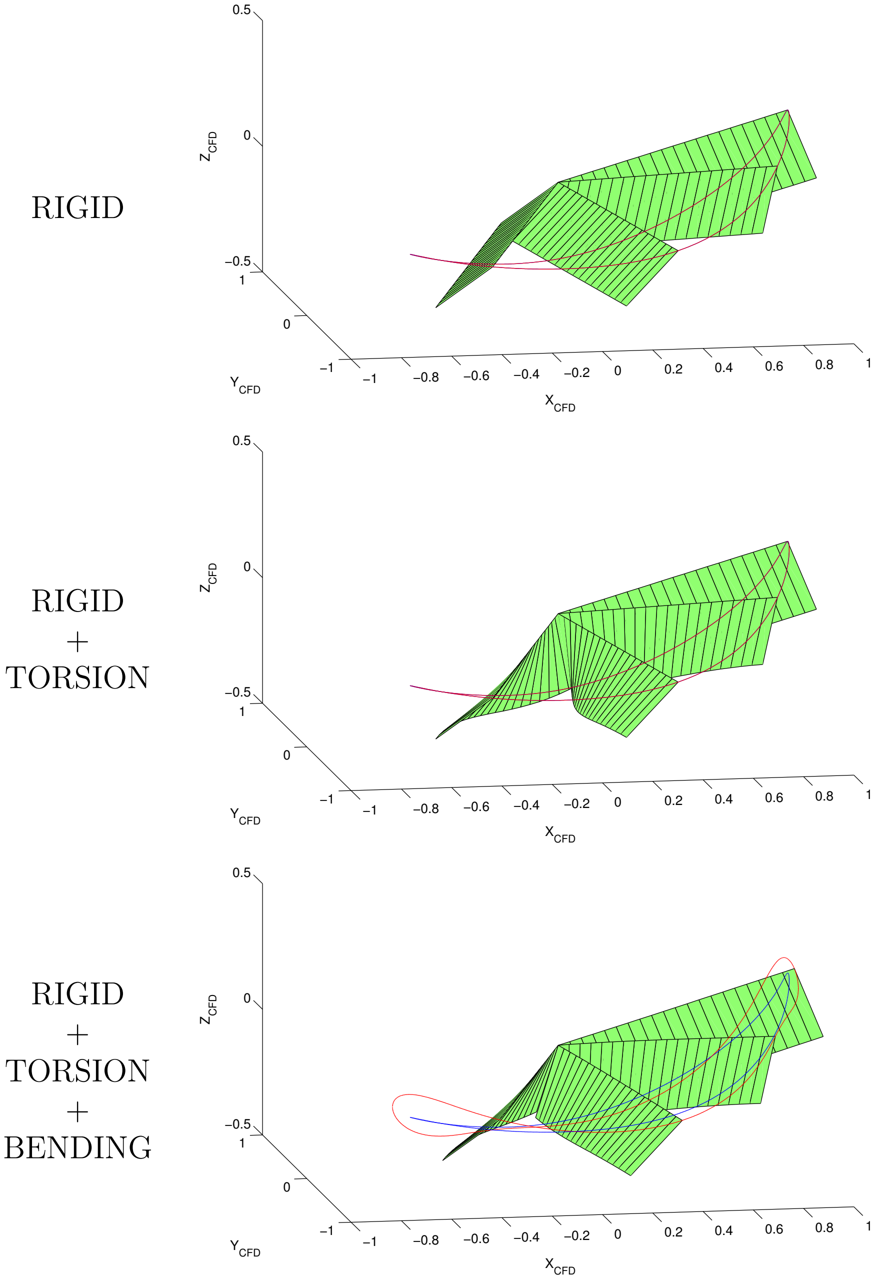

Figure 48: Examples of the flexible wing motion during the upstroke incorporating bending and torsion modes for an elastic axis along the leading edge of the wing. The red line represents the flexible wing tip path during the wing stroke and the blue line represents the rigid wing tip path. These are the types of deformations that may be captured using OVERFLOW 2.1-Elastic.

be scaled by the amplitude of the feathering orientation at the wing tip to define the flexible feathering orientation as a function of time and wing length, as in Equation (26).

$$\alpha(r,t) = \alpha_{tip}(t)\Gamma_T(r) \tag{26}$$

For cases where the wing root is not fixed in time or the feathering parameter is not centered around zero, as is the case for the Hawkmoth kinematics, a flexible feathering distribution may be defined using the amplitude of the feathering variation between the wing root and wing tip, $\delta_\alpha(t) = \alpha_{tip}(t) - \alpha_{root}(t)$, and the feathering orientation at the wing root, as defined in Equation (27).

$$\alpha(r,t) = \alpha_{root}(t) + \delta_\alpha(t)\Gamma_T(r) \tag{27}$$

To maintain consistency with the rigid wing simulations, the rigid wing feathering parameter was used to define the wing tip orientation, while the amplitude of the feathering orientation at the wing root was varied to represent wings with varying amounts of torsional flexibility.

The ability of the first torsion mode to capture the spanwise feathering distribution measured by Willmott and Ellington [17] is shown in Figure 49. The first torsion mode captures the dominant feathering variation from the wing root to the wing tip. A better capture of the recorded feathering variation may be achieved with the inclusion of higher-order torsion modes once a structural characterization of the Hawkmoth wing is available.

6.2 Influence of the Feathering Variation on the Aerodynamic Response

To assess the influence of the spanwise feathering variation on the unsteady aerodynamic phenomena and aerodynamic performance, simulations based on the 3- and 4-term kinematic profiles were computed for three amplitudes of the feathering variation, δ_α. The rigid wing simulations, discussed in Chapter V, represent 0%

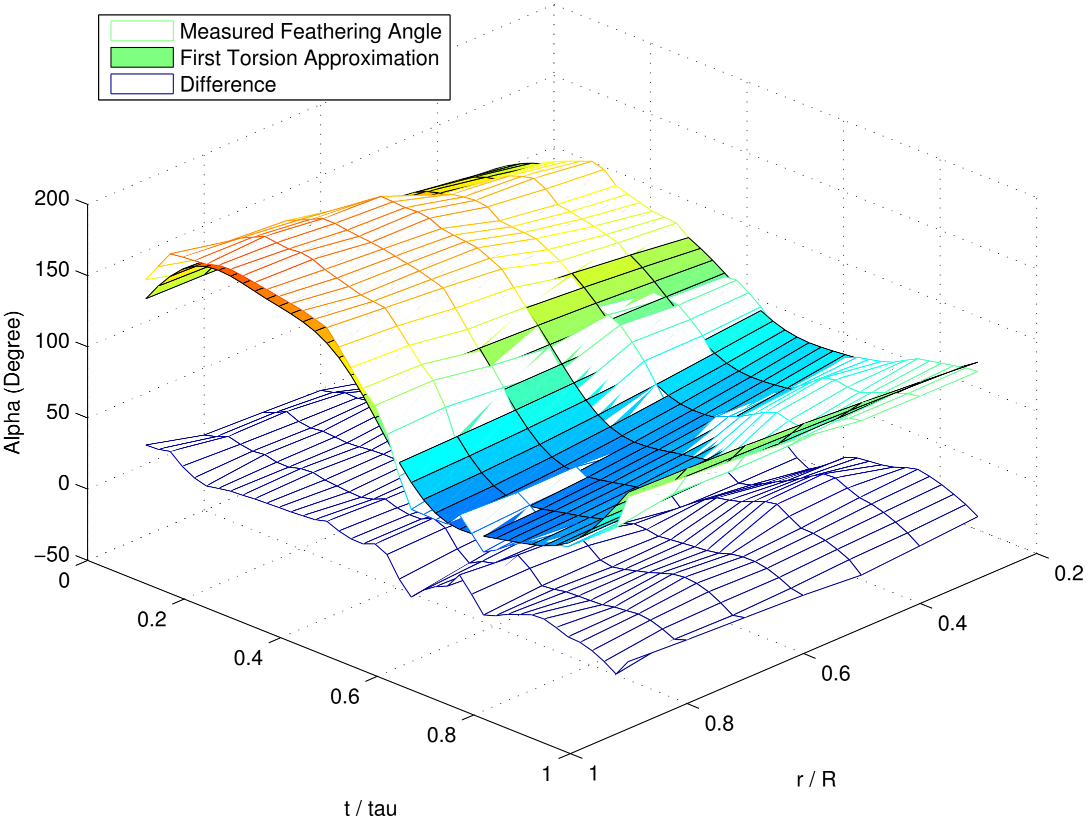

Figure 49: The flexible feathering parameter, $\alpha(r,t)$ approximated using a first-torsion span-wise distribution where $\alpha_{root}(t) = 90$ degrees and $\alpha_{tip}(t)$ is based on the rigid wing feathering orientation. The measured feathering angles were digitized from Willmott and Ellington [17].

feathering where $\alpha_{root}(t) = \alpha_{tip}(t)$. Solutions were computed for a wing with a reduced amplitude feathering profile at the wing root, $\alpha_{root}(t) = 0.5\alpha_{tip}(t)$, representing 50% feathering, and for a wing with a fixed feathering orientation at the wing root, $\alpha_{root}(t) = 90$ degrees, representing 100% feathering. This 0%, 50%, and 100% feathering nomenclature is used throughout the remainder of this document when discussing the influence of prescribed feathering.

As discussed in the previous chapter, the 4-term kinematic profile was considered by Willmott and Ellington to be a reasonable reconstruction of the Hawkmoth wing motions [6]. Though the 3-term and 4-term kinematic profiles produce similar tip paths, the kinematic rates and velocities vary significantly. This variation in the velocity and acceleration profile has a significant influence on the force histories produced by the 3- and 4-term kinematic profiles, with the 3-term kinematic profile producing a single peak in the vertical force per half stroke and the 4-term kinematic profile producing two peaks in the vertical force per half-stroke. The 3-term kinematic profile represents a simplification in the underlying wing kinematics compared to the 4-term profile, as might be expected from simplified kinematic actuators that may used in the next generation of micro-aerial vehicles. The use of both 3- and 4-term kinematic profiles for examining the influence of structural flexibility allows for trends in the aerodynamic response to be identified that are not limited to a specific kinematic profile.

6.2.1 Influence on the Aerodynamic Force History. Increasing the torsional flexibility by decreasing the amplitude of the feathering profile at the wing root while maintaining a consistent feathering profile at the wing tip influences the timing and amplitude of the net aerodynamic forces produced by the 3-term kinematic profile, shown in Figure 50. The duration and magnitude of the single peak in the force magnitude and z-force component produced by the rigid wing, with 0% feathering, changes as the amount of feathering “flexibility” increases. Both the upstroke and downstroke see an increase in the force magnitude early in the half-stroke, leading to a longer duration of the sustained force magnitude. However, the peak value of the z-force component and force magnitude during the downstroke decrease with an increase in the feathering variation.

The timing of the changes in the force history provide clues to which aerodynamic phenomena are sensitive to changes in the spanwise feathering variation. Changes in the aerodynamic forces during the early and middle portions of the half-stroke influence the translational phase of motion that is dominated by the formation of the leading edge vortex and associated circulatory aerodynamic phenomena. Changes in the aerodynamic forces during pronation and supination indicate changes in the non-circulatory aerodynamic phenomena influenced by the feathering acceleration and wing-wake interactions that occur as the wing changes direction of motion, as discussed in Section 5.2.2.

At first glance, "increased torsional flexibility" appears to have a different influence on the aerodynamic forces produced by the 4-term kinematic profile, shown in Figure 51, than observed for the 3-term kinematic profile, shown in Figure 50. However, reducing the amplitude of the root feathering profile increases the magnitude of the initial aerodynamic peak during the early portion of each half-stroke, while decreasing the amplitude and altering the phase of the second aerodynamic peak late in the half-stroke. This is a similar behavior to that observed for the 3-term kinematic profile with an increase in torsional flexibility, if the underlying differences between the 3- and 4-term force histories are neglected.

6.2.2 Spanwise Velocity and Force Distributions. Introducing a spanwise feathering variation influences the geometric configuration of the wing during both phases of wing motion, translation and rotation. During the rotational phase of motion, the reduced amplitude of root feathering orientation reduces the accompanying feathering rate and acceleration of the inboard portion of the wing. This change in the feathering rate influences the velocity distribution along the wing length at every point not located on the feathering axis. The translational velocity of the wing at the

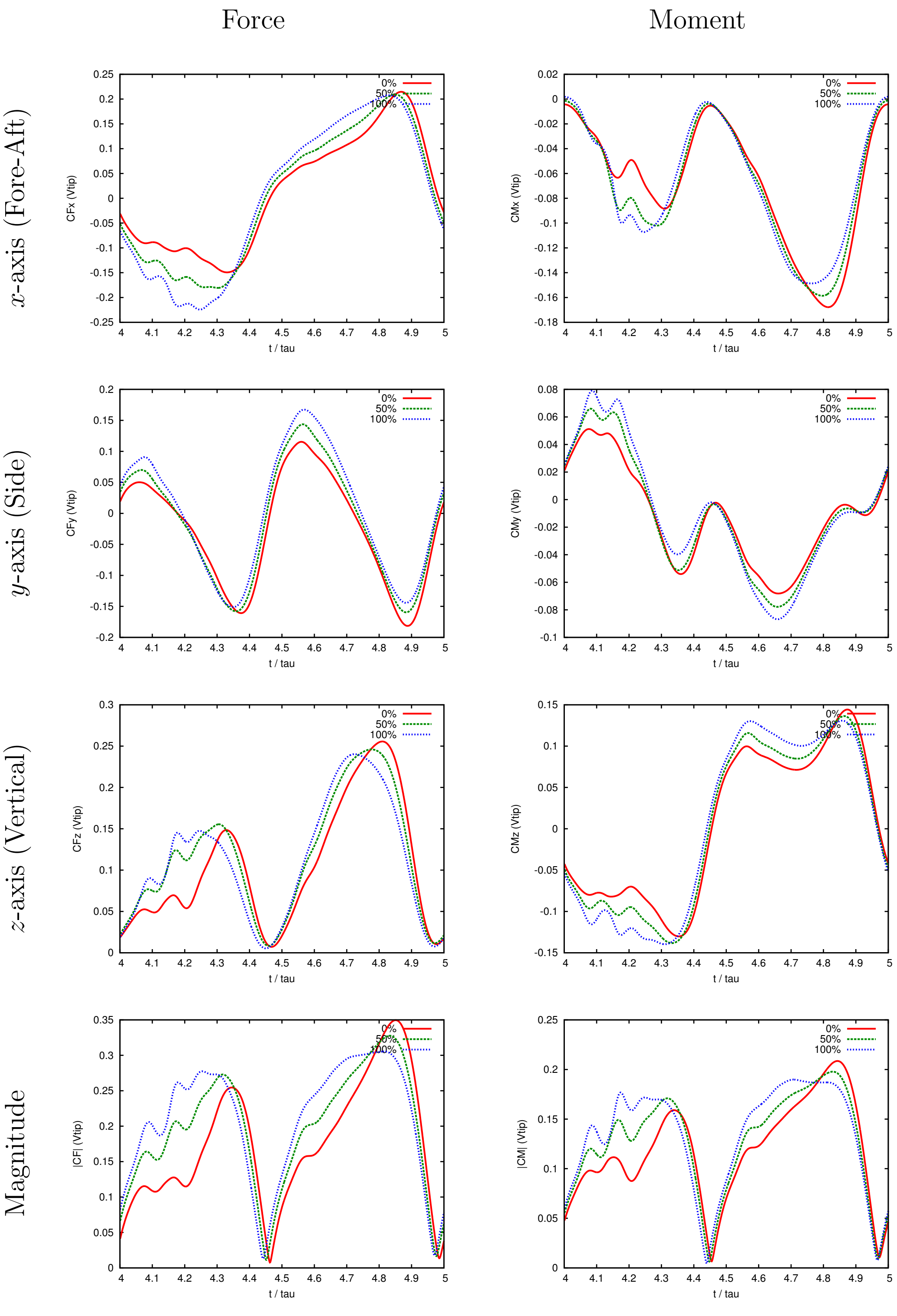

Figure 50: Aerodynamic force and moment histories for the torsionally flexible simulations. The wing kinematics are based on the 3-term Fourier approximation. The flier is oriented in a reference system with the x-axis aligned in the aft direction, the z-axis aligned in the vertical direction, and the y-axis aligned with the right wing.

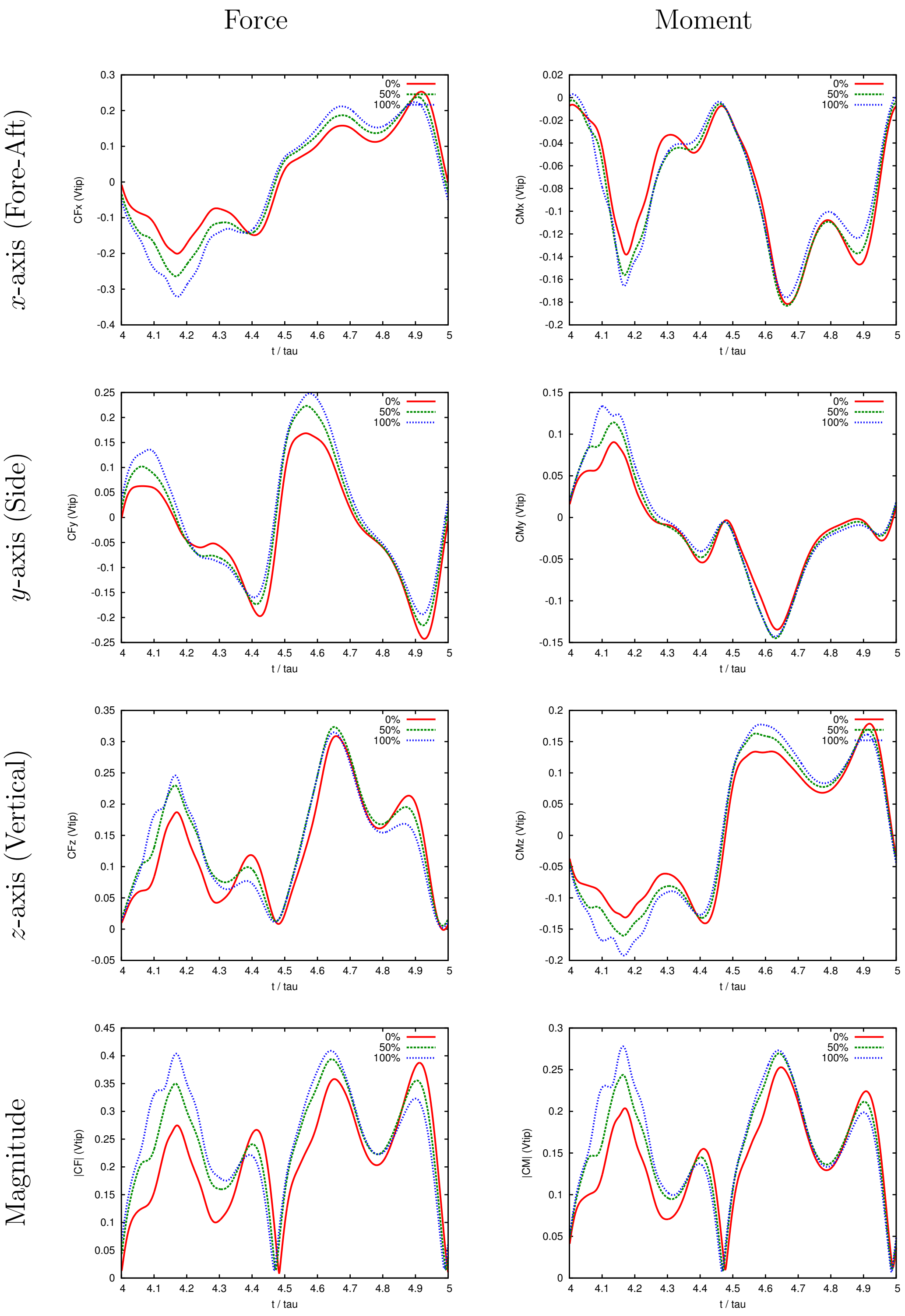

Figure 51: Aerodynamic force and moment histories for the torsionally flexible simulations. The wing kinematics are based on the 4-term Fourier approximation. The flier is oriented in a reference system with the x-axis aligned in the aft direction, the z-axis aligned in the vertical direction, and the y-axis aligned with the right wing.

three-quarter chord location is shown in Figures 52, and 53 using a set of red velocity vectors for the rigid wing, 0% feathering, and the 100% feathering wing as the wing approaches pronation, at $t/\tau = 3/8$, and just after stroke reversal, at $t/\tau = 4/8$. Figure 52 represents the force and velocity distribution for the 3-term kinematic profile and Figure 53 represents the force and velocity distribution for the 4-term kinematic profile.

At $t/\tau = 3/8$, the rigid wing velocity distribution for both kinematic profiles are linear at the three-quarter chord location and exhibits a non-zero velocity component at the wing root. This velocity distribution is accompanied by a spanwise force distribution at the leading edge of the wing, shown using a set of blue vectors in Figures 52 and 53, that exhibits a significant force contribution near the wing root. Contrasting the rigid wing velocity distribution to the torsionally flexible wing with 100% feathering variation, the velocity distribution of the 100% feathering wing at the three-quarter chord is not linear, but mirrors the spatial distribution of the feathering parameter. Since the orientation of the wing root is fixed at $\alpha_{root}(t) = 90$ degrees for the 100% feathering wing, the translational velocity of the wing approaches zero at the wing root. This change in the velocity distribution from the rigid wing is accompanied by a change in the spanwise force distribution. The force distribution of the 100% feathering wing exhibits a decreased contribution near the wing root, which corresponds to the decrease in the velocity distribution along the three quarter chord near the wing root. The middle third of the wing exhibits an increase in force amplitude when compared to the 0% feathering wing.

The influence of the spanwise variation in feathering rates is even more pronounced when contrasting the force distribution between the rigid and feathering wings just after stroke reversal, at $t/\tau = 4/8$, also shown in Figure 52 for the 3-term kinematic profile and Figure 53 for the 4-term kinematic profile. At $t/\tau = 4/8$, the wing has already changed direction of motion, as shown by the single red vector at the wing tip along the leading edge of the wing. This location is coincident with the feathering axis and not influenced by the feathering rate. However, because the wing is still pronating at the start of the downstroke, the contribution of the sweep rate to the translational velocity at the wing tip is negated by the contribution of the feathering rate about the leading edge at the three quarter chord. For the rigid wing, this leads to an “inverse” velocity distribution along the three-quarter chord of the wing with a greater translational velocity at the wing root than the wing tip. This “inverse” velocity distribution along the three-quarter chord is accompanied by a spanwise force distribution that shows significant forces on the “lower” wing surface near the wing root and the “upper” wing surface near the wing tip. Compared to the 0% feathering wing, the 100% feathering wing shows a velocity distribution along the three-quarter chord that is nearly zero along the length of the wing. This is accompanied by a spanwise force distribution that does not exhibit “reversed” forces along the length of the wing.

The influence of the altered force distributions on the net aerodynamic forces may be seen in the force histories at $t/\tau = 3/8$ and $t/\tau = 4/8$, shown in Figures 50 and 51 for the 3- and 4-term kinematic profiles. Due to the orientation of the wing surface, the change in the force distribution primarily influences the net aerodynamic forces in the x- and y-directions. The 100% feathering wing shows an increase in net x- and y-forces compared to the 0% feathering wing, or rigid wing, at both $t/\tau = 3/8$ and $t/\tau = 4/8$. The influence is most significant at $t/\tau = 4/8$ because the “reversed” forces of the rigid wing act in opposing directions, reducing the net aerodynamic forces.

During the translational phase of motion, the feathering variation influences the orientation of the wing relative to the direction of motion at the leading edge due to the sweep and elevation rates. This change in wing orientation, along with the change in wake structure near the wing root, to be discussed in the next section, influences the spanwise force distribution by increasing the amplitude of the aerodynamic forces in the inner and middle thirds of the wing length at $t/\tau = 1/8$ and $t/\tau = 2/8$, shown in Figure 54 for the 3-term kinematic profile and Figure 55 for the 4-term kinematic profile.

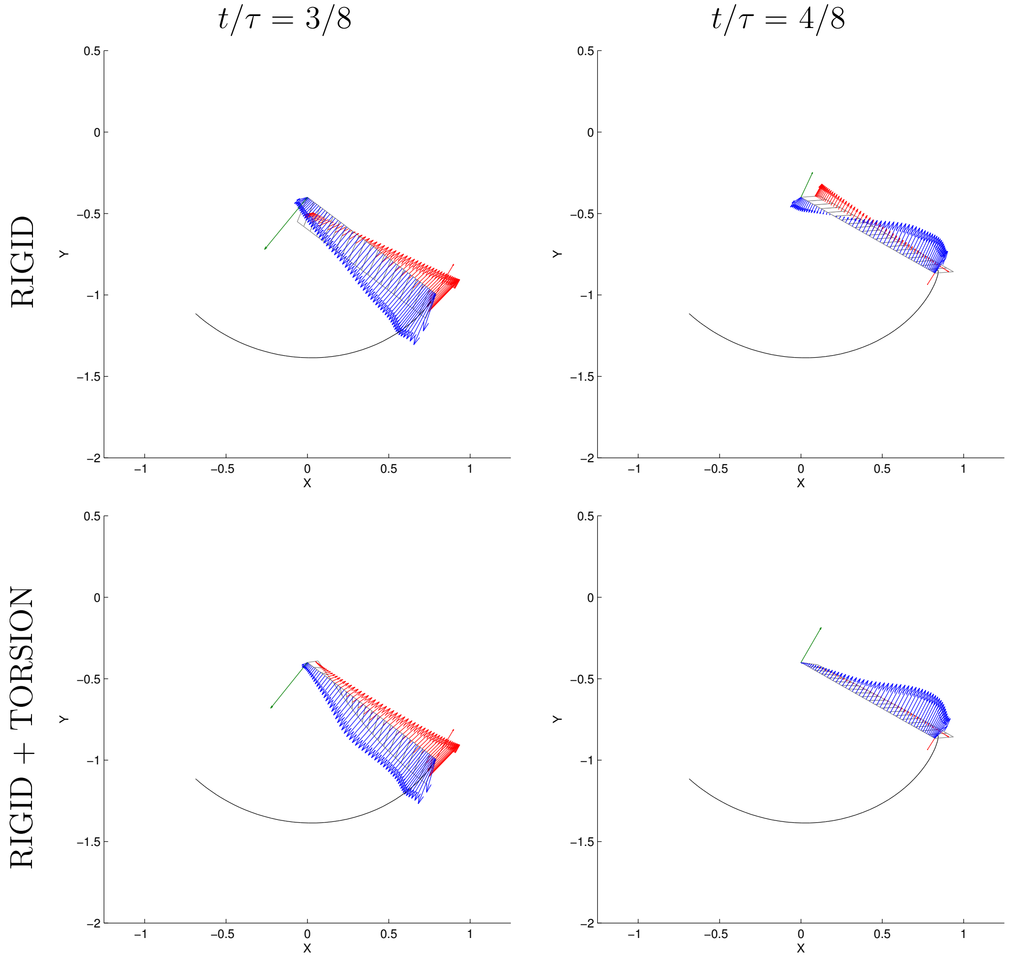

Figure 52: Comparison of the spanwise force distribution in blue to the linear velocity of the wing at the three-quater chord location in red for the rigid wing and prescribed feathering solutions. The wing motion is based on the 3-term kinematic profile.

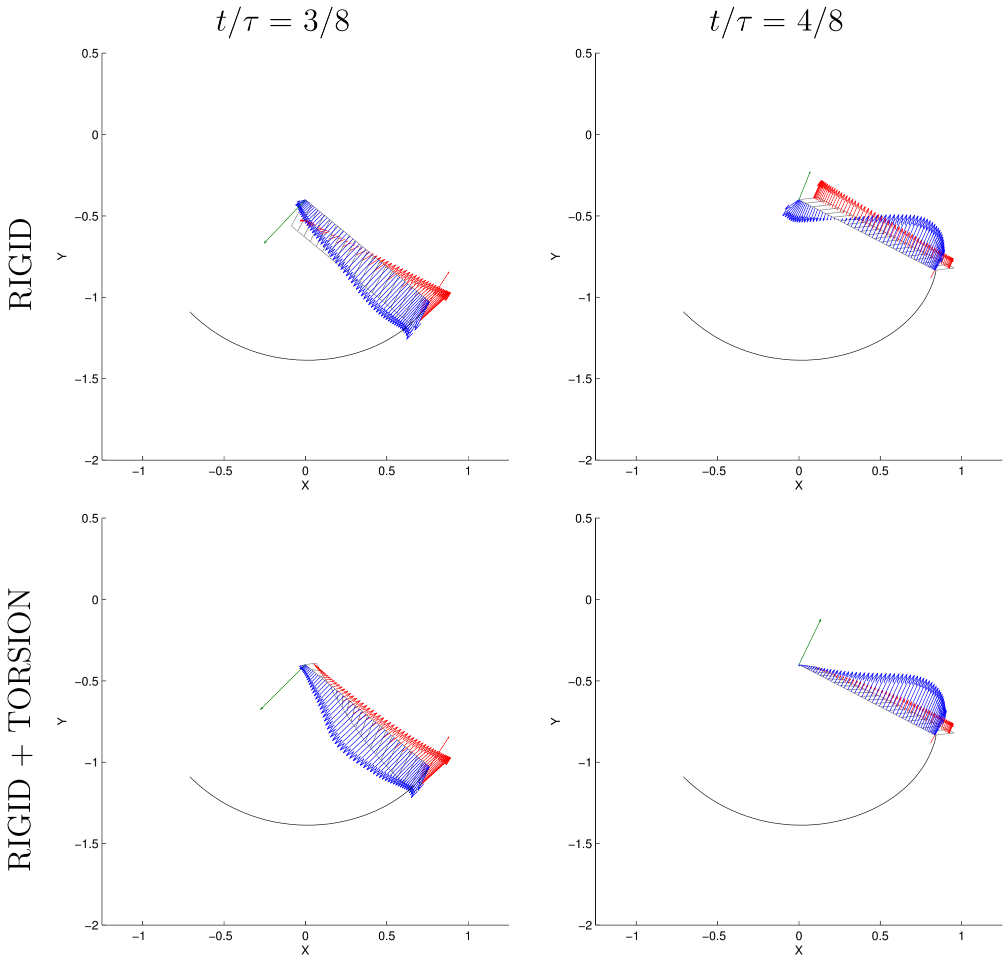

Figure 53: Comparison of the spanwise force distribution in blue to the linear velocity of the wing at the three-quater chord location in red for the rigid wing and prescribed feathering solutions. The wing motion is based on the 4-term kinematic profile.

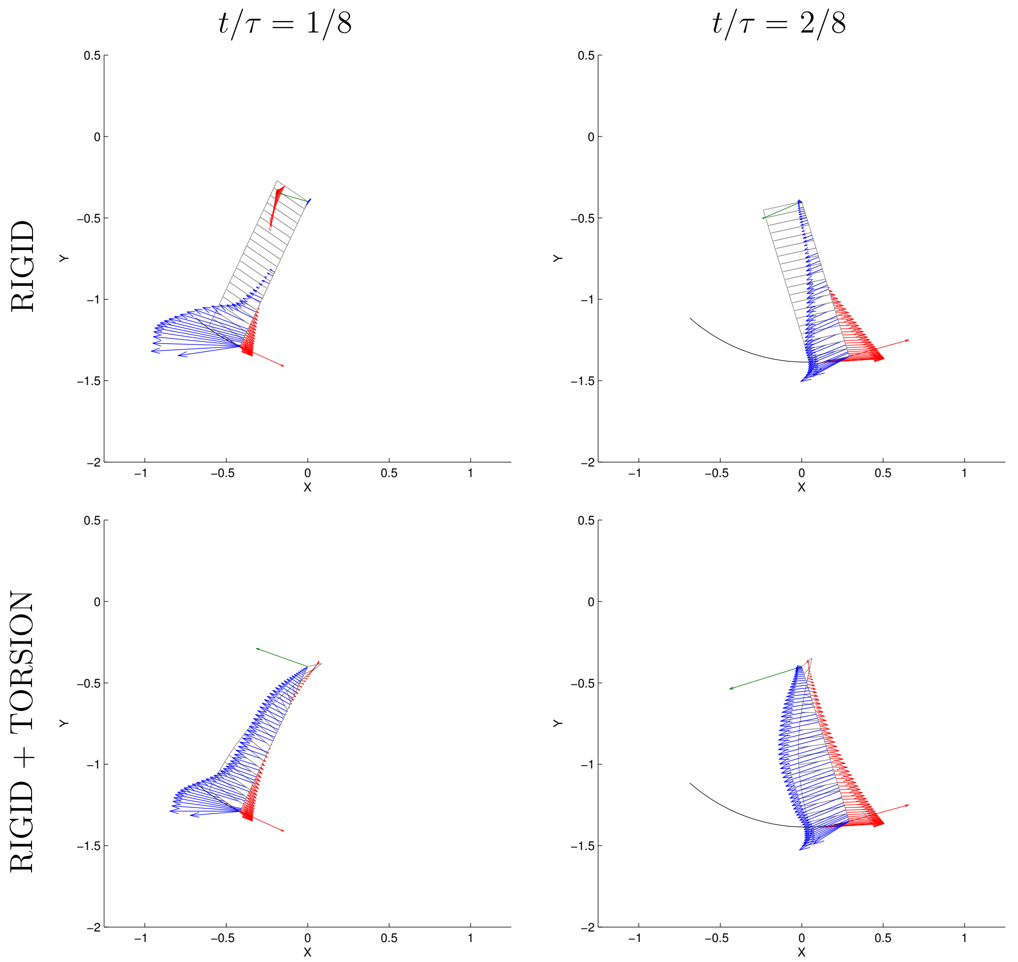

Figure 54: Comparison of the spanwise force distribution in blue to the linear velocity of the wing at the three-quater chord location in red for the rigid wing and prescribed feathering solutions. The wing motion is based on the 3-term kinematic profile.

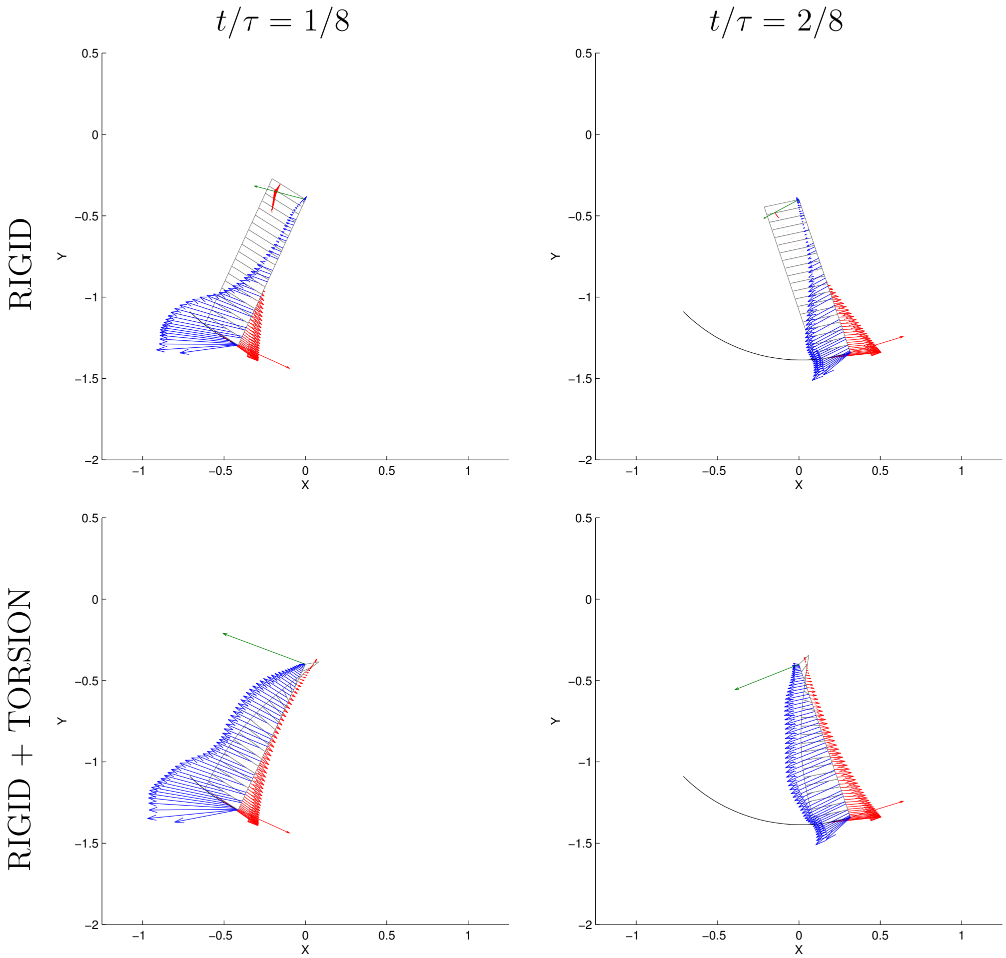

Figure 55: Comparison of the spanwise force distribution in blue to the linear velocity of the wing at the three-quater chord location in red for the rigid wing and prescribed feathering solutions. The wing motion is based on the 4-term kinematic profile.

The point of view at $t/\tau = 1/8$ and $t/\tau = 2/8$ mask the spanwise velocity distribution below the wing surface for each case except for the rigid wing at $t/\tau = 1/8$. The spanwise velocity distribution at the three quarter chord exhibits a "reversed" distribution where the three quarter chord near the wing root is moving to the left, or forward, while the wing tip is translating to the right, or aft. As with the rigid wing during pronation at $t/\tau = 4/8$, this "reversed" velocity distribution exhibits a decreased force contribution near the wing root when compared to the 100% feathering simulation.

6.2.3 Pressure Distribution and Wake Structures. The change in spanwise force distribution with increased feathering variation has a direct connection to the pressure distribution along the wing surface and the wake structures produced by the unsteady aerodynamic phenomena. One example of this connection may be seen by comparing the spanwise force distribution at pronation, $t/\tau = 4/8$, in Figure 52 to the vortical wake structures and pressure distribution along the wing surface at pronation shown in Figure 56 for the 3-term kinematic profile.

Contrasting the spanwise force distribution of the 0% feathering wing with the 100% feathering wing, the inboard portion of the 0% feathering wing produces significantly smaller force contribution than the 100% feathering wing during the translational phase of motion, and a "reversed" force contribution during the peak feathering rotation at the end of the half-stroke. Examining Figure 56, the two feathering profiles produce different types of wake structures near the wing root during the feathering rotation at $t/\tau = 4/8$. The vortical structure produced by the 0% feathering wing, or rigid wing, wraps around the wing root to influence both the "upper" and "lower" wing surface. The 100% feathering wing profile does not produce a significant vortical structure at the wing root, rather there is a vortical structure that starts at the trailing edge of the wing and extends into the flowfield during the half-stroke. This vortical structure shed by the 100% feathering wing "connects" with the vortical structure shed from the wing tip, forming a ring type structure at the end of the half-stroke.

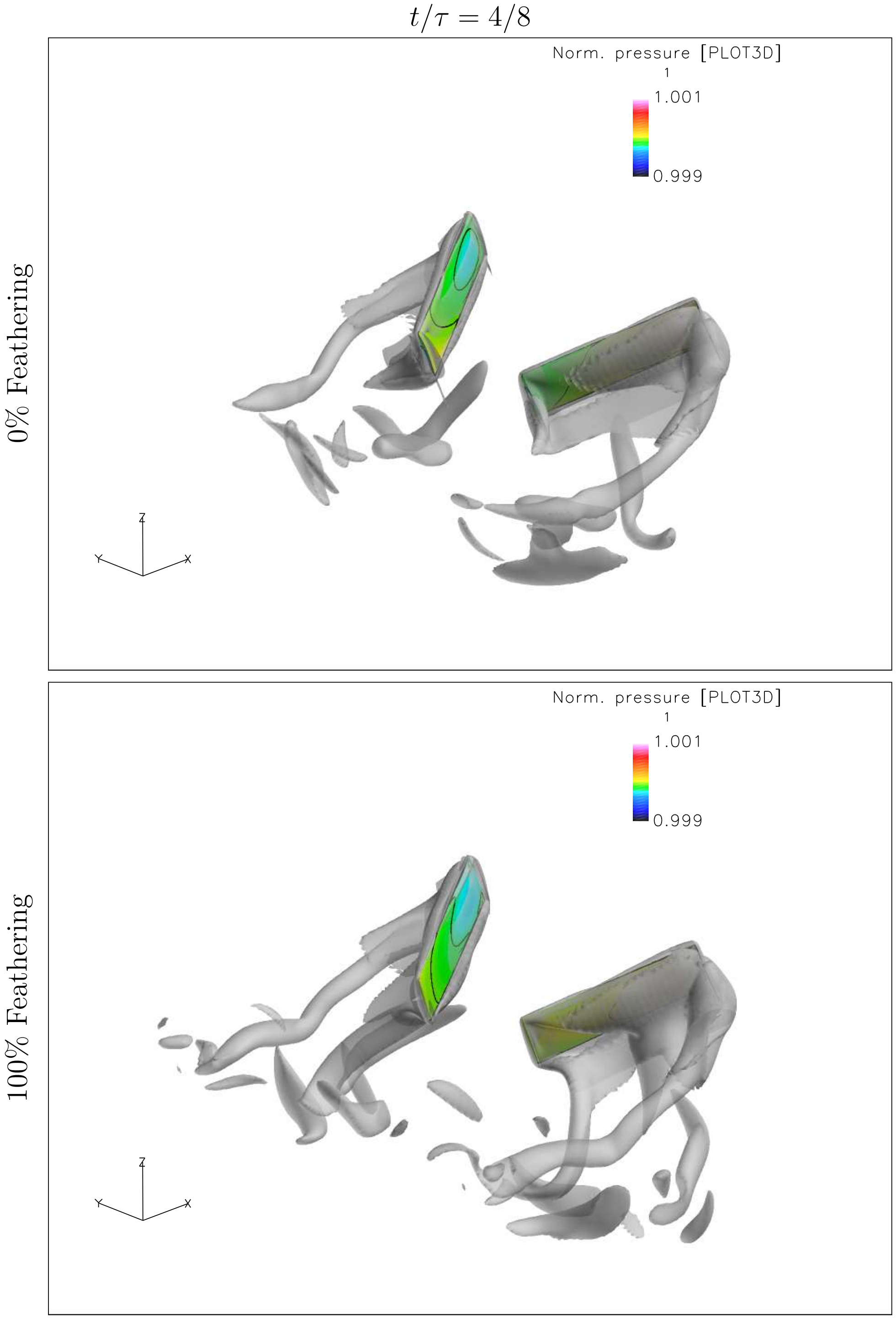

Figure 56: Iso-surface of vorticity magnitude for the 0% and 100% Feathering simulations based on the 3-term kinematic profiles shown during pronation.

This structure then interacts with the “starting” and “stopping” vortical structures shed from the trailing edge of the wing as the wing changes direction of motion at the end of each half-stroke [16]. Components of these structures may be identified in the wake of the 0% feathering profile. However, the vortical structures produced by the rigid wing do not exhibit the same continuous vortical structures as those produced by the 100% feathering wing.

The influence of the altered wake structures on the pressure distribution may be seen in the mean pressure distribution computed during the upstroke and downstroke shown in Figures 57 and 58 for the 0% and 100% feathering profiles. Each figure shows two wing pairs. The wing pair on the right side of the figure represents the mean pressure coefficients computed over the duration of the upstroke, and the wing pair on the left side represents the mean pressure coefficient computed over the duration of the downstroke. The wing pairs are oriented as they would be at the end of their respective half-strokes. Because the end of each half-stroke occurs during the feathering rotation, the point of view shows the “upper” wing surface in the near-field and the “lower” wing surface in the far-field.

Contrasting the mean pressure coefficients for the 0% and 100% feathering simulations, the rigid wings produce a significant region of low pressure, or negative pressure coefficient, on the “lower” wing surface during the upstroke, as seen by the green region on the “lower” wing surface in Figure 57. This is accompanied by a similar, but smaller, region of low pressure on the “lower” wing surface during the downstroke. Neither the upstroke or the downstroke of the 100% feathering case exhibit these regions of low pressure on the lower wing surface, shown in Figure 58.

The larger region of reduced pressure on the lower wing surface during the upstroke corresponds to the longer delay between the start of the upstroke and the peak aerodynamic force magnitude than observed during the downstroke for the rigid wing simulation in Figure 50.

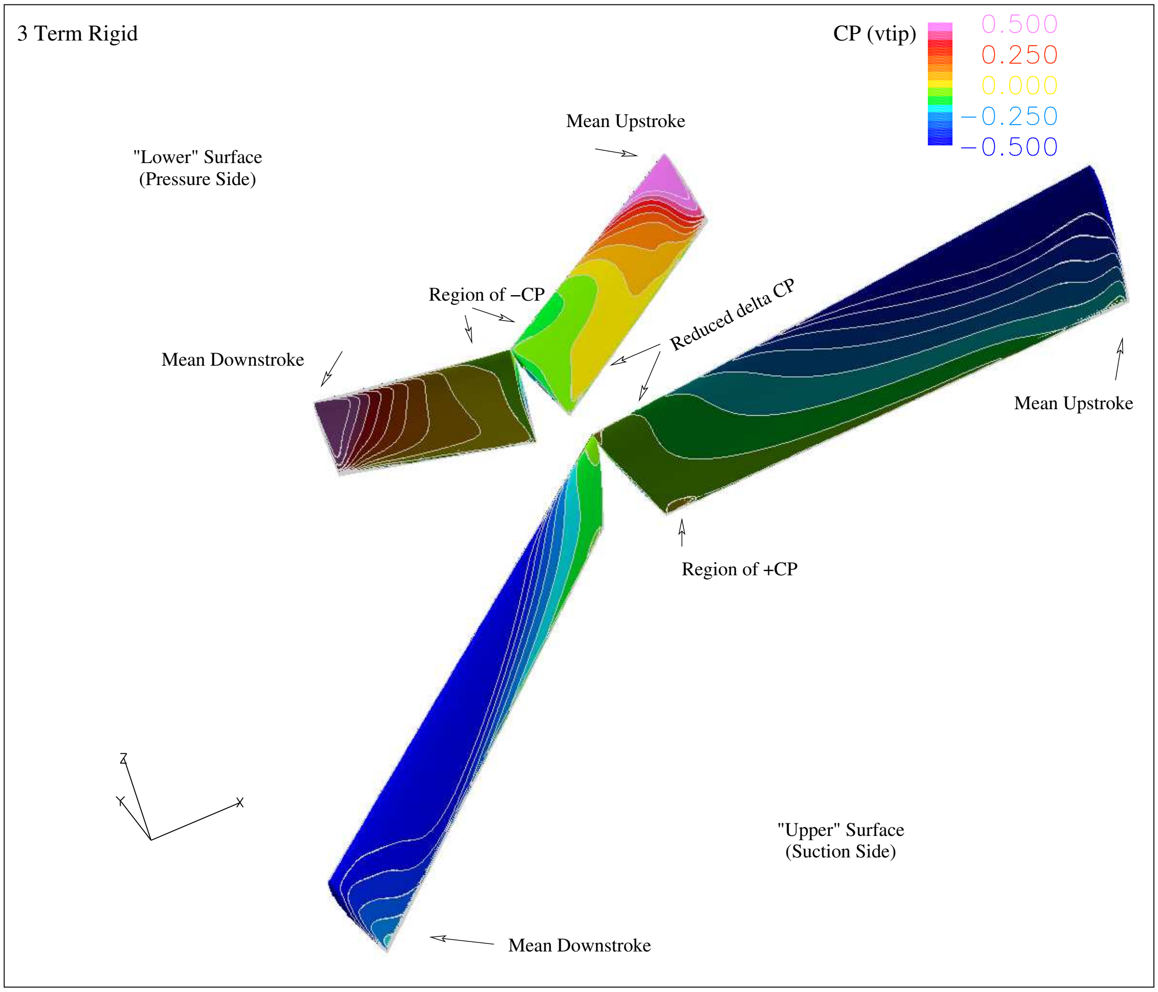

Figure 57: Mean preasure coefficients on the wing surface, 3-term kinematic profile, rigid wing solution.

Along with the influence of the feathering variation on the “lower” wing surface pressures during each half-stroke, there is a corresponding smaller, but still significant, influence on the “upper” wing surface pressures. The mean pressure distribution along the “upper” wing surface varies near the wing root and near the trailing edge of the wing between the 0% and 100% feathering simulations. These regions are influenced by the change in feathering orientation, and by the interaction of the unsteady aerodynamic phenomena.

A similar correlation between the wake structures, Figure 59, and the mean pressure coefficients, shown in Figures 60 and 61, holds for the 4-term kinematic

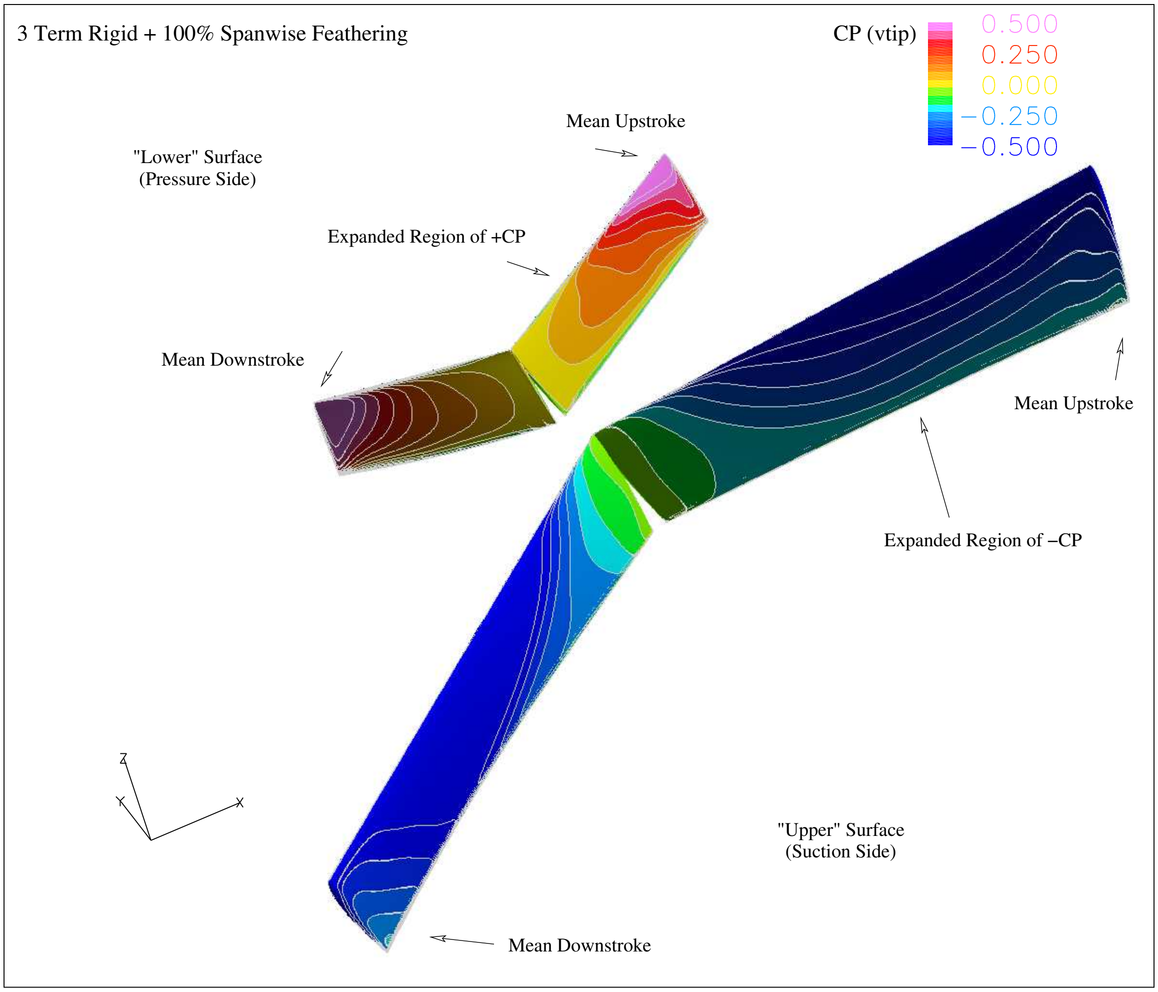

Figure 58: Mean preasure coefficients on the wing surface, 3-term kinematic profile, 100% feathering solution.

profile as was described for the 3-term kinematic profile. The rigid wing exhibits regions of negative pressure coefficient on the"lower" wing surface near the wing root, with a bias in the influence on the upstroke compared to the downstroke. This matches with the variation in the vortical wake structures observed between the 0% and 100% feathering cases for the 4-term kinematic profile in Figures 62 and 63.

6.2.4 Wake Velocities and the Momentum Jet. The vortical wake structures produced by the dynamic wing motions are continually evolving in both space and time. Dominant flow features, such as the leading edge vortex and tip vortex, may be identified and tracked in order to compare the wake structures produced by different wing kinematics of feathering profiles, but these dominant wake structures do not provide much insight into the strength or directionality of the induced momentum jet produced by the dynamic wing motion.

Examining the mean velocity field computed over a complete flapping cycle highlights the strength, directionality, and "coherence" of the vertical momentum jet produced by the hover kinematics. Examining the velocity field for the 4-term kinematic profile shown in Figures 64 and 65, the wake structures produced near the wing root by the rigid wing introduce perturbations in u and v that decrease the "coherence" of the wake structures as they evolve in time compared to the 100% feathering solution. These perturbations influence the strength and direction of the induced momentum jet, which influences aerodynamic performance.

6.3 Change in the Phase Relationship Between the Aerodynamic Forces and Kinematic Parameters

The change in force history with increasing feathering variation alters the phase relationship between the aerodynamic forces and the underlying kinematic parameters, rates, and accelerations. As discussed in Chapter V, the aerodynamic forces for the 3- and 4-term kinematic profiles are sensitive to the sweep and elevation rates

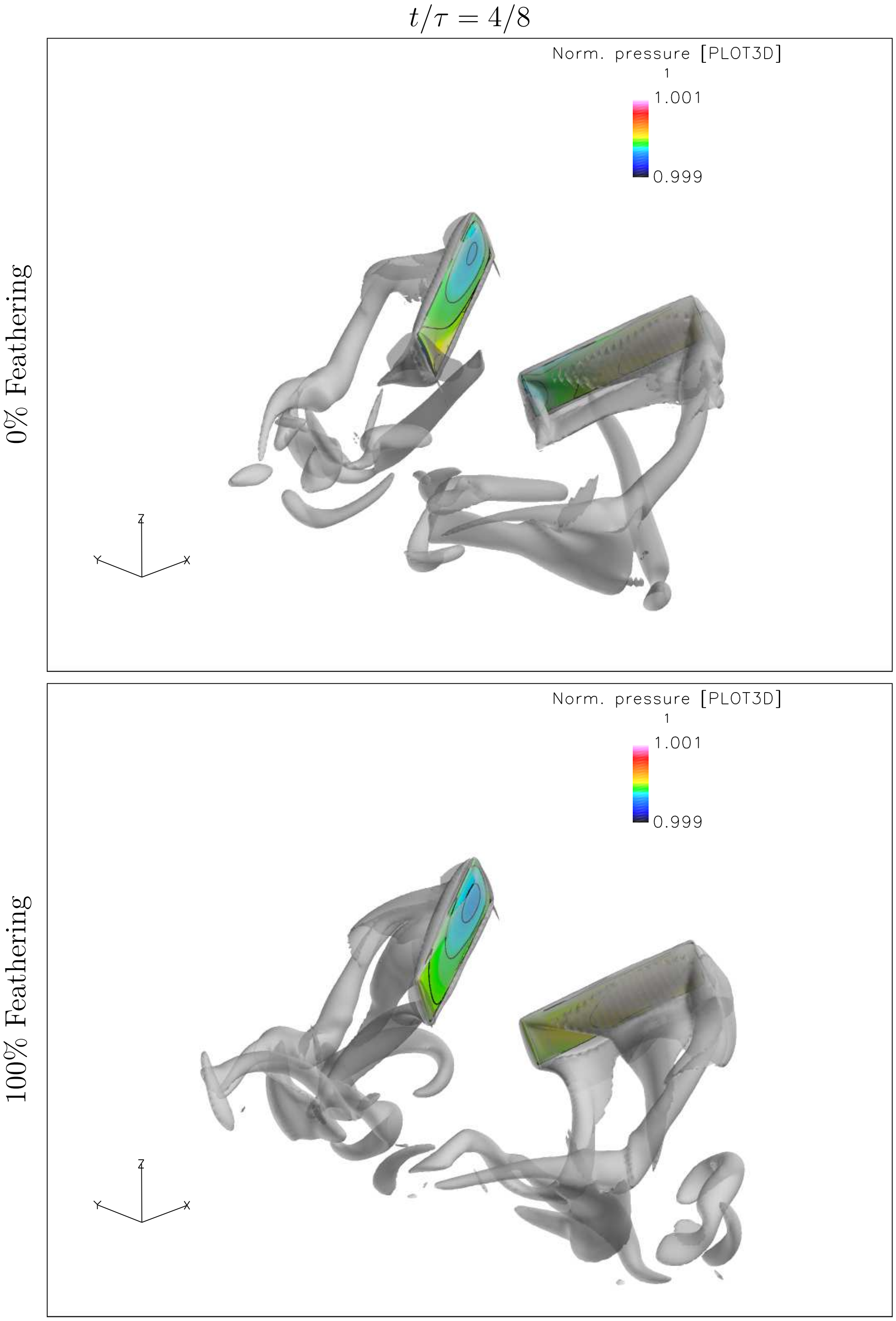

$t/\tau = 4/8$

Figure 59: Iso-surface of vorticity magnitude for the 0% and 100% Feathering simulations based on the 4-term kinematic profiles shown during pronation.

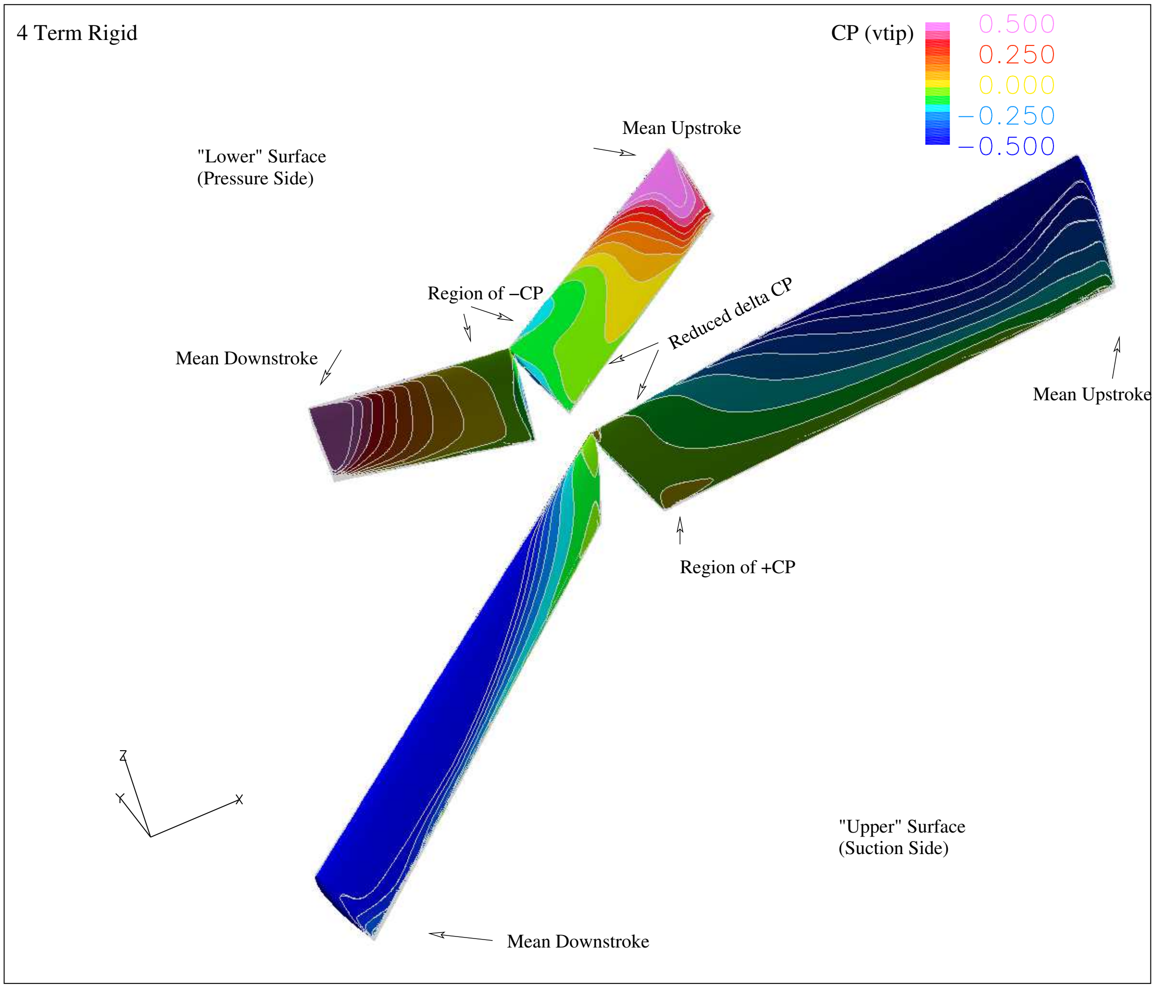

Figure 60: Mean preasure coefficients on the wing surface, 4-term kinematic profile, rigid wing solution.

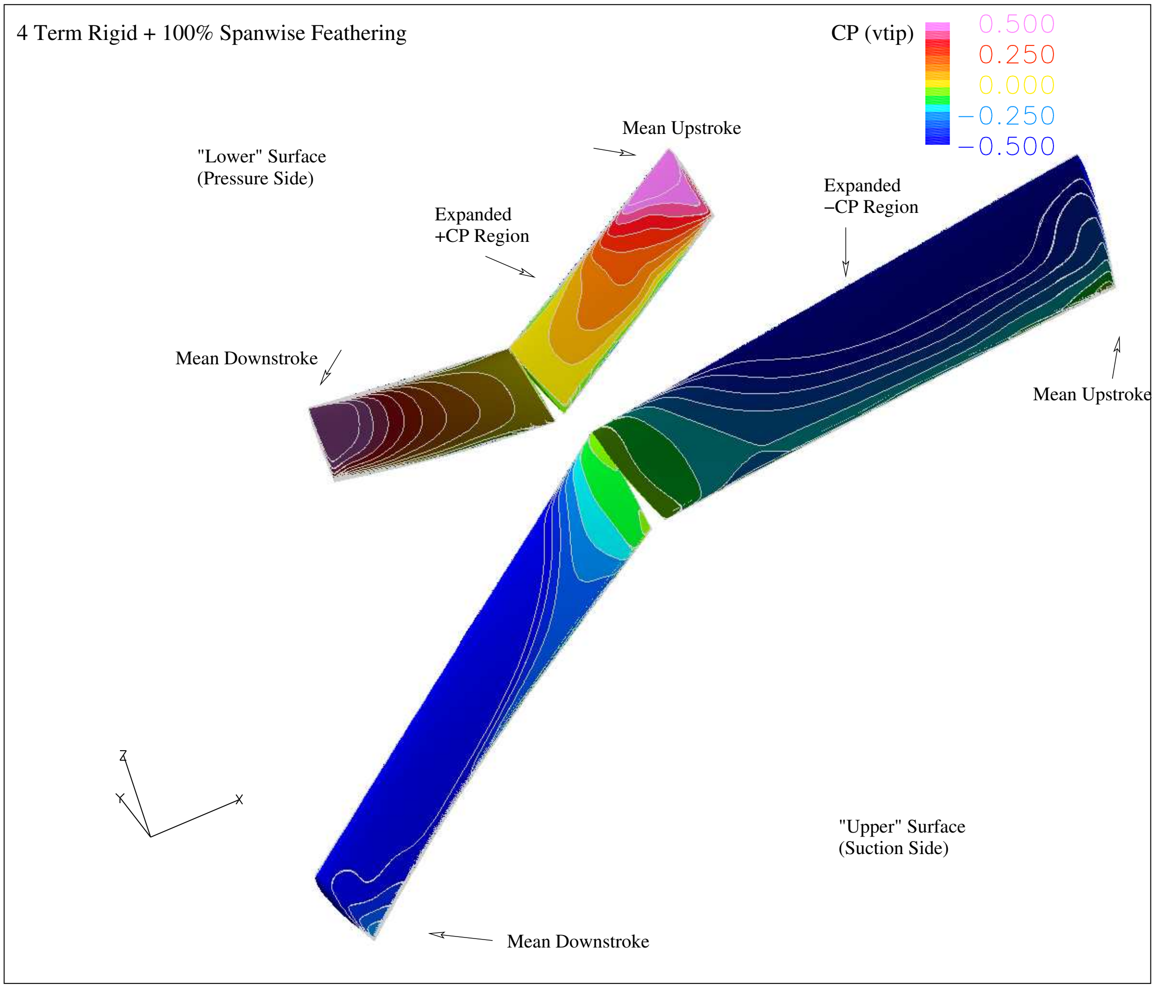

Figure 61: Mean preasure coefficients on the wing surface, 4-term kinematic profile, 100% feathering solution.

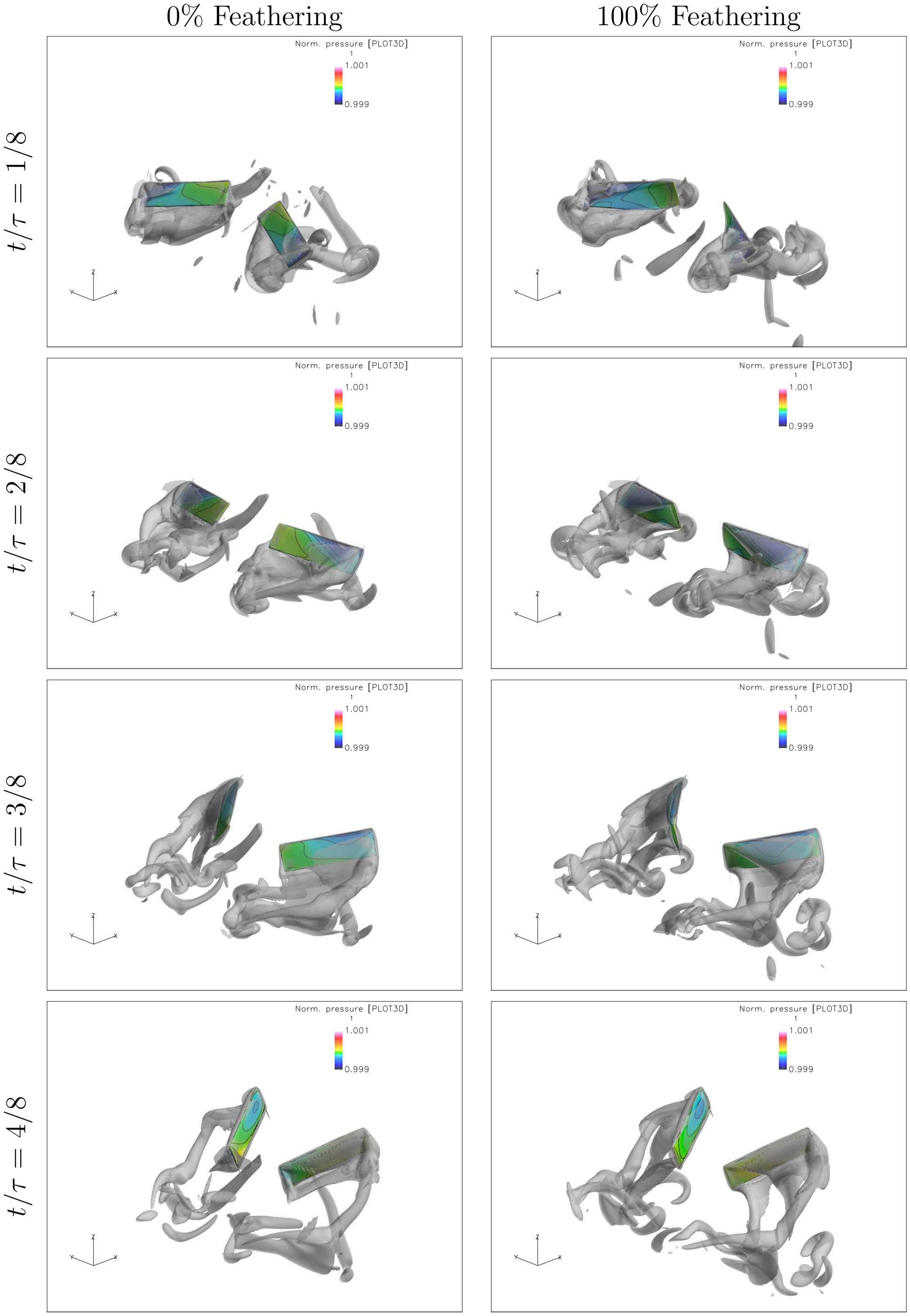

Figure 62: Iso-surface of vorticity magnitude for the 0% and 100% Feathering simulations based on the 4-term kinematic profiles shown during the upstroke.

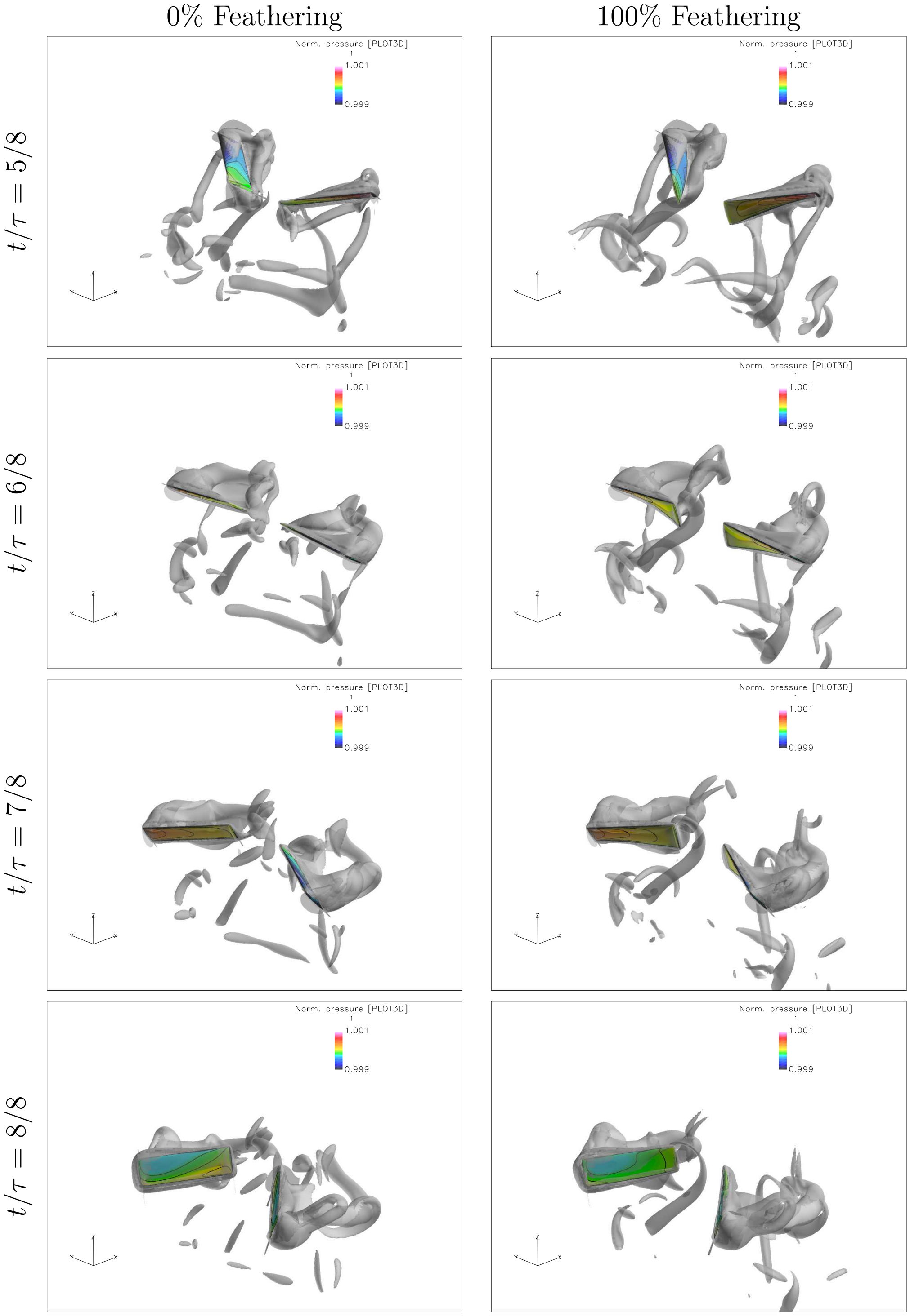

Figure 63: Iso-surface of vorticity magnitude for the 0% and 100% Feathering simulations based on the 4-term kinematic profiles shown during the downstroke.

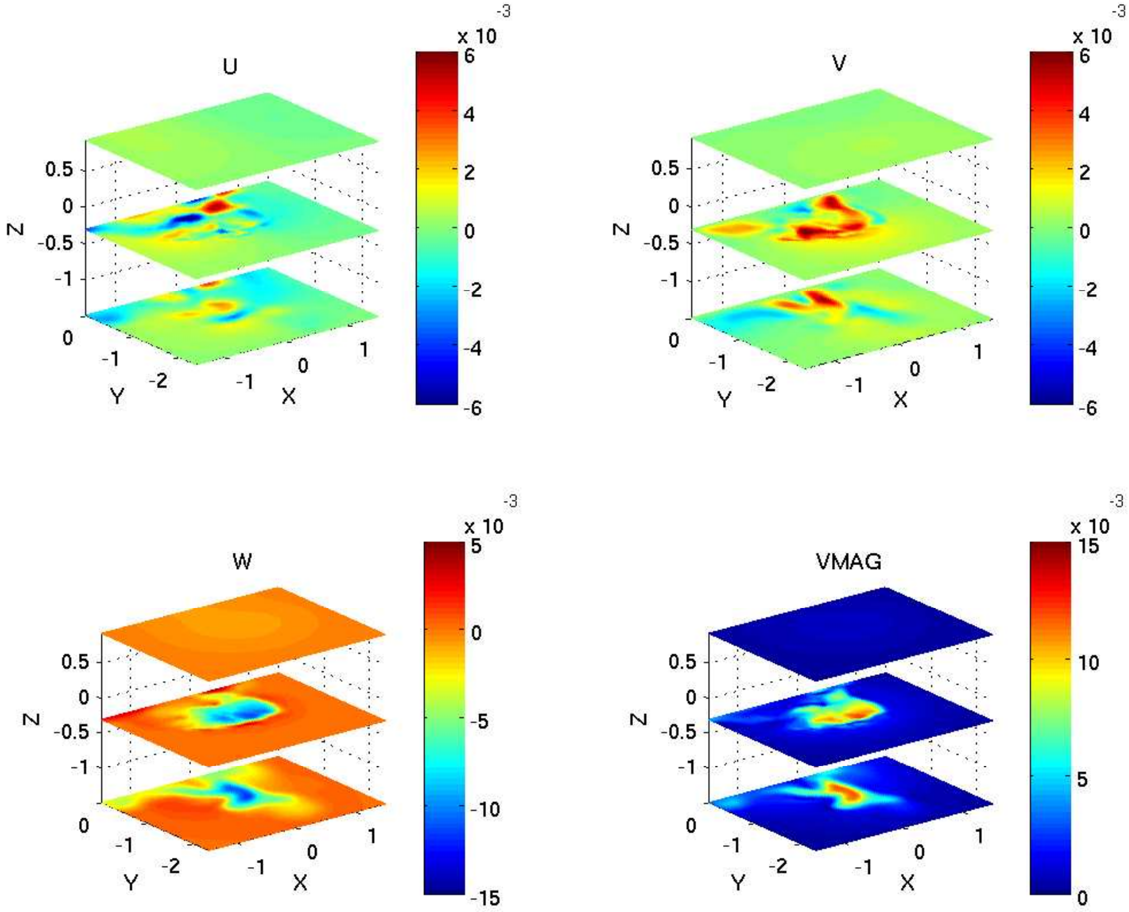

Figure 64: Mean velocity components normalized by tip velocity for the 4-term rigid wing simulation. The three xy-planes are above, immediately below, and below the stroke-plane. The vertical momentum jet can be seen in the plots of the w-velocity component and the velocity magnitude.

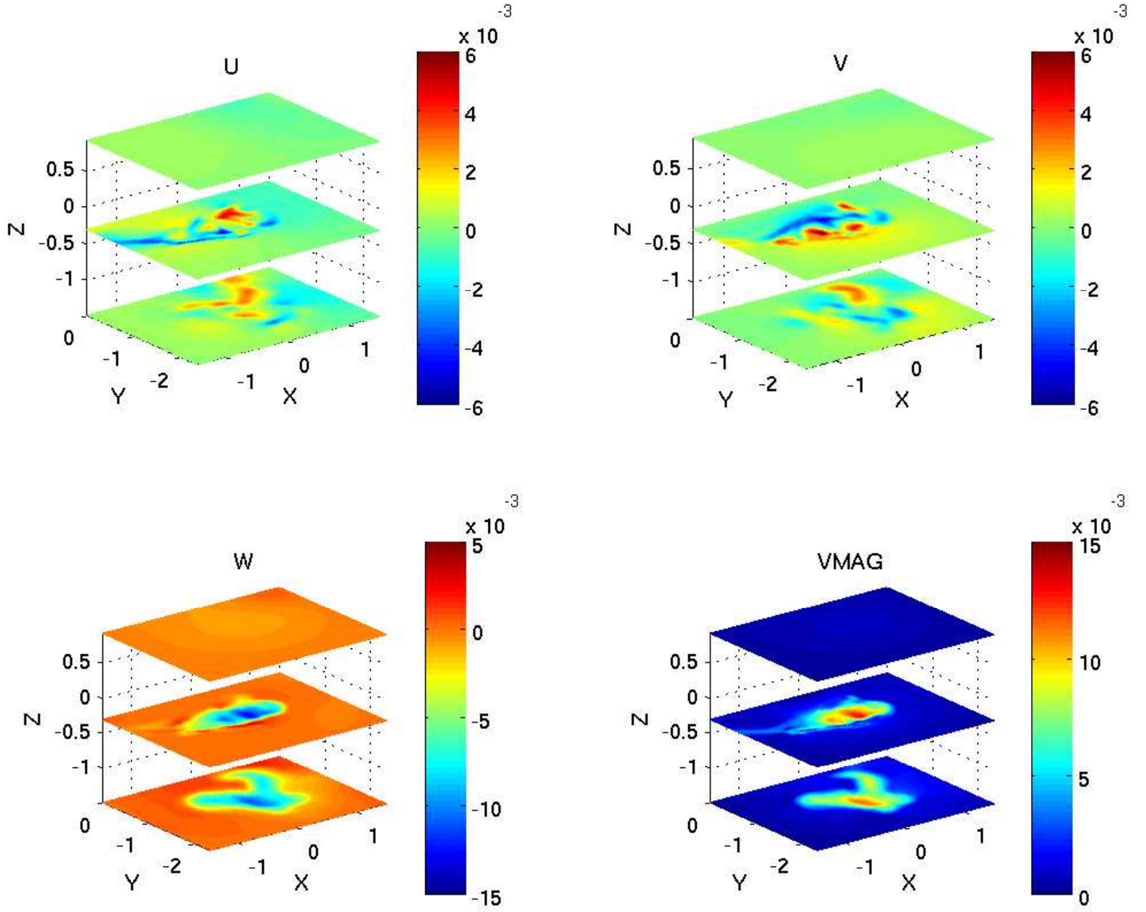

Figure 65: Mean velocity components normalized by tip velocity for the 4-term rigid wing simulation. The three xy-planes are above, immediately below, and below the stroke-plane. The vertical momentum jet can be seen in the plots of the w-velocity component and the velocity magnitude.

and feathering orientation during the translational phase of motion, and the feathering acceleration during the rotational phase of motion.

Examining the phase relationship for the 4-term kinematic profile shown in Figures 66, 67, and 68, it appears that increasing the feathering variation by decreasing the amplitude of the root feathering profile heightens the “correlation” between the aerodynamic force and some kinematic parameters while reducing the influence of other parameters. However, incorporating the feathering variation does not fundamentally change the phase relationship exhibited by any of the kinematic parameters.

Increasing the feathering variation heightens the phase relationship to sweep rate, elevation rate, and feathering orientation during the translational phase of motion, as can be seen by the sharp peaks in the phase portraits exhibited by the 100% feathering case. This is accompanied by an increase in the sensitivity to feathering acceleration rate for the 100% feathering case during pronation and supination. One surprise influence is the heightened sensitivity of the aerodynamic forces to the elevation parameter, shown in Figure 66, and elevation acceleration, shown in Figure 68. The increase in duration of the aerodynamic force magnitude caused by the earlier rise in forces during the half-stroke alters the phase relationship between the sweep parameter, elevation rate, feathering rate, and sweep acceleration as the feathering variation increases.

6.4 Influence on Aerodynamic Performance

Comparing the simulations on the basis of aerodynamic efficiency, the performance metrics show that the 3-term kinematic profile, Table 4, was the most efficient, followed closely by the 4-term kinematic profile, Table 5. Comparing the simulations on the basis of aerodynamic power requirements, the 3-term rigid wing simulation required the least amount of aerodynamic power, requiring 37% less aerodynamic power than the 4-term 100% feathering simulation.

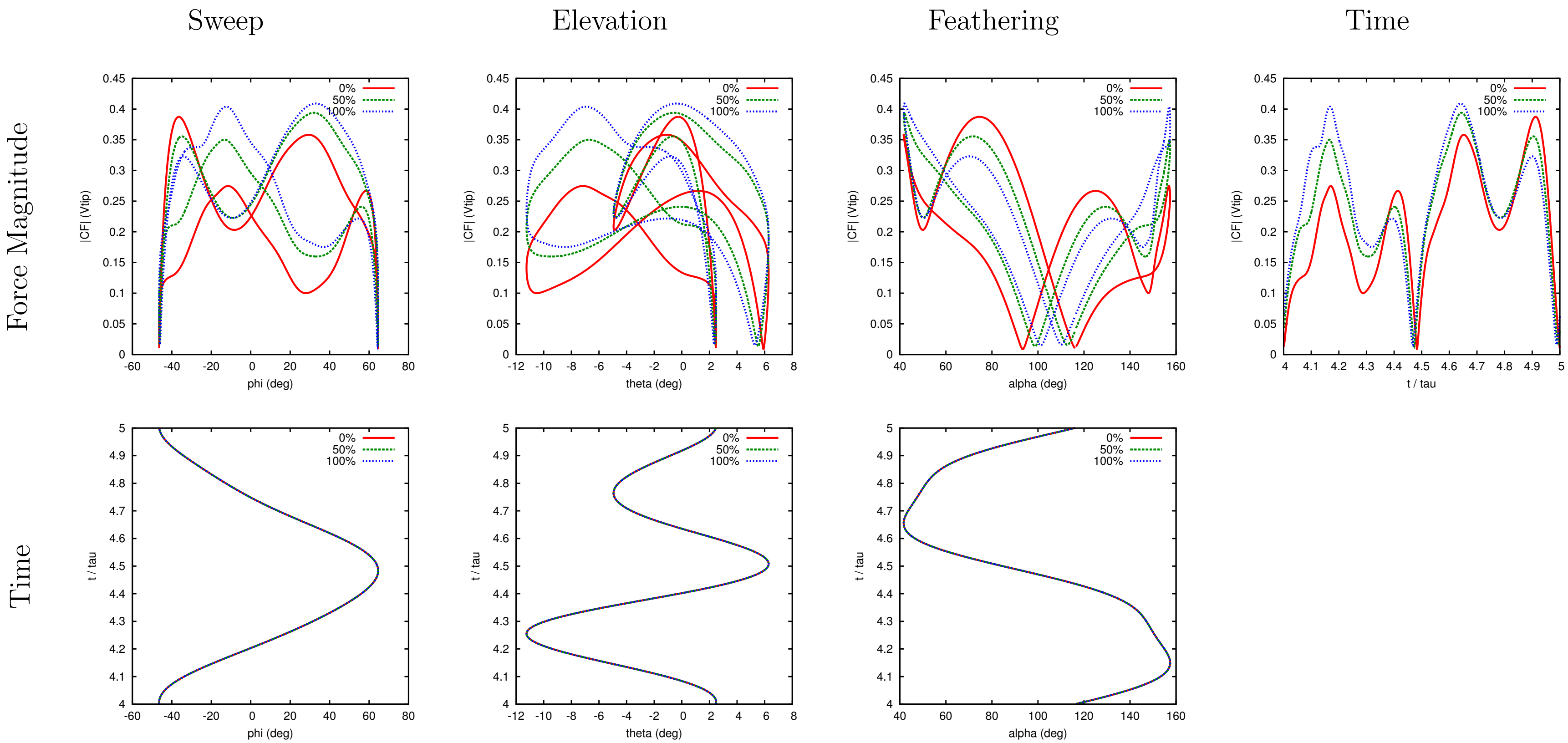

Figure 66: Aerodynamic force magnitude as a function of kinematic parameter for a rigid wing, 0%, half amplitude root feathering profile, 50%, and a fixed root feathering orientation, 100%, based on the 4-term kinematic profile.

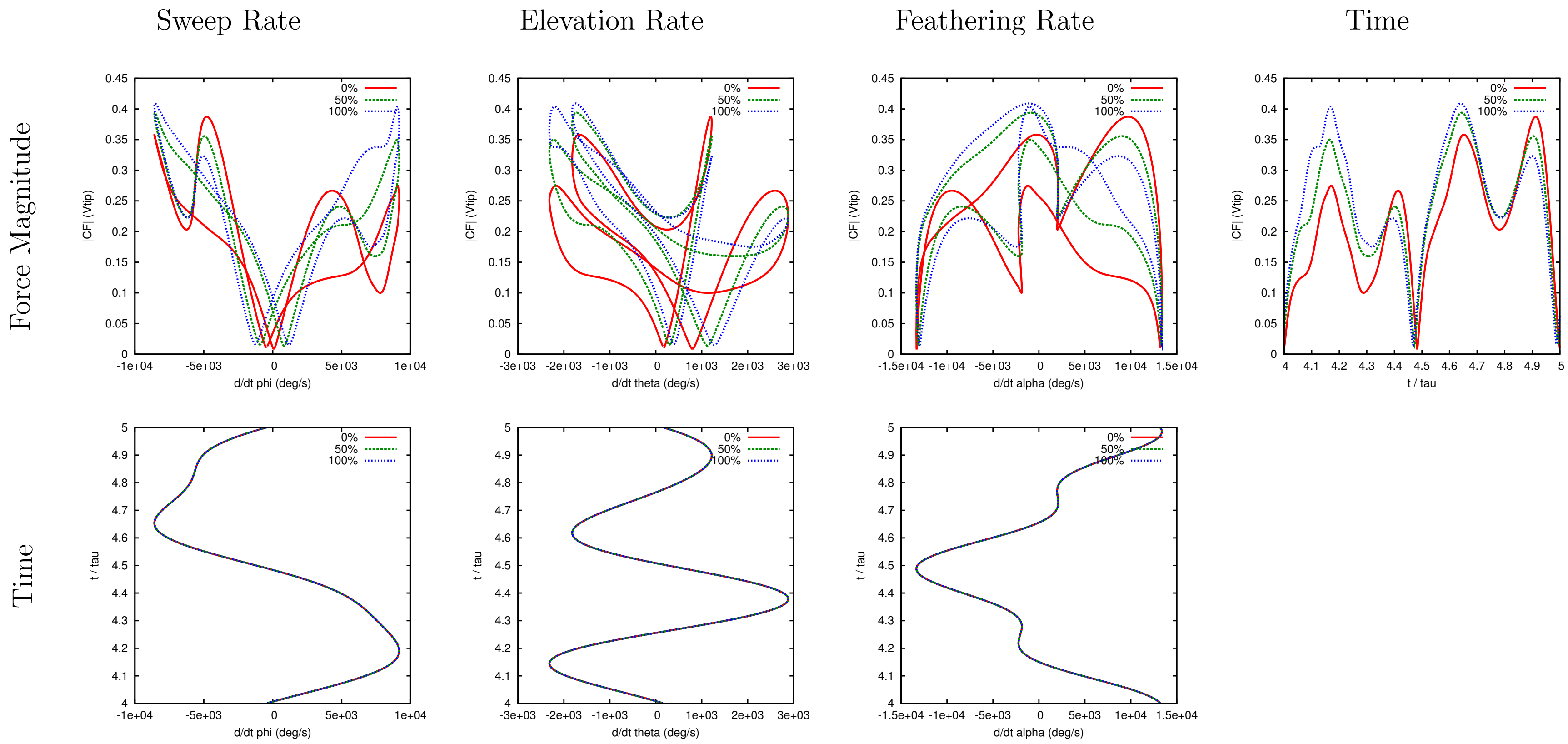

Figure 67: Aerodynamic force magnitude as a function of kinematic rate for a rigid wing, 0%, half amplitude root feathering profile, 50%, and a fixed root feathering orientation, 100%, based on the 4-term kinematic profile.

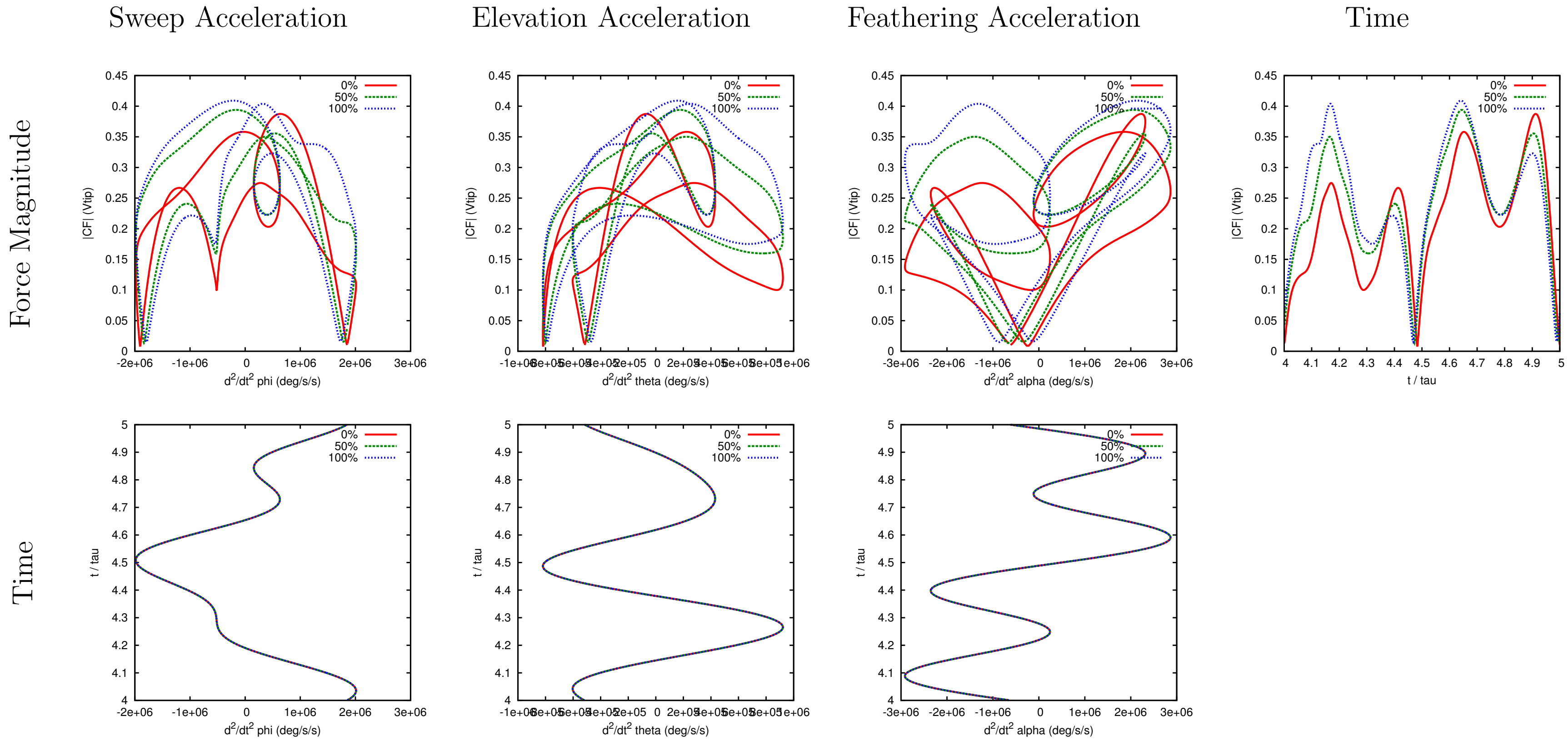

Figure 68: Aerodynamic force magnitude as a function of kinematic acceleration for a rigid wing, 0%, half amplitude root feathering profile, 50%, and a fixed root feathering orientation, 100%, based on the 4-term kinematic profile.

Within the 3-term and 4-term kinematic profiles, the solution computed for a root feathering amplitude of 50% of the wing tip feathering amplitude generated the most vertical force and was the most efficient within a given kinematic profile.

In addition to peak vertical force and power requirements, the solutions with prescribed feathering variations produce significantly smaller mean aerodynamic forces in the side and fore-aft directions, the y- and x-directions respectively. The reduction in mean fore-aft forces ranged from a factor of 2 to a factor of 65, and the reduction in mean side forces ranged from a factor of 2 to a factor of 100, which has significant implications for future work in guidance and control of engineered flapping wing fliers.

Table 4: Computed aerodynamic forces, moments, and power for prescribed feathering variation using the 3-term kinematic profile

	0% Feathering	50% Feathering	100% Feathering
CFx	1.164×10^{-02}	3.638×10^{-03}	1.779×10^{-04}
CFy	-2.919×10^{-02}	-1.624×10^{-02}	-2.840×10^{-04}
CFz	1.136×10^{-01}	1.249×10^{-01}	1.210×10^{-01}
CMx	-7.325×10^{-02}	-7.607×10^{-02}	-7.390×10^{-02}
CMy	-1.387×10^{-02}	-1.280×10^{-02}	-1.086×10^{-02}
CMz	6.108×10^{-03}	4.000×10^{-03}	4.941×10^{-03}
CP	6.755×10^{-02}	7.229×10^{-02}	7.751×10^{-02}
η_{aero}	$1.681\times10^{+00}$	$1.728\times10^{+00}$	$1.562\times10^{+00}$

Table 5: Computed aerodynamic forces, moments, and power for prescribed feathering variation using the 4-term kinematic profile

	0% Feathering	50% Feathering	100% Feathering
CFx	1.418×10^{-02}	5.116×10^{-03}	-3.927×10^{-03}
CFy	-2.970×10^{-02}	-1.147×10^{-02}	4.607×10^{-03}
CFz	1.352×10^{-01}	1.506×10^{-01}	1.445×10^{-01}
CMx	-8.513×10^{-02}	-8.921×10^{-02}	-8.582×10^{-02}
CMy	-1.710×10^{-02}	-1.490×10^{-02}	-1.043×10^{-02}
CMz	1.126×10^{-02}	9.512×10^{-03}	5.743×10^{-03}
CP	8.360×10^{-02}	9.010×10^{-02}	9.640×10^{-02}
η_{aero}	$1.617\times10^{+00}$	$1.672\times10^{+00}$	$1.499\times10^{+00}$

6.5 Summary

The spanwise feathering variation influences the orientation of the wing surface and the velocity and acceleration profiles of the wing associated with the feathering rotation. This spanwise variation in the kinematic profile influences the local unsteady aerodynamic phenomena, which in turn influences the overall aerodynamic performance.

In the case of a rigid wing, the feathering rotation at the wing root induces a non-circulatory aerodynamic phenomenon that produces a region of low pressure on the “lower wing surface” and a localized set of vortical flow structures near the wing root during pronation and supination. At the same point in the wing stroke, the combination of circulatory and non-circulatory aerodynamic phenomena at the wing tip produce a region of high pressure on the “lower” wing surface and a localized region of low pressure on the “upper” wing surface. This “reversed” force distribution decreases the net aerodynamic forces produced by the wing during the rotational phase of motion. The localized vortical structures at the wing root and the associated region of low pressure convect below the wing as the wing changes direction of motion. This region of low pressure influences the pressure distribution along the wing surface as the wing sweeps above the vortical structures, reducing the net aerodynamic forces produced early in the wing stroke.

In addition to the direct influence on aerodynamic performance, the local pressure distribution and vortical structures at the wing root of the rigid wing disrupt the formation of the leading edge vortex on the inboard part of the wing after stroke reversal. This may account for discrepancies between early rigid wing simulations and experimental observations of the flexible natural flier regarding the continuity of the leading edge vortex across the body from wing-tip to wing-tip [21, 92].

VII. Analysis of Bending Along the Elastic Axis

As with torsional flexibility, the lack of a good characterization of the Hawkmoth wing structure necessitated the use of assumed bending characteristics rather than the use of a structural model to examine the influence of bending on the unsteady aerodynamic mechanisms. Thus, the discussion of bending influence is presented as a proof-of-concept demonstration and used to identify coupling mechanisms that could influence fluid-structure interactions of interest and identify future research directions.

7.1 Prescribed Bending as a Function of Span and Time

For consistency with the assumed torsion distribution, the first bending mode of a fixed-free beam was used to define the spatial bending distribution. The first bending mode for a fixed-free beam, defined by Equation (28) for the coefficients $a_1 = 1.87510$ and $b_1 = 0.734096$, was scaled by the inertial forces due to the prescribed wing kinematics to approximate the dynamic wing response.

$$\Gamma_B(r) = \cosh\left(a_1 r/R\right) - \cos\left(a_1 r/R\right) - b_1\left(\sinh\left(a_1 r/R\right) - \sin\left(a_1 r/R\right)\right) \tag{28}$$

The time history of bending was determined using the inertial forces acting on the wing during the wing stroke, which depend on the mass distribution of the wing and the kinematic accelerations in sweep, elevation and feathering. By co-locating the elastic axis and prescribed feathering axis at the leading edge of the wing, the influence of the feathering rotation on bending may be neglected. To compute the time-history of the inertial forces, the rotational accelerations due to feathering and elevation defined in the inertial reference frame were transformed into the wing local frame. This transformation provided accelerations normal to the wing surface and in the chordwise direction. Lacking a well-defined mass or stiffness distribution of the Hawkmoth wing, the time history of the accelerations normal to the wing surface and in the chordwise direction were unit normalized and scaled to achieve a reasonable maximum tip deflection. Thus, the local time-dependent wing deformations were defined in space using the first mode of a uniform fixed-free beam and scaled in time by the rotational accelerations associated with the kinematic rotations.

7.2 Results of the Bending with Torsion Simulations

After examining the available footage of the Hawkmoth in flight and considering the smoothing influences of the torsionally flexible wings on the unsteady aerodynamics at the wing root, the bending degree-of-freedom was superimposed onto the 50% torsion simulation described in Chapter VI. By superimposing the bending deformations on the torsionally flexible wing, illustrated in Figure 48, the bending with torsion simulations provide a more realistic representation of the flexible Hawkmoth wing than would be achieved by superimposing the bending deformations onto the rigid wing motion. Two peak tip deflections were considered for each kinematic profile representing 5% and 10% of the wing length. The kinematic accelerations associated with the 3- and 4-term kinematic profiles produce two time-dependent tip paths, shown in Figures 69 and 70.

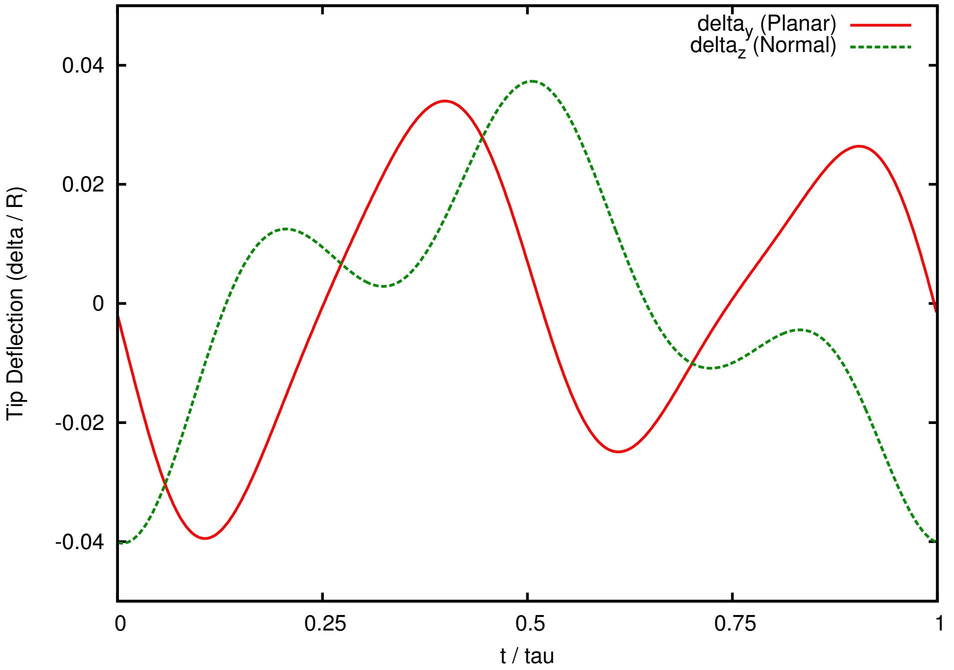

Figure 69: Tip deflection history for the 3-term kinematic profile.

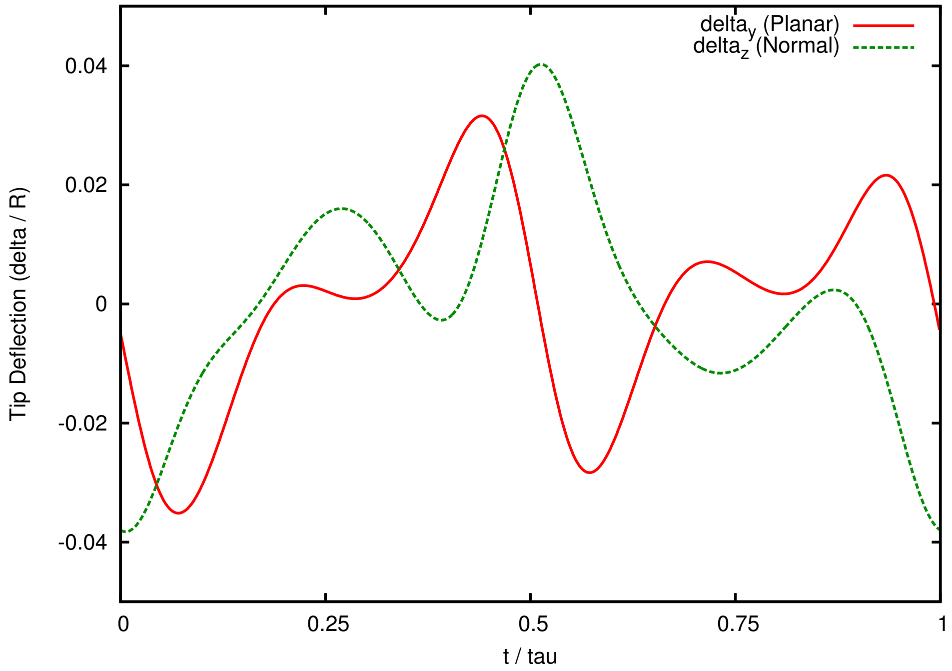

Figure 70: Tip deflection history for the 4-term kinematic profile.

Examination of the force history of the bending solutions based on the 3-term kinematic profile, shown in Figure 71, indicates the inclusion of bending modes increases the force magnitude at the end of each half-stroke while decreasing the force magnitude during the translational phase of motion in the middle of each half stroke. This alters the 3-term force history from a single aerodynamic peak during each half-stroke to a set of double peaks. As would be expected, the increase in the force magnitude at the ends of the wing stroke is strongest for the 10% tip deflection. However, due to the wing orientation at the end of each half-stroke, the increase in force magnitude at the ends of the half-stroke has a greater influence on the y-direction forces than the z-direction due to wing orientation. As would be expected for first mode beam bending, examination of the spanwise force distribution indicates that the largest change in aerodynamic forces occcurs near the wing tip. The increase in the y-direction force is highlighted in Figure 72 at $t/\tau = 8/8$, while the variation in the vertical force is visible in Figure 73. The variation in the tip path due to the bending deformations may also be seen Figure 73 The influence of the tip deflections

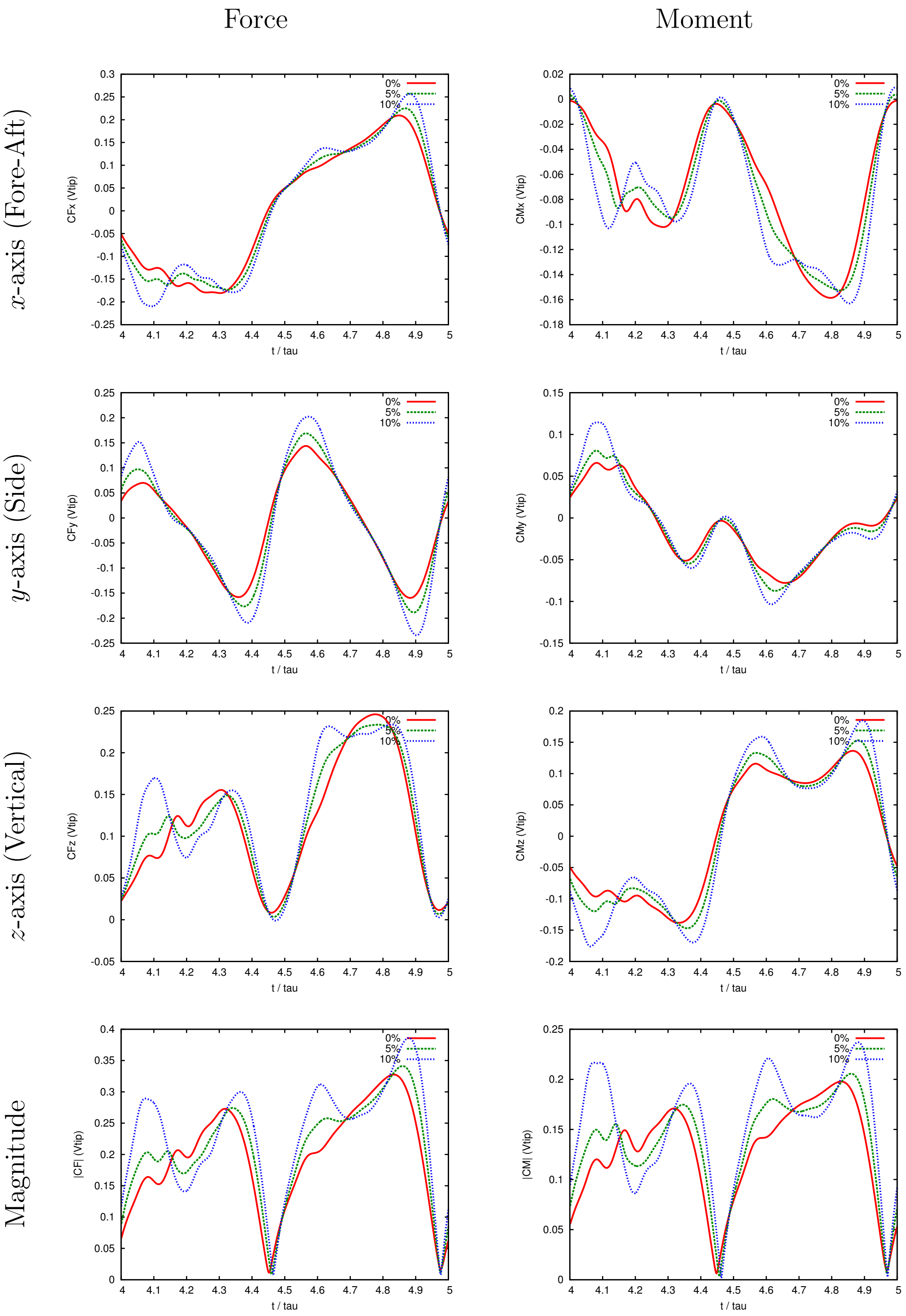

Figure 71: Aerodynamic force and moment histories for the 0%, 5%, and 10% bending simulations using the 3-term kinematic profile. The flier is oriented in a reference system with the x-axis aligned in the aft direction, the z-axis aligned in the vertical direction, and the y-axis aligned with the right wing.

on the unsteady aerodynamic mechanisms produced by the 3-term kinematic profile may be seen as variations in the wake structures at pronation shown in Figure 74.

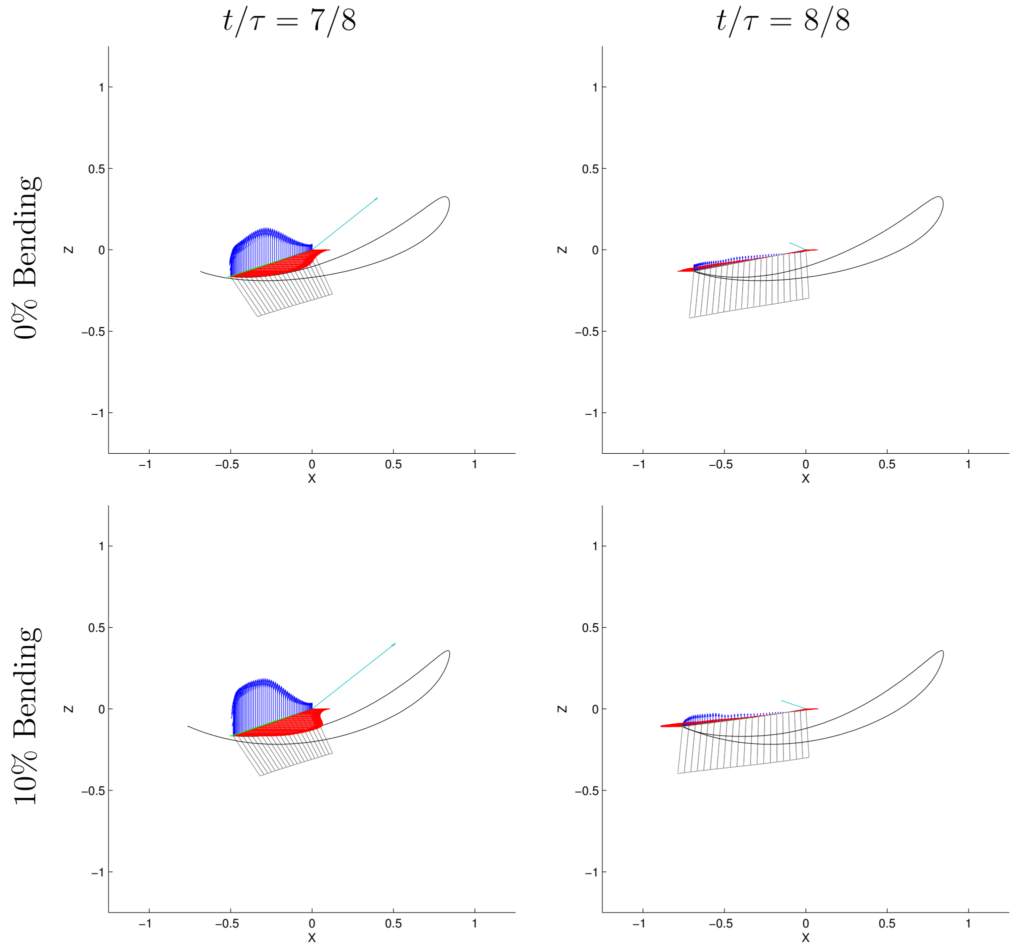

Figure 72: Comparison of the spanwise force distribution for the bending simulations. The three components of the sectional aerodynamic force are shown in red for the x-direction, in green for the y-direction, and in blue for the z-direction. The wing motion is based on the 3-term kinematic profile.

The prescribed bending deformations based on the 4-term kinematic profile influence the force history in a similar manner as the 3-term profile, increasing the force magnitude at the ends of the half-stroke and decreasing the force magnitude during the translational phase of motion, as shown in Figure 75. Unlike the solutions based on the 3-term kinematic profile, the 4-term solutions do not exhibit the same dramatic increase in forces at the begnining the half-stroke; instead the deformations increase the amplitude of the “shoulder” discussed for the 4-term feathering solutions in the

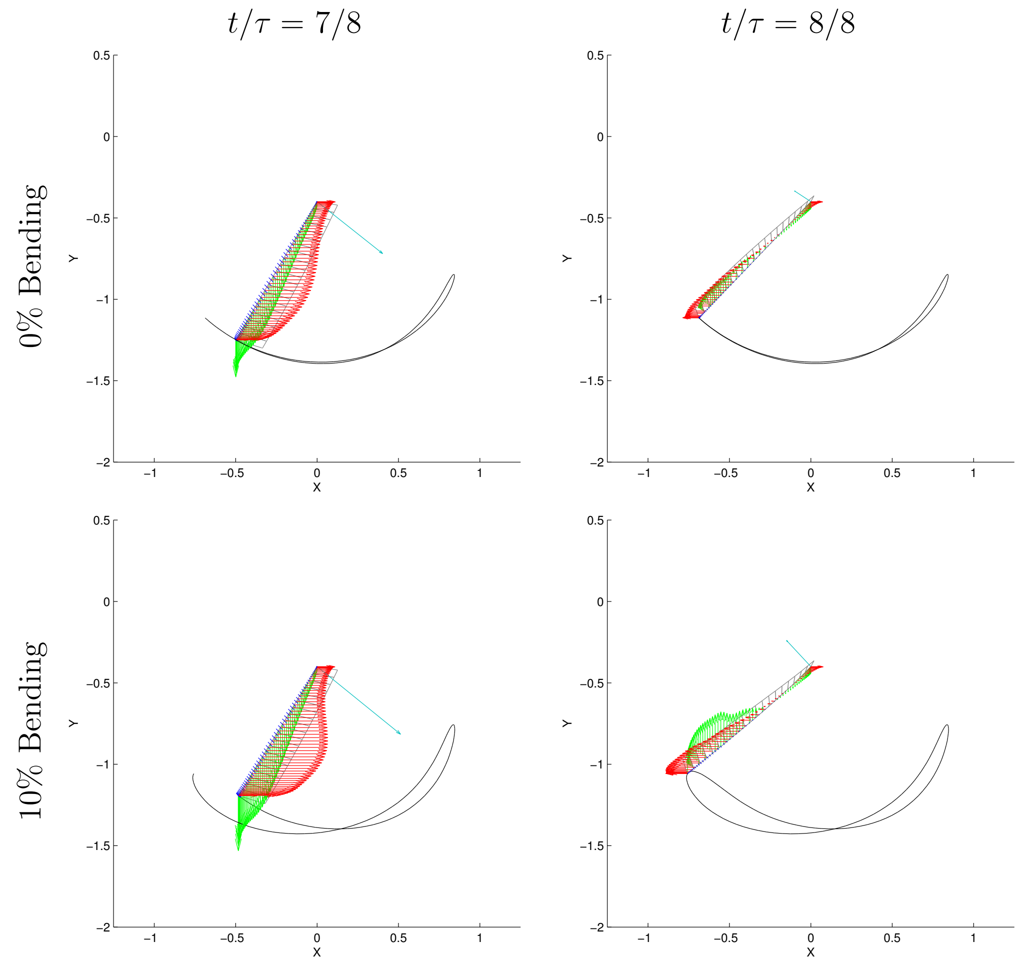

Figure 73: Comparison of the spanwise force distribution for the bending simulations. The three components of the sectional aerodynamic force are shown in red for the x-direction, in green for the y-direction, and in blue for the z-direction. The wing motion is based on the 3-term kinematic profile.

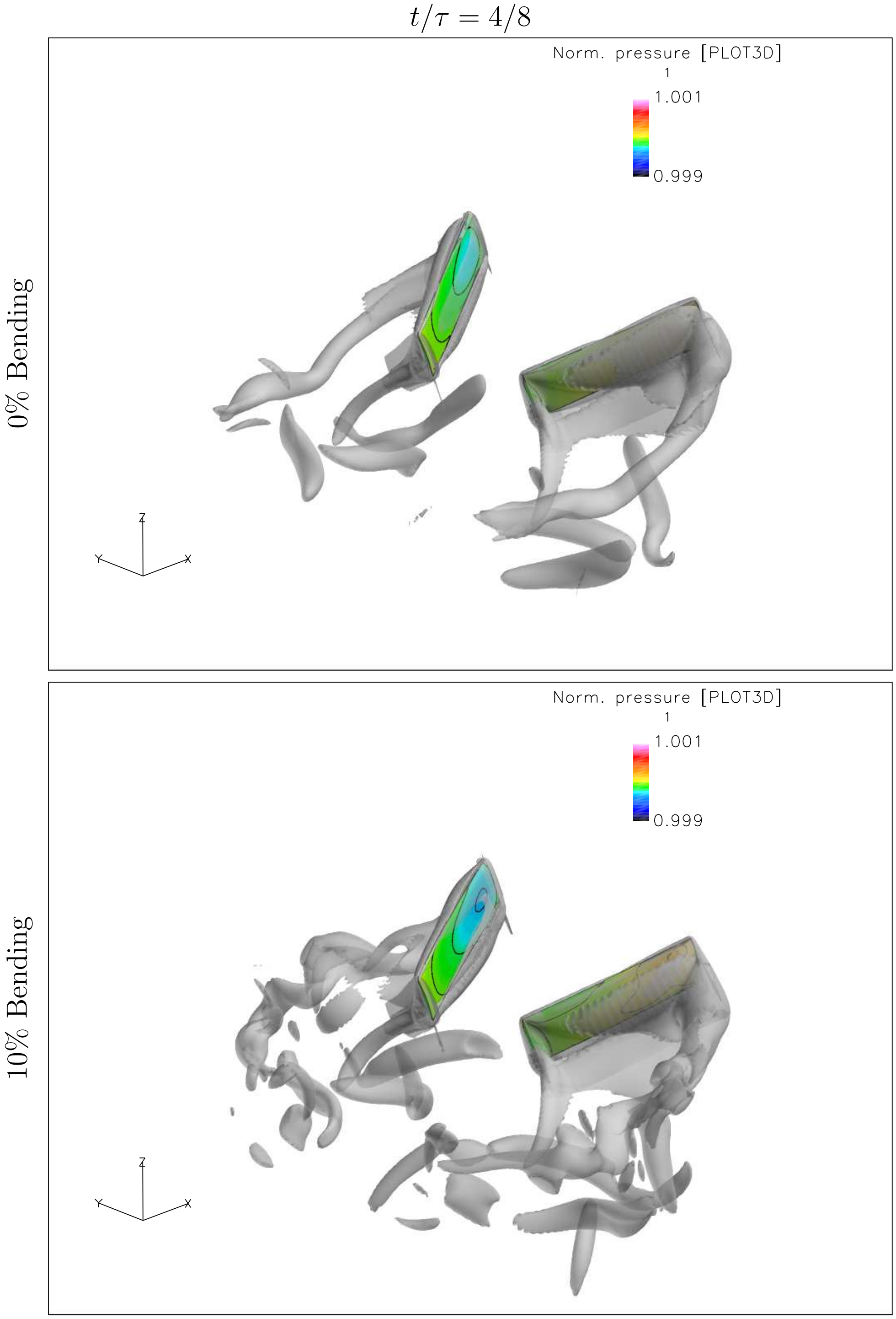

Figure 74: Iso-surface of vorticity magnitude for the 0% and 10% Bending simulations based on the 3-term kinematic profiles shown during pronation.

previous chapter. For the feathering solutions without bending, it was hypothesized that the shoulder in the force history is due to wing-wake interactions, while the early aerodynamic peak exhibited by the 4-term kinematic profile was due to the circulatory aerodynamic mechanisms produced when the peak sweep and elevation rates occur in phase with a maximum feathering orientation. It is a logical extension that the bending deformations influence the wing-wake interactions by increasing the effective tip velocity during this part of the wing stroke. Wing-wake interactions could account for the fluctuation in the tip forces at $t/\tau = 1/8$ and $2/8$ seen in Figures 76 and 77, as well as the variation in the strength and coherency of the tip vortex between the 0% and 10% bending solutions shown in Figure 80.

The response late in the half-stroke of the 4-term kinematic profile is dominated by the large feathering rotation and the non-circulatory aerodynamic mechanisms near the wing root. The dramatic increase in force magnitude late in the half-stroke may be due to non-circulatory mechanisms occurring near the wing tip as the bending deformations alter the effective sweep angle, tip velocity, and tip acceleration. This explanation could account for the variation in the spanwise force distribution seen in Figures 78 and 78 at $t/\tau = 3/8$ and $t/\tau = 4/8$. Examining the wake structures produced by the 0% and 10% bending solutions, the 10% bending solution exhibits a significant vortical structure shed from the trailing edge of the wing at $t/\tau = 4/8$ in Figure 80.

Just as the bending deformations influencing the wing-wake interactions by increasing the tip velocity at the beginning of the half-stroke, the deformations exhibited by the 4-term kinematic profile reduce the translational velocity at the wing tip during the middle of the half-stroke resulting in a further reduction in the force magnitude and the vertical forces shown in Figure 75. The variation in the tip path due to the bending deformations may be seen from different perspectives in spanwise force plots.

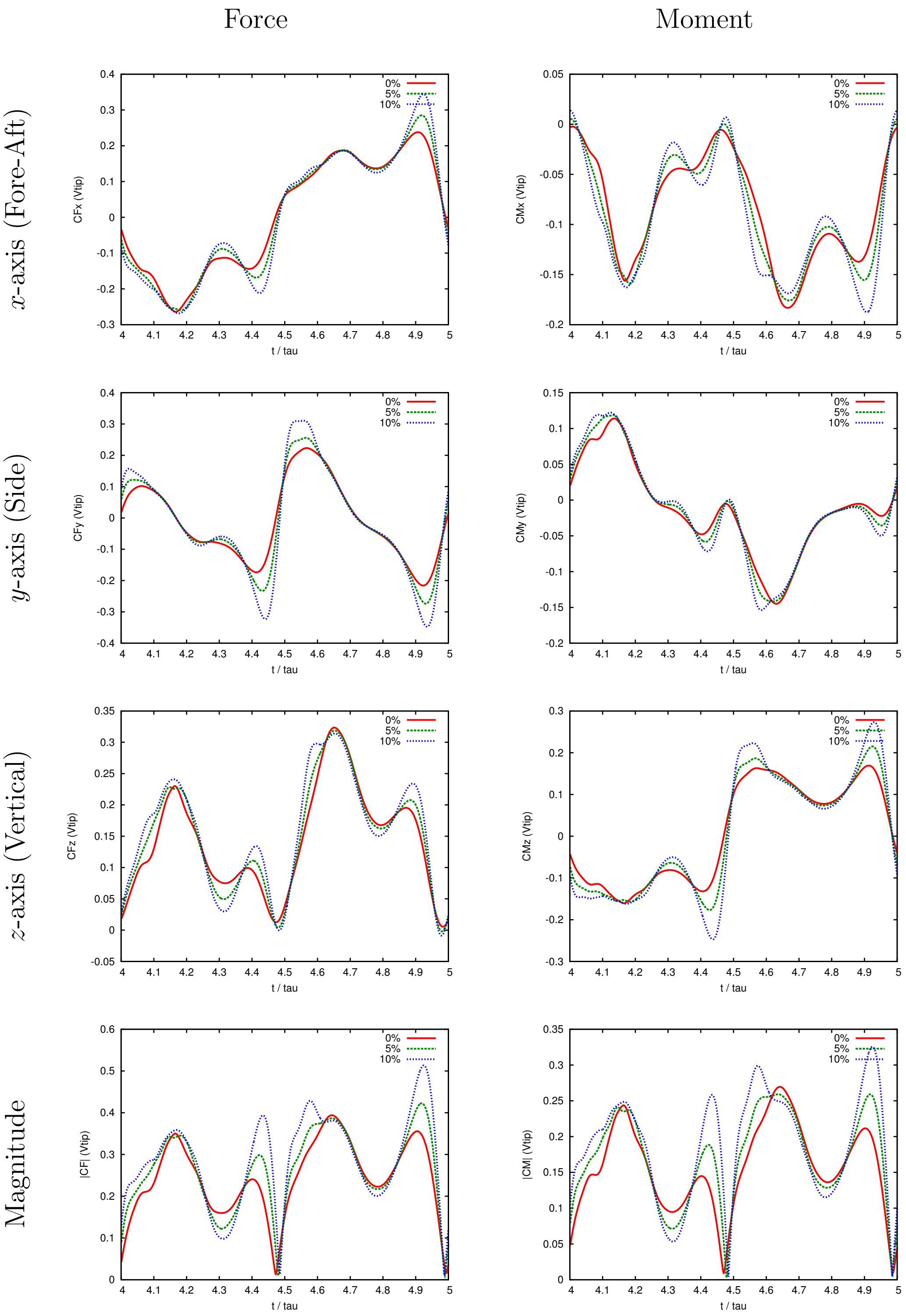

Figure 75: Aerodynamic force and moment histories for the 0%, 5%, and 10% bending simulations using the 4-term kinematic profile. The flier is oriented in a reference system with the x-axis aligned in the aft direction, the z-axis aligned in the vertical direction, and the y-axis aligned with the right wing.

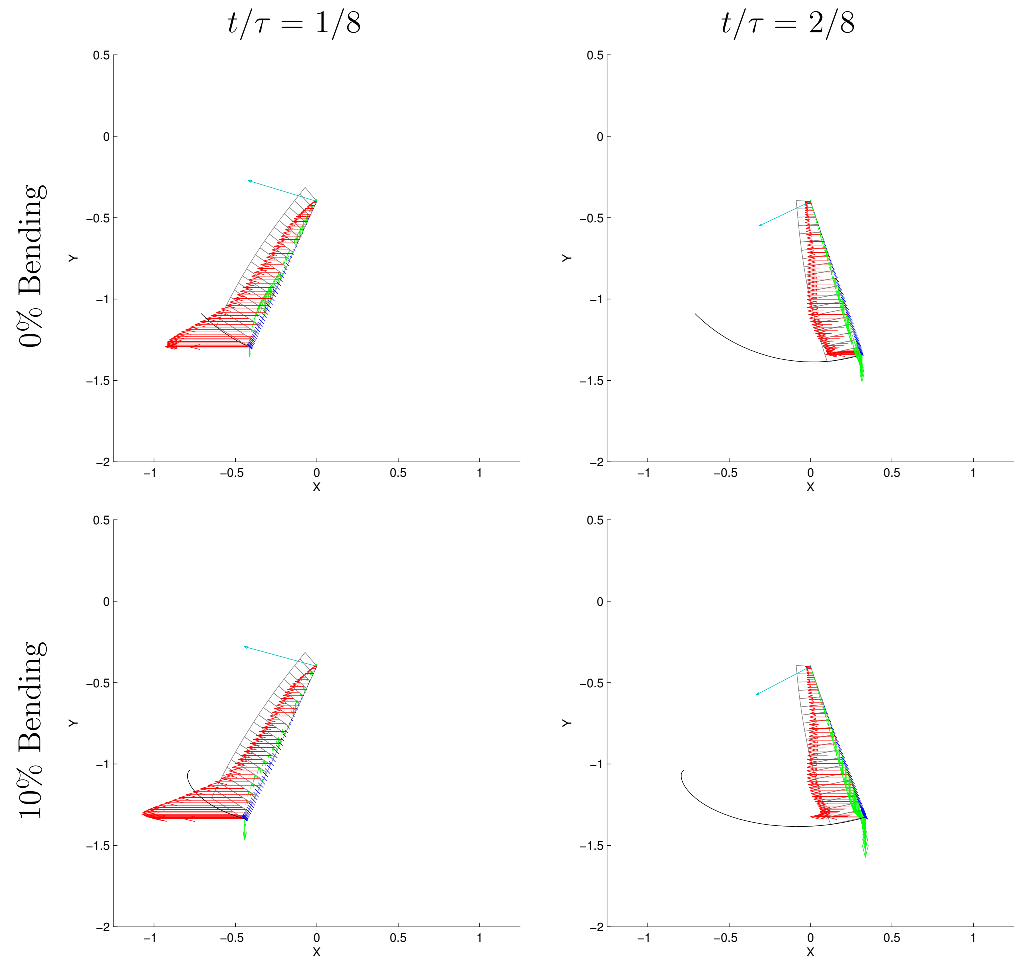

Figure 76: Comparison of the spanwise force distribution for the bending simulations. The three components of the sectional aerodynamic force are shown in red for the x-direction, in green for the y-direction, and in blue for the z-direction. The wing motion is based on the 4-term kinematic profile.

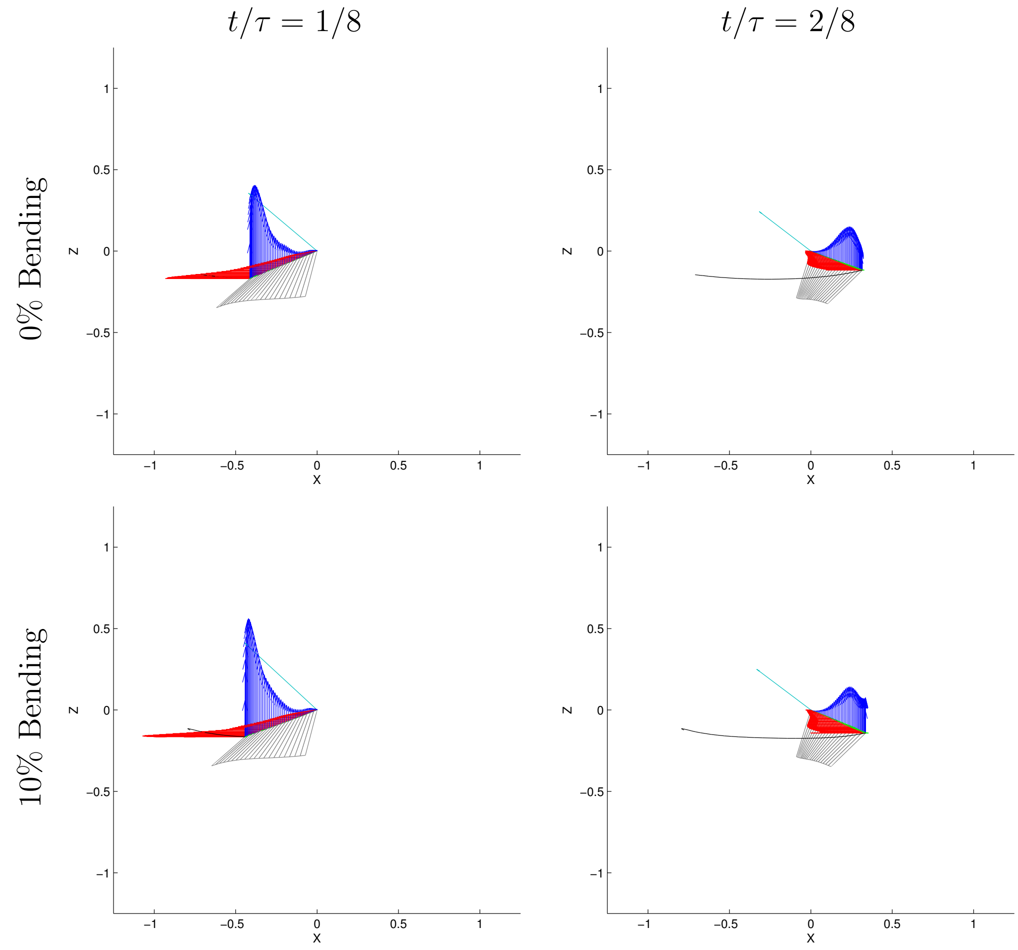

Figure 77: Comparison of the spanwise force distribution for the bending simulations. The three components of the sectional aerodynamic force are shown in red for the x-direction, in green for the y-direction, and in blue for the z-direction. The wing motion is based on the 4-term kinematic profile.

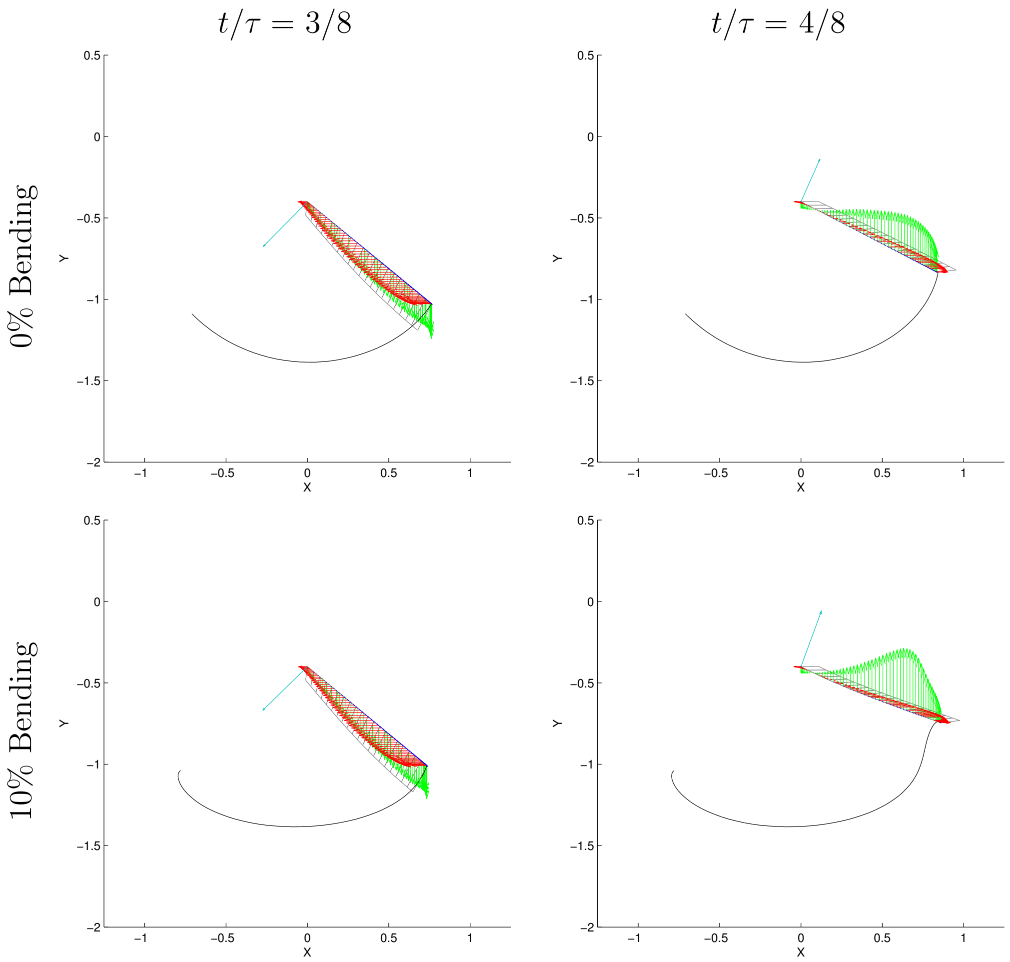

Figure 78: Comparison of the spanwise force distribution for the bending simulations. The three components of the sectional aerodynamic force are shown in red for the x-direction, in green for the y-direction, and in blue for the z-direction. The wing motion is based on the 4-term kinematic profile.

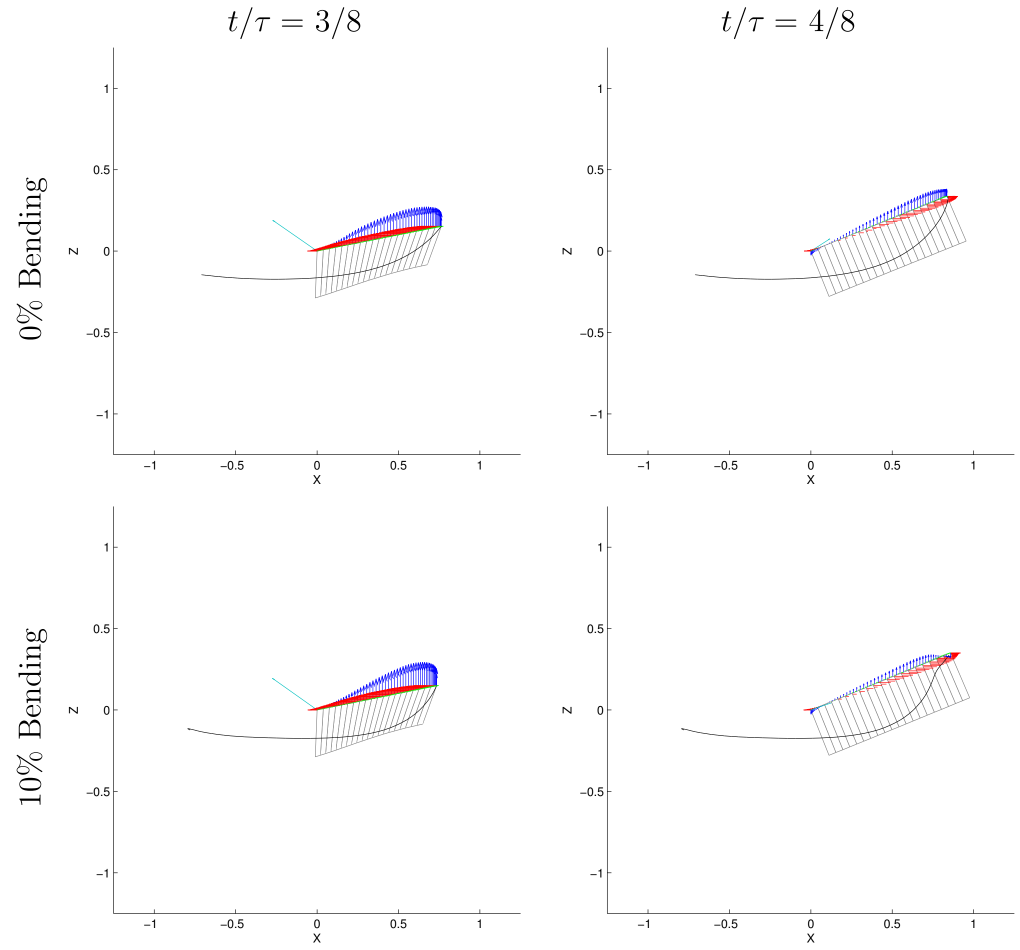

Figure 79: Comparison of the spanwise force distribution for the bending simulations. The three components of the sectional aerodynamic force are shown in red for the x-direction, in green for the y-direction, and in blue for the z-direction. The wing motion is based on the 4-term kinematic profile.

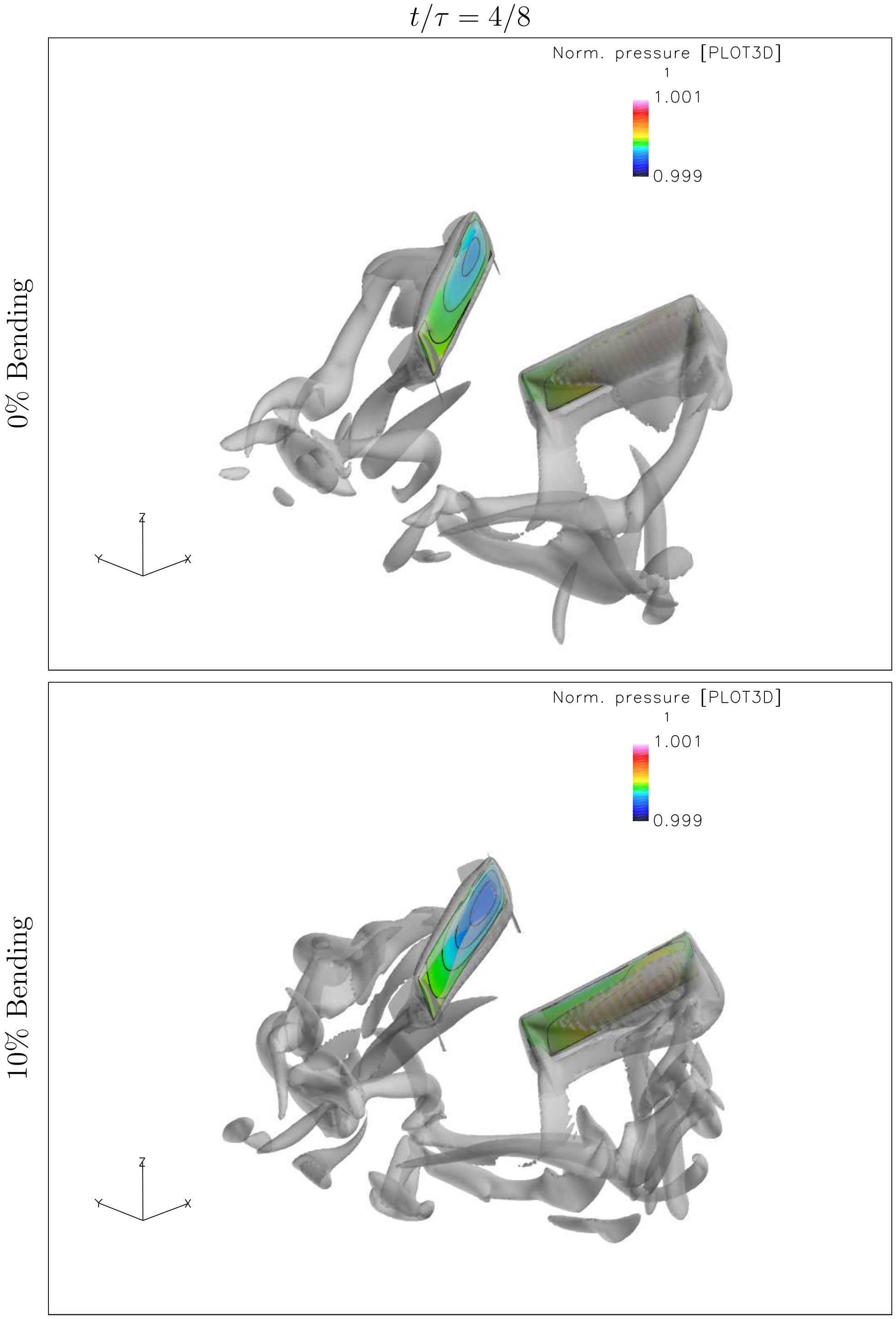

Figure 80: Iso-surface of vorticity magnitude for the 0% and 10% Bending simulations based on the 4-term kinematic profiles shown during pronation.

7.3 Influence on Aerodynamic Performance

For the deformation history utilized in this proof-of-concept examination, the mean vertical force increases with increasing tip deflection, shown in Table 6 for the 3-term kinematic profile and Table 7 for the 4-term kinematic profile. However, this increase in lifting capacity was tempered by an increase in the aerodynamic power requirement. For both of the kinematic profiles, the torsionally flexible wing with no bending represents the most efficient configuration.

Table 6: Computed aerodynamic forces, moments, and power for prescribed feathering and bending using the 3-term kinematic profile

	0%	5%	10%
CFx	3.638×10^{-03}	3.718×10^{-03}	3.079×10^{-03}
CFy	-1.625×10^{-02}	-1.766×10^{-02}	-1.794×10^{-02}
CFz	1.249×10^{-01}	1.285×10^{-01}	1.376×10^{-01}
CMx	-7.608×10^{-02}	-7.936×10^{-02}	-8.614×10^{-02}
CMy	-1.280×10^{-02}	-1.350×10^{-02}	-1.314×10^{-02}
CMz	4.001×10^{-03}	2.768×10^{-03}	7.654×10^{-04}
CP	7.229×10^{-02}	7.717×10^{-02}	8.570×10^{-02}
η_{aero}	$1.728\times10^{+00}$	$1.665\times10^{+00}$	$1.606\times10^{+00}$

Table 7: Computed aerodynamic forces, moments, and power for prescribed feathering and bending using the 4-term kinematic profile

	0%	5%	10%
CFx	5.117×10^{-03}	4.820×10^{-03}	4.070×10^{-03}
CFy	-1.147×10^{-02}	-1.417×10^{-02}	-1.814×10^{-02}
CFz	1.507×10^{-01}	1.552×10^{-01}	1.619×10^{-01}
CMx	-8.922×10^{-02}	-9.280×10^{-02}	-9.811×10^{-02}
CMy	-1.491×10^{-02}	-1.468×10^{-02}	-1.531×10^{-02}
CMz	9.512×10^{-03}	8.269×10^{-03}	6.694×10^{-03}
CP	9.011×10^{-02}	9.692×10^{-02}	1.060×10^{-01}
η_{aero}	$1.672\times10^{+00}$	$1.601\times10^{+00}$	$1.527\times10^{+00}$

VIII. Summary and Conclusions

8.1 Summary of Research

Navier-Stokes based simulation was utilized to understand how the dynamic response of the wing structure influences the aerodynamic behavior of a characteristic flapping wing configuration. The use of Navier-Stokes based simulation enabled detailed examination of the time-resolved aerodynamic forces, unsteady aerodynamic phenomena, and variations in the time-resolved wake structures for the large amplitude wing rotations utilized by natural fliers. The influence of structural deformation on the aerodynamic response was examined by superimposing torsional and bending modes onto the rigid wing approximation of the dynamic wing motions utilized by previous numerical investigations.

8.2 Geometric Configuration

A characteristic configuration based on the Hawkmoth *Manduca sexta* was developed after considering the influence of geometric variations, such as wing-body interaction, wing planform, and wing length, on the unsteady aerodynamic phenomena and aerodynamic performance. The characteristic configuration developed for this study utilized a single wing with a rectangular planform with prescribed wing motions based on the kinematic parameters documented by Willmott and Ellington [6]. This configuration represented a minimum geometric configuration that reproduced the characteristic unsteady aerodynamic phenomena, such as the leading edge vortex and wing-wake interactions, previously documented in the published literature for the Hawkmoth [15, 16, 19]. During the development of the characteristic configuration, it was observed that:

- There is a minimum separation distance between the wing and body, or wing-body gap, that is required in order to resolve the wing motion. The minimum wing-body gap depends on the wing planform, the origin of rotation, and the kinematic parameters.

- It was shown that the aerodynamic interactions between the wing and body were small for the wing-body gap required to resolve the rigid wing motion of the Hawkmoth planform without experiencing contact between the wing and body surfaces.
- Wing planform influences the amplitude of the time-history of the aerodynamic forces. However, the character of the force history and wake structures were similar for the Hawkmoth and rectangular wing planforms considered. This indicates that the Hawkmoth and rectangular wing planforms both induce similar unsteady aerodynamic phenomena for the same dynamic wing motion.
- One important contribution of the configuration study was the observation that the magnitude of the aerodynamic forces produced by wings of varying length, but similar planform and flapping frequency, scale with the square of the wing tip velocity.

8.3 Kinematic Profile

A cursory examination of the Fourier approximation of the kinematic profile highlighted the influence of several kinematic parameters on the aerodynamic response during the translational and feathering phases of motion:

- Sweep rate, elevation rate, and feathering orientation influence the aerodynamic forces during the translational phase of the wing motion where the leading edge vortex and the circulatory aerodynamic mechanisms play an important role.
- The feathering acceleration influences the non-circulatory aerodynamic phenomena and the rate of change in the bound circulation during the rotational phase of motion. This influences the transition of the “upper” and “lower” wing surfaces as the suction and pressure roles alternate at the end of each half-stroke.

8.4 Influence of Feathering Variation

Local structural deformations were superimposed onto the rigid wing motion to examine the influence of structural response on local aerodynamic response. Lacking a characterization of the Hawkmoth wing structure, documented feathering variations for a Hawkmoth at hover were approximated using the first torsion mode for a fixed-free beam. A good match to the documented feathering variation was achieved by reducing the amplitude of the feathering orientation at the wing root while maintaining the rigid wing feathering orientation near the wing tip. Wings of varying torsional stiffness were approximated by varying the amplitude of the feathering orientation at the wing root.

- The feathering rotation dominates the motion of the wing near the wing root.
- The spanwise variation in the feathering rotation alters the velocity and acceleration profile of the wing away from the elastic axis.
- The time-dependent force histories and the mean aerodynamic force and power requirements exhibit a strong dependence on the amplitude of the span-wise feathering variation.
- The reduced amplitude of the feathering acceleration has a significant influence on the local non-circulatory aerodynamic phenomena near the wing root. The change in the non-circulatory forces has a direct influence on the local pressure distribution along the wing length, altering the net aerodynamic forces during the rotational phase of motion.
- The variation in the non-circulatory aerodynamic phenomena at the wing root due to the change in the feathering acceleration influences the strength of the root vortex. This change in the root vortex alters the interaction with the circulatory aerodynamic phenomena along the wing length. These interactions in turn influence the circulatory aerodynamic phenomena near the wing tip and the non-circulatory wing-wake interactions, and have a direct influence on the overall aerodynamic performance at hover.

- The feathering variation alters the wing orientation and geometric angle of attack along the wing span during the translational phase of motion. This change in the wing orientation influences the strength of the leading edge vortex and circulatory aerodynamic mechanisms during the translational phase of the wing motion.

For the kinematic profiles studied in detail, the solution with a 50% reduction in the feathering amplitude at the wing root produced the greatest mean vertical force and represented the most aerodynamically efficient solution. This indicates that wings of moderate torsional stiffness may outperform both highly compliant and rigid wing structures.

8.5 Influence of Bending

Local deformations based on the first bending mode of a fixed-free beam were superimposed onto the torsionally flexible wing to examine the influence of bending on the local aerodynamic phenomena. The time history of the bending was based on the inertial forcing of the wing structure due to the kinematic profile and the amplitude of the bending was scaled to achieve tip displacements of 5% and 10% of the wing length. The bending deformations influenced the aerodynamic response during both the translational and rotational phases of motion.

- Incorporating bending deformations increased the aerodynamic force magnitude during the rotational phase of motion while decreasing the aerodynamic force magnitude during the translational phase of motion.
- An examination of the vortical wake structures suggests that the force variation early in the half-stroke are due to enhanced wing-wake interactions.
- The force decrease during the translational phase of motion corresponds to a reduction in tip velocity.
- The force increase at the end of the half-stroke is due to additional non-circulatory aerodynamic influences near the wing tip.

- The influence of the bending deformations on overall performance was to increase the mean vertical force while decreasing aerodynamic efficiency.

8.6 Contributions

Through an examination of the influence of prescribed structural response on the unsteady aerodynamic phenomena, this work provides new insight into the influence of structural response on the local unsteady aerodynamic phenomena and overall aerodynamic performance. The results of this work indicate that dynamic structural response plays an important role in determining the aerodynamic performance of flapping wing fliers.

In the case of a torsionally flexible wing, spanwise variations in the feathering orientation influence the strength and timing of the circulatory and non-circulatory unsteady aerodynamic phenomena produced by the dynamic wing motion. These local variations in the unsteady aerodynamic phenomena influence the evolution of the vortical wake structures, surface pressure distributions, and the directionality and strength of the net aerodynamic forces.

In the case of the flexible wing with bending degrees of freedom, the circulatory and non-circulatory unsteady aerodynamic phenomena were influenced by the variation in the span-wise velocity profile, particularly during the rotational phase of motion. The sensitivity of the aerodynamic performance to bending degrees of freedom was observed for tip deflections of 5% and 10% of the wing length. This indicates that spanwise bending may still play an important role in determining aerodynamic performance for wings with pronounced variations of the effective bending stiffness in the spanwise and chordwise directions.

This work also highlights the sensitivity of the global wake structure to small variations in the local aerodynamic phenomena. This sensitivity was observed through qualitative comparisons of the vortical wake structures and quantitative comparisons of the net aerodynamic force histories. This sensitivity of the aerodynamic forces and wake structure to small variations in the unsteady aerodynamic phenomena highlights the need to adequately resolve the underlying unsteady aerodynamic phenomena within future design tools that consider the influence of structural response and kinematic variations on aerodynamic performance.

8.7 Recommendations for Future Research

The present work provides a benchmark study examining the influence of structural response on aerodynamic performance using Navier-Stokes based simulation. By extending the simulation tools developed for this study, the role of multi-physics coupling in determining system performance may be explored by examining the following questions:

- Do aerodynamic forces or inertial elastic forces dominate the structural response?
- How does the phase relationship between the aerodynamic and inertial-elastic forces influence the structural response?
- Is the feathering rotation due to passive structural response or active actuation of the wing structure?
- Are higher-order modes present in the structural response of the coupled system?
    - If so, what influence do higher order modes have on the unsteady aerodynamic phenomena?
- How does fluid-structure-kinematic coupling influence agile maneuvers?
    - What is important to the transient response of the system?
    - What is the phase lag between change in wing actuation and change in the force history?
    - If there is a phase lag, is it due to structural response or aerodynamic response?

In addition to the role of multi-physics coupling on aerodynamic performance, the sensitivity of the unsteady aerodynamic phenomena to prescribed changes in the geometric configuration, kinematic profile, and structural response, may be explored using the current set of simulation tools:

- What is the influence of Reynolds number on the unsteady aerodynamic phenomena, and how should Reynolds number be defined for hovering configurations?
- What is the role of turbulence in insect flight, and how important is laminar-turbulent transition for capturing the near-body and off-body wake structures?
- How does the choice of wing planform influence aerodynamic performance?
  - Is there an ideal spanwise force distribution for efficiency and power?
  - What influence does area distribution and taper ratio have on the aerodynamic phenomena?
  - How does tip shape influence the interaction between the leading edge and tip vortices?
- What is the influence of the origin of rotation on aerodynamic performance?
  - How does the location of the feathering axis influence the leading edge vortex?
  - How does the location of the feathering axis influence the non-circulatory phenomena during pronation and supination?

Bibliography

1. Ellington, C. P., van den Berg, C., Willmott, A. P., and Thomas, A. L. R., "Leading-edge vortices in insect flight," *Nature*, Vol. 384, 1996, pp. 626–630.
2. Ellington, C., "The aerodynamics of hovering insect flight. III. Kinematics," *Philosophical Transactions of the Royal Society of London, Series B.*, Vol. 305, 1984, pp. 41–78.
3. Dickinson, M. H., "The effects of wing rotation on unsteady aerodynamic performance at low Reynolds numbers," *Journal of Experimental Biology*, Vol. 192, 1994, pp. 179–206.
4. Hover, F., Haugsdal, A., and Triantafyllou, M., "Effect of angle of attack profiles in flapping foil propulsion," *Journal of Fluids and Structures*, Vol. 19, 2004, pp. 37–47.
5. Lehmann, F.-O. and Pick, S., "The aerodynamic benefit of wing-wing interaction depends on stroke trajectory in flapping insect wings," *Journal of Experimental Biology*, 2007.
6. Willmott, A. P. and Ellington, C. P., "The mechanics of flight in the Hawkmoth Manduca Sexta II. Aerodynamic consequences of kinematic and morphological variation," *Journal of Experimental Biology*, Vol. 200, 1997, pp. 2723–2745.
7. Wang, Z. J., Birch, J. M., and Dickinson, M. H., "Unsteady forces and flows in low Reynolds number hovering flight: two-dimensional computations vs robotic wing experiments," *Journal of Experimental Biology*, Vol. 207, 2004, pp. 449–460.
8. Heathcote, S. and Gursul, I., "Flexible flapping airfoil propulsion at low Reynolds numbers," *43rd AIAA Aerospace Sciences Meeting and Exhibit*, AIAA, 10 - 13 January 2005.
9. Heathcote, S., Wang, Z., and Gursul, I., "Effect of spanwise flexibility on flapping wing propulsion," *36th AIAA Fluid Dynamics Conference and Exhibit*, AIAA, June 2006.
10. Barut, A., Das, M., and Madenci, E., "Nonlinear deformations of flapping wings on a micro air vehicle," *47th AIAA/ASME/ASCE/AHS/ASC Structures, Structural Dynamics, and Materials Conference*, 2006.
11. Hamamoto, M., Ohta, Y., Hara, K., and Hisada, T., "Application of fluid-structure interaction analysis to flapping flight of insects with deformable wings," *Advanced Robotics*, 2007.
12. Ellington, C., "The aerodynamics of hovering insect flight. II. Morphological parameters," *Philosophical Transactions of the Royal Society of London, Series B.*, Vol. 305, 1984, pp. 17–40.

13. Hedrick, T. L., "Personal Correspondence," .

14. McMichael, J. and Francis, C., "Micro air vehicles - toward a new dimension in flight," Tech. rep., DARPA, 1997.

15. van den Berg, C. and Ellington, C. P., "The three-dimensional leading-edge vortex of a 'hovering' model Hawkmoth," *Philosophical Transactions of the Royal Society of London, Series B.*, Vol. 352, 1997, pp. 329–340.

16. van den Berg, C. and Ellington, C. P., "The vortex wake of a 'hovering' model Hawkmoth," *Philosophical Transactions of the Royal Society of London, Series B.*, Vol. 352, 1997, pp. 317–328.

17. Willmott, A. P. and Ellington, C. P., "The mechanics of flight in the Hawkmoth Manduca Sexta I. Kinematics of hovering and forward flight," *Journal of Experimental Biology*, Vol. 200, 1997, pp. 2705–2722.

18. Willmott, A. P., Ellington, C. P., and Thomas, A. L. R., "Flow visualization and unsteady aerodynamics in the flight of the Hawkmoth," *Philosophical Transactions of the Royal Society of London, Series B.*, Vol. 352, 1997, pp. 303–316.

19. Liu, H., Ellington, C. P., Kawachi, K., van den Berg, C., and Willmott, A. P., "A computational fluid dynamic study of Hawkmoth hovering," *Journal of Experimental Biology*, Vol. 201, 1998, pp. 461–477.

20. Liu, H. and Kawachi, K., "A numerical study of insect flight," *Journal of Computational Physics*, Vol. 146, 1998, pp. 124–156.

21. Bomphrey, R. J., Lawson, N. J., Harding, N. J., Taylor, G. K., and Thomas, A. L. R., "The aerodynamics of Manduca Sexta: digital particle image velocimetry analysis of the leading-edge vortex," *Journal of Experimental Biology*, 2005.

22. Aono, H. and Liu, H., "Vortical structure and aerodynamics of hawkmoth hovering," *Journal of Biomechanical Science and Engineering*, Vol. 1, No. 1, 2006, pp. 234–245.

23. Hedrick, T. L. and Daniel, T. L., "Flight control in the hawkmoth Manduca sexta: the inverse problem of hovering," *Journal of Experimental Biology*, Vol. 209, 2006, pp. 3114–3130.

24. Aono, H., Shyy, W., and Liu, H., "Vortex dynamics in near wake of a hovering Hawkmoth," *46th AIAA Aerospace Sciences Meeting and Exhibit*, 2008.

25. Aono, H., Liang, F., and Liu, H., "Near- and far-field aerodynamics in insect hovering flight: an integrated computational study," *Journal of Experimental Biology*, Vol. 211, 2008, pp. 239–257.

26. Combes, S. A. and Daniel, T. L., "Flexural stiffness in insect wings I. Scaling and the influence of wing venation," *Journal of Experimental Biology*, Vol. 206, 2003, pp. 2979–2987.

27. Wootton, R. J., "Function, homolgy and terminology in insect wing systems," *Systematic Entomology*, Vol. 4, 1979, pp. 81–93.

28. Ennos, A. R., "The importance of torsion in the design of insect wings," *Journal of Experimental Biology*, Vol. 140, 1988, pp. 137–160.

29. Ennos, A. R., "The inertial cause of wing rotation in Diptera," *Journal of Experimental Biology*, Vol. 140, 1988, pp. 161–169.

30. Ennos, A. R., "Inertial and aerodynamic torques on the wings of diptera in flight," *Journal of Experimental Biology*, Vol. 142, 1989, pp. 87–95.

31. Sunada, S., Zeng, L., and Kawachi, K., "The relationship between dragonfly wing structure and torsional deformation," *Journal of Theoretical Biology*, Vol. 193, 1998, pp. 39–45.

32. Wootton, R., Evans, K., Herbert, R., and Smith, C., "The hind wing of the desert locust (Schistocerca gregaria Forskal) I. Functional morphology and mode of operation," *Journal Of Experimental Biology*, Vol. 203, No. 19, 2000, pp. 2921–2931.

33. Smith, C., Herbert, R., Wootton, R., and Evans, K., "The hind wing of the desert locust (Schistocerca gregaria Forskal) II. Mechanical properties and functioning of the membrane," *Journal Of Experimental Biology*, Vol. 19, 2000, pp. 2933–2943.

34. Herbert, R., Young, P., Smith, C., Wootton, R., and Evans, K., "The hind wing of the desert locust (Schistocerca gregaria Forskal) III. A finite element analysis of a deployable structure," *Journal Of Experimental Biology*, Vol. 203, No. 19, 2000, pp. 2945–2955.

35. Bergou, A. J., Xu, S., and Wang, Z. J., "Passive wing pitch reversal in insect flight," *J. Fluid Mech*, Vol. 591, 2007, pp. 321–337.

36. Combes, S. A. and Daniel, T. L., "Into thin air: Contributions of aerodynamic and inertial-elastic forces to wing bending in the Hawkmoth Manduca Sexta," *Journal of Experimental Biology*, Vol. 206, 2003, pp. 2999–3006.

37. Combes, S. A. and Daniel, T. L., "Flexural stiffness in insect wings II. Spatial distribution and dynamic wing bending," *Journal of Experimental Biology*, Vol. 206, 2003, pp. 2989–2997.

38. Wootton, R. J., Herbert, R. C., Young, P. G., and Evans, K. E., "Approaches to the structural modelling of insect wings," *Philosophical Transactions of the Royal Society of London, Series B.*, Vol. 358, 2003, pp. 1577–1587.

39. Casey, T. M., "Flight Energetics Of Sphinx Moths: Power Input During Hovering Flight," *Journal of Experimental Biology*, Vol. 64, 1976, pp. 529–543.

40. Rayner, J. M. V., "A vortex theory of animal flight. Part 1. The vortex wake of a hovering animal," *Journal of Fluid Mechanics*, Vol. 91, 1979, pp. 697–730.

41. Rayner, J. M. V., “A vortex theory of animal flight. Part 2. The forward flight of birds,” *Journal of Fluid Mechanics*, Vol. 91, 1979, pp. 731–763.

42. DeLaurier, “An aerodynamic model for flapping-wing flight,” *The Aeronautical Journal of the Royal Aeronautical Society*, April 1993, pp. 125–130.

43. Sunada, S., Kawachi, K., Watanabe, I., and Azuma, A., “Fundamental analysis of three-dimensional 'near fling',” *Journal of Experimental Biology*, Vol. 183, 1993, pp. 217–248.

44. Sunada, S., Kawachi, K., Watanabe, I., and Azuma, A., “Performance of a butterfly in take-off flight,” *Journal of Experimental Biology*, Vol. 183, 1993, pp. 249–277.

45. Smith, M. J. C., Wilkin, P. J., and Williams, M. H., “The advantages of an unsteady panel method in modelling the aerodynamic forces on rigid flapping wings,” *Journal of Experimental Biology*, Vol. 199, 1996, pp. 1073–1083.

46. Sun, M. and Tang, J., “Unsteady aerodynamic force generation by a model fruit fly wing in flapping motion,” *Journal of Experimental Biology*, Vol. 205, 2002, pp. 55–70.

47. Sun, M. and Tang, J., “Lift and power requirements of hovering flight in Drosophila virilis,” *Journal of Experimental Biology*, Vol. 205, 2002, pp. 2413–2427.

48. Sun, M., “High-lift generation and power requirements of insect flight,” *Fluid Dynamics Research*, Vol. 37, 2005, pp. 21–39.

49. Ramamurti, R. and Sandberg, W. C., “Computational study of 3-D flapping foil flows,” *39th AIAA Aerospace Sciences Meeting and Exhibit*, 2001.

50. Ramamurti, R. and Sandberg, W. C., “A three-dimensional computational study of the aerodynamic mechanisms of insect flight,” *Journal of Experimental Biology*, Vol. 205, 2002, pp. 1507–1518.

51. Hamamoto, M., Ohta, Y., Hara, K., and Hisada, T., “Free-flight analysis of flapping flight during turning by fluid-structure interaction finite element analysis based on arbitrary lagrangian-eulerian method,” *Proceedings of the 2004 IEEE International Confrence on Robotics and Automation*, 2004.

52. Mittal, R., “Computational Modeling in Biohydrodynamics: Trends, Challenges, and Recent Advances,” *IEEE Journal of Oceanic Engineering*, Vol. 29, No. 3, 2004.

53. Mittal, R., “Understanding insect wing performance via computational modeling,” *AFOSR MAV Workshop, Denver CO.*, June 2006.

54. Mittal, R., Utturkar, Y., and Udaykumar, H. S., “Computational modeling and analysis of biomimetic flight mechanisms,” *40th Al AA Aerospace Sciences Meeting & Exhibit*, AIAA, 2002.

55. Pandya, S., Venkataswaran, S., and Pulliam, T., “Implementation of preconditioned dual-time procedures in OVERFLOW,” *41st Aerospace Sciences Meeting & Exhibit*, 2003.

56. Nichols, R. H., Tramel, R. W., and Buning, P. G., “Evaluation of two high order WENO schemes,” *25th AIAA Applied Aerodynamics Conference*, 2007.

57. Potsdam, M. A. and Silva, M. J., “Tilt rotor aeromechanics phenomena in low speed flight,” *Proceedings of the Users Group Conference (DOD_UGC 04)*, 2004.

58. Potsdam, M., Yeo, H., and Johnson, W., “Rotor airloads prediction using loose aerodynamic/structural coupling,” *American Helicopter Society 60th Annual Forum*, 2004.

59. Nichols, R. H. and Buning, P. G., “OVERFLOW 2 Training Class: Flow Solver Overview,” *8th Symposium on Overset Composite Grids & Solution Technology*, 2006.

60. *OVERFLOW 2.1 Documentation*.

61. *Users Manual for OVERFLOW 2.1*, June 2008.

62. Jespersen, D., Pulliam, T., and Buning, P., “Recent enhancements to OVERFLOW,” *35th Aerospace Sciences Meeting and Exhibit*, 1997.

63. Conion, J., “OVERFLOW code empowers Computational Fluid Dynamics,” *HPCC Insights*, Vol. 5, 1998.

64. Jespersen, D. C., “Parallelism and OVERFLOW,” Tech. rep., NASA Techinical Report NAS-98-013, 1998.

65. Buning, P. G., “Status and Recent Applications of OVERFLOW,” *5th Symposium on Overset Grids & Solution Technology*, 2000.

66. Chou, H. S. Y. and Ekaterinaris, J. A., “A Compact High-Order CFD Package for the Flow Solver Overflow,” *41st Aerospace Sciences Meeting and Exhibit*, 2003.

67. Slotnick, J., Buning, P., and Nichols, R., “OVERFLOW Flow Solver Overview,” *8th Symposium on Overset Composite Grids & Solution Technology*, 2006.

68. Buning, P. G. and Nichols, R. H., “OVERFLOW 2 Training Class,” *8th Symposium on Overset Composite Grids & Solution Technology*, 2006.

69. Chan, W. M., Gomez, R. J., Rogers, S. E., and Buning, P. G., “Best practices and tools for overset surface and volume grid generation,” *8th Symposium on Overset Composite Grids & Solution Technology*, 2006.

70. Sherer, S. E. and Scott, J. N., “High-order compact finite-difference methods on general overset grids,” *Journal of Computational Physics*, Vol. 210, 2005, pp. 459–496.

71. Chan, W. M. and Buning, P. G., “User’s Manual for FOMOCO Utilities - Force and Moment Computation Tools for Overset Grids,” Tech. rep., NASA, 1996.

72. Buning, P. G. and Nichols, R. H., "OVERFLOW 2 Training Class: Moving Body Capability," *8th Symposium on Overset Composite Grids & Solution Technology*, 2006.

73. Meakin, R., "Hole Cutting," *8th Symposium on Overset Composite Grids & Solution Technology*, 2006.

74. Murman, S. M., Chan, W. M., Aftosmis, M. J., and Meakin, R. L., "An interface for specifying rigid-body motions for CFD applications," *41st AIAA Aerospace Sciences Meeting*, AIAA, 2003.

75. Harlow, F. H. and Welch, J. E., "Numerical calculation of time-dependent viscous incompressible flow of fluid with free surface," *The Physics of Fluids*, 1965.

76. Patankar, S. V., *Numerical heat transfer and fluid flow*, Hemisphere, 1980.

77. Hill, M. J., *Coupled fluid-structure simulations of helicopter rotors*, Master's thesis, Pennsylvania State University, 2006.

78. White, F. M., *Viscous Fluid Flow*, McGraw-Hill, 2006.

79. Bush, B. L. and Baeder, J. D., "Computational investigation of flapping-wing flight," *37th AIAA Fluid Dynamics Conference and Exhibit*, 2007.

80. Guilmineau, E. and Queutey, P., "A numerical simulation of vortex shedding from an oscillating circular cylinder," *Journal of Fluids and Structures*, Vol. 16, No. 6, 2002, pp. 773–794.

81. Lu, X. and Dalton, C., "Calculation of the timing of vortex formation from an oscillating cylinder," *Journal of Fluids and Structures*, Vol. 10, 1996, pp. 527–541.

82. McGowan, G. Z., Gopalarathnam, A., Ol, M. V., Edwards, J. R., and Fredberg, D., "Computation vs. experiment for high-frequency low-Reynolds number airfoil pitch and plunge," *46th AIAA Aerospace Sciences Meeting and Exhibit*, 2008.

83. Leishman, J. G., *Principles of helicopter aerodynamics*, Published by Cambridge University Press, 2002.

84. Willmott, A. P. and Ellington, C. P., "Measuring the angle of attack of beating insect wings: Robust three-dimensional reconstruction from two-dimensional images," *Journal of Experimental Biology*, Vol. 200, 1997, pp. 26932704.

85. Bos, F., *Influence of wing kinematics on performance in insect flight*, Master's thesis, Delft University of Technology, 2005.

86. Bos, F., Lentink, D., van Oudheusden, B., and Bijl, H., "Numerical study of kinematic wing models of hovering insect flight," *45th AIAA Aerospace Sciences Meeting and Exhibit*, 2007.

87. Bos, F., van Oudheusden, B., and Bijl, H., "Three-dimensional numerical simulations of flapping wings at low Reynolds numbers," *OpenFOAM Workshop, Zagreb*, 2007.

88. Bos, F. M., Lentink, D., van Oudheusden, B. W., and Bijl, H., "Influence of wing kinematics on aerodynamic performance in hovering insect flight," *Journal of Fluid Mechanics*, Vol. 594, 2008, pp. 341–368.

89. Dickinson, M. H., Lehmann, F.-O., and Sane, S. P., "Wing rotation and the aerodynamic basis of insect flight," *SCIENCE*, Vol. 284, 1999, pp. 1954–1960.

90. Sane, S. P. and Dickinson, M. H., "The control of flight force by a flapping wing: Lift and drag production," *Journal of Experimental Biology*, Vol. 204, 2001, pp. 2607–2626.

91. Sane, S. P. and Dickinson, M. H., "The aerodynamic effects of wing rotation and a revised quasi-steady model of flapping flight," *Journal of Experimental Biology*, Vol. 205, 2002, pp. 1087–1096.

92. Bomphrey, R. J., Lawson, N. J., Taylor, G. K., and Thomas, A. L. R., "Application of digital particle image velocimetry to insect aerodynamics: measurement of the leading-edge vortex and near wake of a Hawkmoth," *Experiments in Fluids*, Vol. 40, 2006, pp. 546–554.

REPORT DOCUMENTATION PAGE

Form Approved
OMB No. 0704–0188

1. REPORT DATE *(DD–MM–YYYY)* 18–06–2009	**2. REPORT TYPE** Dissertation	**3. DATES COVERED** *(From — To)* Sept 2004 — June 2009

4. TITLE AND SUBTITLE

Influence of Structural Flexibility
on Flapping Wing Propulsion

5a. CONTRACT NUMBER

5b. GRANT NUMBER

5c. PROGRAM ELEMENT NUMBER

6. AUTHOR(S)

McClung, Aaron, M., CIV

5d. PROJECT NUMBER

5e. TASK NUMBER

5f. WORK UNIT NUMBER

7. PERFORMING ORGANIZATION NAME(S) AND ADDRESS(ES)

Air Force Institute of Technology
Graduate School of Engineering and Management
2950 Hobson Way
WPAFB OH 45433-7765

8. PERFORMING ORGANIZATION REPORT NUMBER

AFIT/DS/ENY/09-J01

9. SPONSORING / MONITORING AGENCY NAME(S) AND ADDRESS(ES)

Aerospace, Chemical and Material Sciences Directorate
Air Force Office of Scientific Research
875 N. Randolph, Ste.325, Rm. 3112, Arlington Virginia, 22203
Dr. Victor Giurgiutiu

Design and Analysis Methods Branch, Structures Division
Air Force Research Laboratory, Air Vehicles Directorate
2210 Eighth Street, Wright-Patterson Air Force Base, OH 45433
Dr. Philip Beran

10. SPONSOR/MONITOR'S ACRONYM(S)

AFRL/RBSD, AFOSR/NA

11. SPONSOR/MONITOR'S REPORT NUMBER(S)

12. DISTRIBUTION / AVAILABILITY STATEMENT

Approval for public release; distribution is unlimited.

13. SUPPLEMENTARY NOTES

14. ABSTRACT

The influence of structural deformations on the aerodynamic response of a flapping wing configuration was examined using Navier-Stokes based simulation. Two deformation modes, torsion and bending, were considered for an elastic axis along the leading edge of the wing. Both deformation modes influence the velocity and acceleration profile of the wing surface, altering the unsteady aerodynamic phenomena produced by the dynamic wing motion. The spanwise feathering rotation, or torsional response, alters the motion of the wing near the wing root. This variation in the acceleration profile influences the non-circulatory aerodynamic response and the local wake structures produced near the wing root during pronation and supination. Increased lifting forces and enhanced aerodynamic efficiencies were observed for a moderate increase in torsional flexibility. Peak bending deformations near the wing tip also occur during pronation and supination, altering the velocity and acceleration profiles of the wing as the circulatory aerodynamic phenomena undergo a transition as the wing changes direction of motion. Because of the timing of the bending deformations, small tip deformations may have a significant influence on overall aerodynamic performance.

15. SUBJECT TERMS

Computational Fluid Dynamics (CFD), Fluid-Structure Interaction (FSI), Micro-Aerial Vehicle (MAV), Unmanned Aerial System (UAS), Insect Flight, Flapping Wing, OVERFLOW, Hawkmoth, *Manduca sexta*

16. SECURITY CLASSIFICATION OF:			**17. LIMITATION OF ABSTRACT**	**18. NUMBER OF PAGES**	**19a. NAME OF RESPONSIBLE PERSON**
a. REPORT	**b. ABSTRACT**	**c. THIS PAGE**			Raymond C. Maple
U	U	U	UU	180	**19b. TELEPHONE NUMBER** *(include area code)* N/A